A MULTI-PRONGED, NONINVASIVE PROBING OF ELECTRODEPOSITION IN LI-ION BATTERIES

A Thesis

by

MICHAEL ANDREW KALAN

Submitted to the Office of Graduate and Professional Studies of
Texas A&M University
in partial fulfillment of the requirements for the degree of

MASTER OF SCIENCE

Chair of Committee,	Partha P. Mukherjee
Committee Members,	Sarbajit Banerjee
	Hong Liang
Head of Department,	Andreas A. Polycarpou

May 2017

Major Subject: Mechanical Engineering

ABSTRACT

Lithium ion batteries hold the potential to play a key role in meeting our future and increasing energy storage needs. Lithium ion batteries have the highest energy density of all battery systems currently available. Since their introduction to the modern battery market in the mid 90’s they have evolved and become the choice system for meeting energy needs in portable electronic devices. Lithium ion batteries, however, face many challenges preventing them from being utilized to their fullest potential. They suffer from self-discharge, degradation over repeated charging, not operating well at extreme low or high temperatures, and can suffer from the deposition of metallic lithium during charging. This deposition builds up on the surface of the graphite electrode and can lead to the formation of structures called dendrites. These dendrites can cause problems like internal short-circuits, ultimately resulting in the battery catching on fire.

The focus of this work is to study the electrodeposition of lithium on graphite electrodes. Two main tools are used over the course of this study: modeling and experimentation.

The first half of this work discusses the approach through computational modeling. A simple one dimensional, needle-like dendrite model is developed. Through analysis of the concentration gradient that occurs near the surface of the electrode and evaluation of the overpotentials that develop due to applied current at the surface of the electrode a relationship is found for the tip current density. Propagation of the dendrite is calculated from determination of the tip current density and application of Faraday’s law. Appropriate verification through the method of manufactured solutions and validation by comparison to previously reported experimental data are discussed.

The second half of this work cover the experimental parts of this work to probe the electrodeposition of lithium on graphite electrodes. The development of the cell fabrication techniques and the characterization of the graphite electrode material used in these experiments is explained. The graphite used in these experiments was CMS graphite on a copper current collector with a specific capacity of 317 mAh/g.

The experimental investigation of electrodeposited lithium on graphite electrodes is studied by the development and utilization of a novel dynamic impedance measurement technique. The impedance response of the cell is captured across different states of charge of normally charged cells and of cells where electrodeposition was proven to occur. Through trends in the impedance data, and through utilization of equivalent circuit analysis, correlations of changes in the impedance with the electrodeposition of lithium are made. In the absence of lithium electrodeposition, the general impedance response of the cell is to increase with increasing SOC. However, this trend reverses under conditions where electrodeposition is occurring. The presence of electrodeposited lithium is verified using SEM imaging.

DEDICATION

To my mother and father. For being the giants whose shoulders I could stand on.

ACKNOWLEDGEMENTS

First and foremost, I must acknowledge the many blessings that have been bestowed upon me by God the Almighty Father who ultimately gives me the gifts, talents, and opportunities to pursue this work in accord with His divine plan and for His greater glory.

In addition, I owe a debt of gratitude to the many friends and advisors who made this work possible and provided the support to help me complete this thesis. This work would not have been possible without the help and support of my primary advisor Partha Mukherjee, and his enthusiasm and example to always do great work. I also received much support from my fellow graduate students in the ETSL lab; in particular, I would like to thank Chien-Fan Chen, Daniel Robles, Aashutosh Mistry, and Robert Minter who provided me with much guidance, support, and help during the progress of my work.

During the course of this work, I had the privilege to spend a few months working at Oak Ridge National Laboratory in Tennessee. Srikanth Allu and John Turner helped guide my work while there and taught me a tremendous amount about the computational aspects of science and engineering.

Finally, I would like to extend a very special thanks to all my friends and family, who are too numerous to list here, but have provided me with support, encouragement, and love to live up to my fullest potential. The most important of course are my mom, Mary, and my father, Bob, whose constant example and guidance in virtue motivate me to always work harder and never stop striving to be a better man.

CONTRIBUTORS AND FUNDING SOURCES

Contributors

This work was supervised by a thesis committee consisting of Professor Partha P. Mukherjee (advisor) and Professor Hong Liang of the Department of Mechanical Engineering and Professor Sarbajit Banerjee, of the Department of Chemistry.

All work for the thesis was completed independently by the student, under the advisement of Partha P. Mukherjee of the Department of Mechanical Engineering.

Funding Sources

Graduate study was supported by a fellowship from Texas A&M University.
This research was supported in part by the faculty research initiation grant from Texas A&M University and in part by the U.S. Department of Energy, Office of Science, Oak Ridge Institute for Science and Education (ORISE) at Oak Ridge National Laboratory.

NOMENCLATURE

CPE	constant phase element
DEC	diethyl carbonate
DMC	dimethyl carbonate
EC	ethylene carbonate
EDL	electric double layer
EIS	electrochemical impedance spectroscopy
EMC	ethyl-methyl carbonate
$LiCoO_2$	lithium cobalt oxide
mAh	milliampere hour: unit of current
MMS	method of manufactured solutions
MTI	MTI Corporation: supplier of materials and engineering equipment
OCP	open circuit potential
PDE	partial differential equation
SEM	scanning electron microscope
TEM	tunneling electron microscope
XPS	x-ray photoelectron spectroscopy

TABLE OF CONTENTS

LIST OF FIGURES

Page

LIST OF TABLES

CHAPTER I

INTRODUCTION AND LITERATURE REVIEW

Motivation and Challenges

Energy storage is one of the most fundamental challenges faced by society in the 21st century. Everything we do depends on the availability of stored energy: growing food, supplying drinking water, transporting goods, and communicating all rely on the availability of stored energy. There are many different ways to store energy. Gravitational potential energy is a way to store energy in a body based upon that body's position relative to other bodies. Hydroelectric dams use the gravitational potential energy of accumulated water at a high elevation to drive turbines at a lower elevation and generate electricity. [1] Chemical potential energy or chemical potential is another way to store energy.[2] The chemical potential refers to the amount of energy that can be released (or absorbed) during a chemical reaction (ie. the breaking or forming of chemical bonds). The internal combustion engine is a common means of utilizing chemical potential energy through the combustion of a fuel, like gasoline, and finds itself in many applications. One of the most popular applications is in supplying the world's transportation needs. [3] Nuclear potential energy is another form of potential energy that harnesses the energy stored in the bonds of an atom's nucleus. Breaking atomic bonds releases a tremendous amount of energy and has been utilized from applications ranging from military weaponry that ended the Second World War to power plants which provide large amounts of stable electricity.[3-5]

The method used for the production or storage of energy is application and situation specific. It is not possible to use Hoover Dam to power an automobile; it is better to use an internal combustion engine. A submarine does not use an internal combustion engine, because that requires carrying large amounts of additional fuel, or refueling; rather is uses a nuclear reactor. The specific application and corresponding requirements dictate the possible means of energy production and storage.

The electrochemical energy storage system is another means of energy storage available.[6] Electrochemical energy storage involves the conversion, or transduction of chemical energy into electrical energy or vice versa.[7] Common electrochemical systems include fuel cells, supercapacitors, and batteries. Batteries have been in the lime light of modern energy storage research in part because of the rise of modern electronics. Batteries are very applicable energy storage devices for all of our electronic devices. They are condense systems, have reasonable energy density, and are “all-in one” units. Everything needed for the production and the storage of energy is completely contained inside the battery cell. The fuel, reaction mechanisms, and all necessary components come in one package. This is in contrast to other energy systems where fuel is normally stored externally: fuel cells, internal combustion engine, etc.

Batteries, however, have many short comings. They suffer from self-discharge-the loss of energy without actually being used- they degrade over time, and, if rechargeable, degrade over repeated charging. Furthermore, they take long periods of time to recharge and can only be recharged relatively slowly. In comparison to other forms of energy (like the internal combustion engine) batteries have low energy density. The short comings of batteries systems have prompted much research, the understanding of which requires some fundamental background knowledge.

Fundamental Electrochemistry and Basic Battery Operation

A battery is an electrochemical system, and has been around for many years. Benjamin Franklin is credited with having first coined the phrase “battery” in 1749. He used to describe a system of linked capacitors. Thirty years later in 1780 Luiki Galvani (for whom the galvanic cell is named) described “animal electricity” when he created an electrical circuit through a frog. Though he did not realize it at the time, this was essentially the first battery. In 1800 Alessandro Volta discovered that in Galvani’s experiment the energy was not actually coming from the frog, but had a different source. He setup an experiment where he produced the first non-animal battery, which was termed the *voltaic pile*.[8]

Building on previous research, in 1836 John Frederic Daniell created the Daniell cell when investigating different ways to configure and overcome some of the problems associated with the voltaic pile. This work was followed by developments from William Robert Grove in 1844 who produced the Grove cell. In 1859 Gaston Plante created the world’s first rechargeable battery based on a lead-acid system.[8]

Following these initial discoveries, the field of battery research slowed in the latter 19th century. The rise of the internal combustion engine and its utilization in the automobiles overshadowed the field of battery technology. Early attempts to create an electric vehicle proved futile as the internal combustion engine provided far more energy than the battery. The lead-acid rechargeable battery was integrated into automobiles to provide accessory power when the engine was not running and operate the starter, but any further research efforts into batteries were slowed.

In 1912 a new battery system was discovered: the lithium battery. This new battery held greater potential than previous battery systems. It promised both high energy and light weight characteristics. It would take almost the rest of the century, however, before this battery system's potential was unlocked and it would find its niche application.

In 1991 Sony produced the first lithium ion battery to be used in a portable electronic device. [9, 10] It has since become the industry standard battery and has been the power house behind some of the newest technological devices, such as the iPhone.

As illustrated by the Ragone plot in Figure 1, the lithium ion battery has both the highest specific energy density (Wh/kg) and the highest volumetric energy density (Wh/L) of any modern battery system.[11] These properties makes the lithium ion battery system the most viable system for battery based energy storage applications.

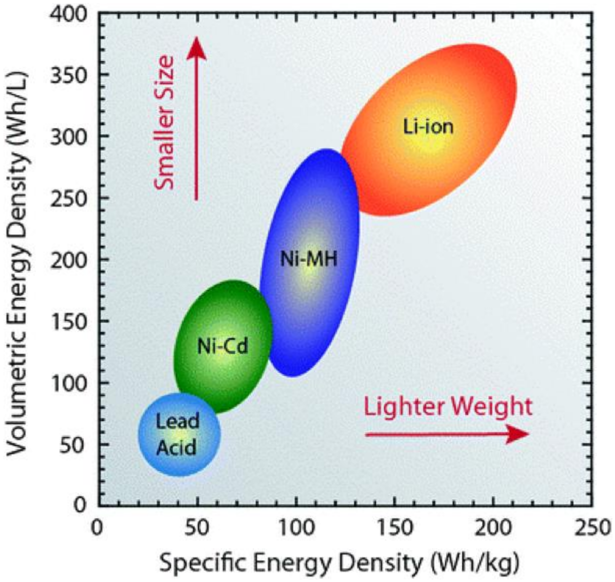

Figure 1. Ragone plot showing the high volumetric and specific energy density of lithium ion systems. This is ideal for applications like portable electronic devices and cars where size is a limiting factor.[11]

Lithium ion batteries can physically come in many configurations. Common configurations are shown in Figure 2 and Figure 3. Figure 2 shows a cylindrical lithium ion battery and the corresponding components. Cylindrical cells are often found in automotive applications. Figure 3 shows a rectangular, or pouch cell lithium ion battery configuration and the corresponding components. The pouch cell geometry is typically found in laptops or other portable electronics. Regardless of geometrical shape, all lithium ion batteries contain the same basic components—two electrodes, a separator, electrolyte, casing – and operate on the same fundamental principles.

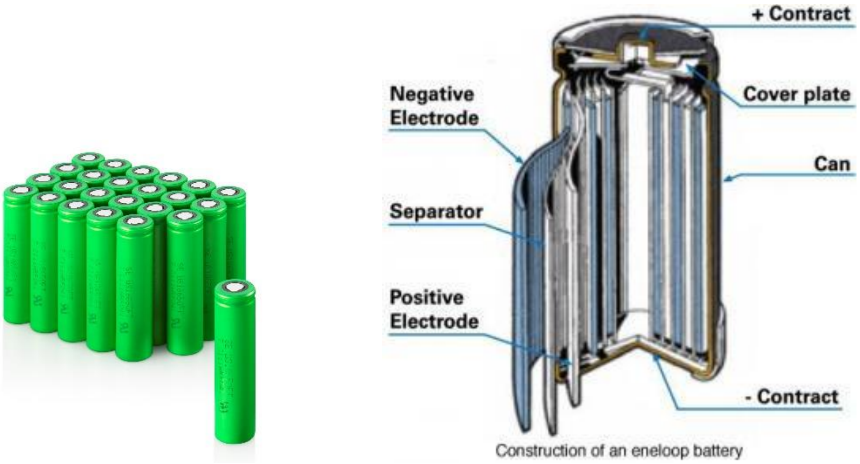

Figure 2. Cylindrical geometry lithium ion battery. Found in electric vehicle applications[12, 13]

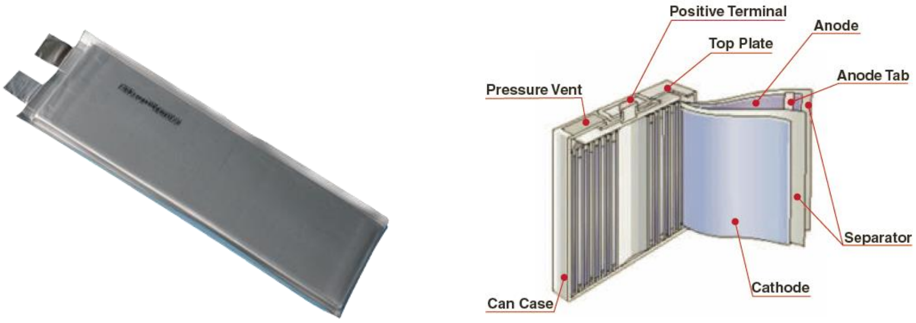

Figure 3. Pouch geometry lithium ion battery. Found in laptop and other portable electronics [14, 15]

The fundamental operation of the battery is best explained using Figure 4. The fundamental components in a battery include: positive electrode (cathode), negative electrode (anode), electrolyte, and separator. The electrodes are made up of the electrode material and the current collector. The electrode materials are different for the anode and cathode. A common anode electrode material is graphite. [16, 17] Common cathode materials include lithium cobalt oxide ($LiCoO_2$), lithium manganese oxide ($LiMn_2O_4$), and lithium nickel oxide ($LiNiO_2$). [18] The current collector is a thin metal foil that electrode material is adhered to and provides electrons to the circuit. A common anode current collector is copper, and a common cathode current collector is aluminum. The metals used for a particular electrode are based upon how the metals react with the electrolyte and its operating voltage. [19] An anode and cathode electrode sheet are shown in Figure 5.

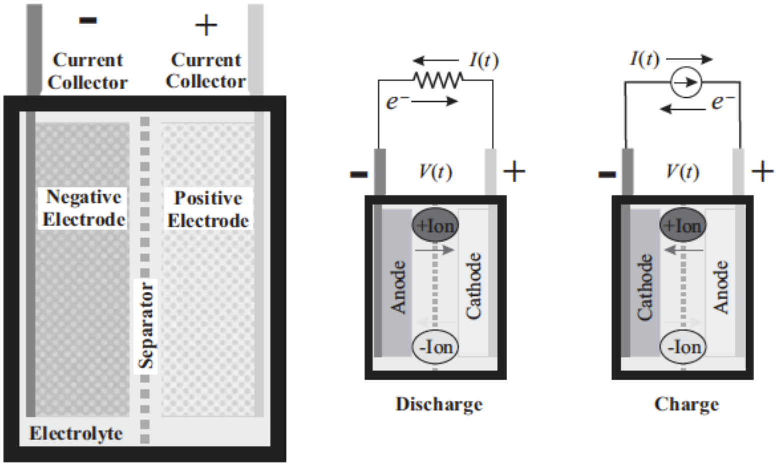

Figure 4. Schematic showing the flow of current in the external circuit and ions in the internal circuit.[20]

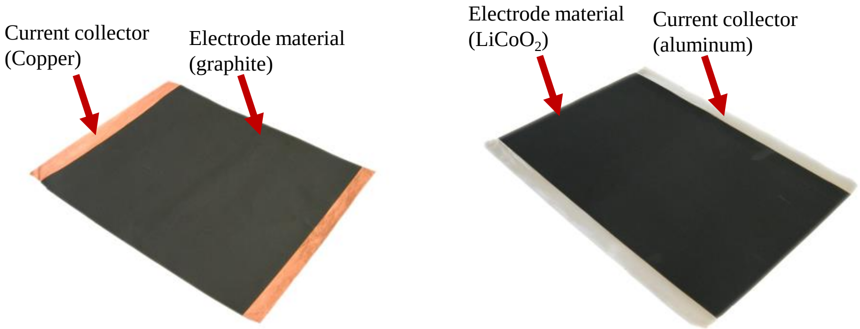

Anode Electrode Sheet

Cathode Electrode Sheet

Figure 5. Common electrode sheets. The anode electrode sheet consists of a copper current collector and graphite electrode material. The cathode electrode sheet consists of an aluminum current collector and $LiCoO_2$ electrode material.

Two circuits exist in a battery and both must be connected simultaneously for the battery to work: an external electrical circuit and an internal electrochemical circuit. The external electrical circuit connects the positive current collector to the negative current collector; usually a wire is used to complete the circuit. When connected, current flows through the external circuit. During discharge current spontaneously flows from the positive current collector to the negative current collector. During charge an external source provides an electromotive force to cause current to flow from the negative current collector to the positive current collector. The flow of current for charge and discharge is illustrated in Figure 4.

The internal electrochemical circuit is the crux of battery operation. Inside the battery, the positive and negative electrodes are immersed in an electrolyte solution. The electrolyte solution is typically an organic solvent: ethylene, dimethyl, diethyl, and/or ethyl-methyl carbonates (EC, DMC, DEC, EMC) and a lithium salt are the basic components of the electrolyte solution. The alkyl carbonates are used due to their stability for voltages in the 4 V range. They also have high conductivities, a reasonable boiling and freezing point, and sufficiently low toxicity. The most common salt is $LiPF_6$. Other lithium salts have been utilized, however each have their own draw backs.[16] $LiAsF_6$ is poisonous, $LiClO_4$ is explosive, $LiBF_4$ interacts poorly with the anode, $LiSO_3CF_3$ possesses too low a conductivity, $LiN(SO_2CF_3)_2$ and $LiC(SO_2CF_3)_3$ interact poorly with the aluminum current collector.[16, 18, 19] Electrolyte performance – the ability for the electrolyte to withstand a wide range of temperatures, voltages, and possess a high conductivity – can be increased by utilizing electrolyte additives. Electrolyte additives, which usually account for no more that 5% by weight or volume of the electrolyte solution have been found to increase salt stability, prevent degradation of the anode and cathode, reduce the flammability of the electrolyte, and provide overcharge protection.[21]

The internal electrochemical circuit consists of positively charged lithium ions moving back and forth between the positive and negative electrode. To maintain chargebalance the positively charged lithium ions in the internal electrochemical circuit travel in the same direction as the negatively charged electrons moving in the external electrical circuit. During discharge lithium ions migrate from the negative electrode to the positive electrode. At each electrode different electrochemical processes take place that allow the lithium ions to insert or de-insert, through a process called intercalation, from the electrode material. During charge lithium ions are driven from the positive electrode to the negative electrode.

Eq. 2, lithium ions intercalate into the carbon structure and are reduced to form Eq. 1 represents the electrochemical reaction that takes place at the cathode. During charge the active material, in this example LiCoO2, is oxidized and lithium ions are de-intercalated from the electrode material. At the negative electrode, represented by Li_xC, the active material of the anode. During discharge the reverse reaction takes place. At the anode Li_xC is oxidized and lithium ions de-intercalate from the graphite structure of the anode. At the cathode lithium ions are reduced forming $LiCoO_2$. [20]

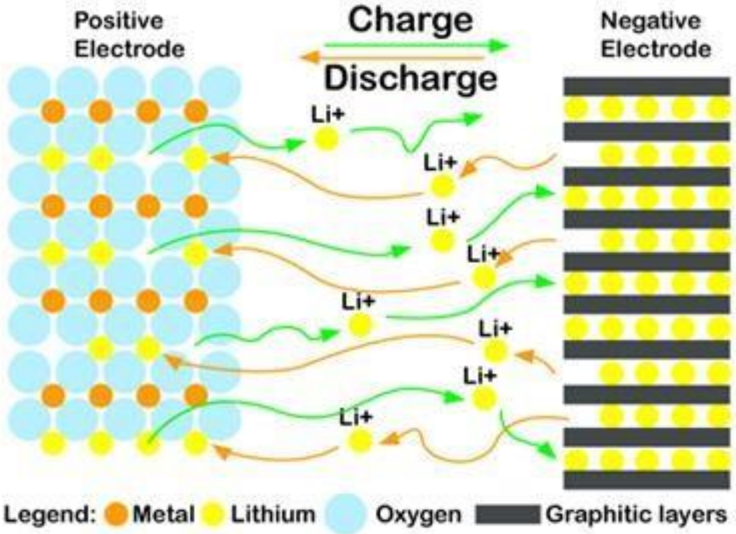

Figure 6. Schematic representation of the operation of the internal electrochemical circuit in a lithium ion battery. During charge lithium ions de-intercalate from the positive electrode and intercalate into the negative electrode. During discharge the reverse operation takes place. [11]

$$Li_{1-x}CoO_2 + xLi^+ + xe^- \underset{\text{charge}}{\overset{\text{discharge}}{\rightleftarrows}} LiCoO_2 \qquad \text{Eq. 1}$$

$$Li_xC \underset{\text{charge}}{\overset{\text{discharge}}{\rightleftarrows}} C + xLi^+ + xe^- \qquad \text{Eq. 2}$$

Complications and the Need for Improvement

Like every technology, lithium ion batteries have their own set of complications and problems. In some situations, their problems become a safety hazard. Such problems have necessitated a plethora of scientific research.

Boeing Corporation recently suffered from the effects of lithium ion battery failure in one of their aircraft, the Boeing 787 Dreamliner. This world class, long-range, mid-size, wide-body aircraft is one of Boeing's elite commercial airplanes. A recent design change to replace the formerly standard internal combustion engine, used to provide power to the plane when on the ground with the turbines off, with lithium ion batteries proved to be detrimental and scathed the reputation of the company.[22]

An issue occurred in which the lithium ion batteries in several Dreamliners suffered from thermal runaway. Thermal runaway is not a new issue with lithium ion batteries, but it is not completely understood. Several aircraft suffered because their lithium ion batteries experienced thermal runaway after only 52,000 flight hours rather than after the 10 million flight hours as predicted by Boeing.[22]. The result of five incidents (electrical fires) in five days on 787s forced the Federal Aviation Administration to order the entire fleet of 787 Dreamliners be grounded until Boeing could investigate the problem and come up with a solution. This cost time, money, and tarnished the reputation of Boeing among the aviation community.[22]

Implementing new technologies is never easy, and there are always obstacles that must be overcome. Fortunately, no one was hurt or killed in any of the incidents (most likely thanks to the quality engineering and safety systems), but the event illustrates the need for further research to develop a more comprehensive understanding of lithium ion batteries and their failure mechanisms so that they can be safely and effectively utilized to meet our energy needs.[13]

Understanding Degradation and Failure Mechanisms in Lithium Ion Batteries

Desired operating conditions for lithium ion batteries include high currents, a wide range of operating temperatures, fast charging rates, and high voltages. Many of these requirements stem from the fact that energy applications are very time dependent. Often end users have applications that need a source of energy and they need it immediately. Similarly, the time to build up stored energy is time dependent. An end user will not wait all day for their cell phone battery to charge. In applications such as regenerative braking, the energy is only available for a short period and has to be stored or dissipated very quickly. Furthermore, once the energy is stored it eventually needs to be reclaimed, and repurposed. In most applications, this needs to be accomplished repeatedly, so batteries also have to have high cycle-ability. These operating conditions put high requirements on battery systems and consequently all battery systems undergo degradation, which ultimately leads to failure during operation. Degradation and failure is a culmination of many effects, including but not limited to temperature, charging rate, and mechanical shock. Two primary and interconnected degradation modes that affect lithium ion batteries, and have been widely studied is the formation of the Solid Electrolyte Interface (SEI layer) on the electrodes and dendrite growth.

Solid Electrolyte Interface (SEI)

The formation of a passivating film on the battery electrodes caused by a reaction between the organic electrolyte and the electrode material was first realized in the 1970's.[23] This passivating film, however, is not entirely bad. Once formed, it serves to protect the electrodes from further degradation and loss of cycleable lithium due to side reactions between the electrolyte and electrodes. The SEI layer mostly forms during the first charge-discharge cycle.[24] Its formation is a consequence of reactions with the electrolyte solvents and the salt. While its formation does account for approximately a 10% loss in capacity during the formation cycle, due to the reaction consuming lithium, its presence has been acknowledged as essential to the overall operation of the battery.[25] Once the SEI layer is formed, continued growth of the film should theoretically not occur. An optimal SEI layer should have negligible electrical conductivity and high electrolyte diffusion resistance while simultaneously having high lithium ion selectivity and permeability.[23] These characteristics prevent further side reactions since electrons cannot travel through the SEI layer. In reality the SEI layer gradually grows and changes during battery cycling due to electron transfer and exposure to the electrolyte or electrolyte diffusion through the layer to the electrode surface leading to a continuation of side reactions.[26, 27] The continued growth lowers the capacity of the battery and the Coulombic efficiency. However, the growth of the SEI after the formation cycle is significantly less.[23]

The SEI that forms on graphite anodes is of particularly interest as this has been found to be the major cause of SEI related degradation. [28] An SEI-like layer does form on surface of the cathode; however, the effect of this layer on capacity loss and overall battery operational performance is significantly less. [25, 29] SEI on graphite anodes has been studied extensively and found to be affected by a variety of parameters including, but not limited to electrode size and relative geometries (N/P ratio), the current densities that occur in the electrode during operation, and the operating potentials of the electrodes. [26, 27, 29-31] The N/P ratio is the ratio of the capacity of the negative electrode (N) to the capacity of the positive electrode (P). In an ideal battery the N/P ratio would be 1:1. During charge and discharge the capacity of each electrode is fully utilized. However, due to the loss of cycleable lithium during formation cycles and the potential for dendrite growth on graphite anodes the capacity of the graphite anode used in a commercial battery is designed to be higher than the cathode.[25] Obtaining a higher capacity in the anode can be obtained in several ways. The thickness of the anode material can be increased, or the overall surface area of the anode can be increased.[32] However, each method has its drawbacks. An increase in the anode thickness changes the diffusion kinetics, which affects current densities in the electrode and charge rates.[33] Enlarging the surface area means that a larger SEI layer will form to cover the surface of the electrode consuming more lithium, consequently leading to a larger capacity lose during the formation cycle.

The operating voltages of the electrodes govern the formation of the SEI layer and the energies required for the oxidation and reduction reactions. Figure 7 shows the relative energies and potentials for an anode-cathode pair.[23, 34] The anode (μ_A) and the cathode (μ_C) sit at different electrochemical potentials. The stability window of the electrolyte is the difference in energy between the Lowest Unoccupied Molecular Orbital (LUMO) and the Highest Occupied Molecular Orbital (HOMO). If the potential of the anode (μ_A) is above the LUMO energy then the electrolyte will undergo reduction, leading to the formation of the SEI layer. Similarly, if the potential of the cathode (μ_C) is below the HOMO energy, the electrolyte will oxidize. The difference between LUMO and HOMO is the obtainable energy of the cell, E_g. To obtain the highest energy this separation needs to be as large as possible. Organic electrolytes used in lithium ion batteries have oxidation potentials close to 4.7 V vs. Li/Li^+ . The reduction potentials of these electrolytes are around 1.0 V vs. Li/Li^+. For lithium ions to intercalate into the graphite anode the potential of the anode needs to be between 0V and 0.25V. This voltage is outside the stability voltage window of the electrolyte; thus the electrolyte decomposes at the surface of the graphite forming the SEI layer.

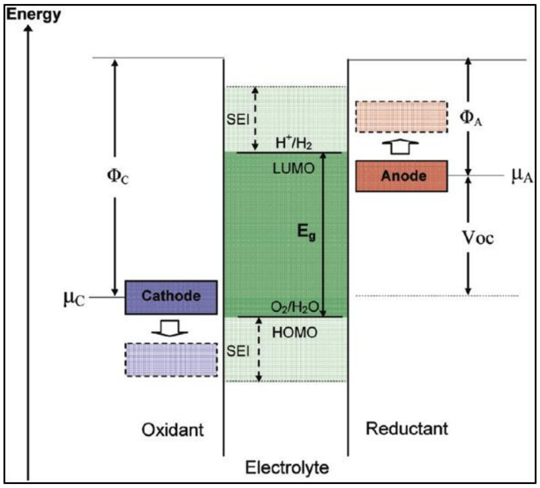

Figure 7. Energy levels and relative voltages for lithium ion battery electrode pair. [23, 34]

In general, the formation of the SEI layer can be broken down into a two-step process. In the first step, the graphite electrode is polarized. The polarization potential causes the reduction of components in the organic electrolyte forming new chemical species. The second step involves the precipitation of the decomposed species. The decomposed species begin to form the SEI layer until all surfaces of the graphite are covered with this passivating film. $LiPF_6$ precipitates as LiF and Li_xPF_y after reduction. Simultaneously, carbonates from the electrolyte precipitate with lithium ions forming Li_2CO_3, lithium akyl carbonate ($ROCO_2Li$), or a similar organic compound. At the surface of the graphite insoluble products such as LiF, Li_2O, and Li_2CO_3 collect forming the SEI layer.[23]

The reduction processes responsible for the formation of the SEI layer take place between 0.2V and 0.8V vs Li/Li^+. Simultaneously lithium ions are intercalating into the graphite structure forming LiC_6. If the reduction and the intercalation rates are too high, the SEI layer may not fully develop. The continuous formation of SEI consumes cycleable lithium and negatively affects the battery capacity. Additionally, the SEI layer serves to protect the battery electrode during operation. An incomplete SEI layer or breakdown in the SEI layer can lead to other detrimental degradation phenomenon like lithium plating or dendrite formation.

Dendrite Formation

Lithium plating or dendrite formation is the deposition of metallic lithium on the surface of the graphite anode, rather than the intercalation of the lithium into the graphite structure. The intercalation potential for lithium ions into graphite is very close to the Li/Li^+ potential. The close proximity of these potentials can cause deposition of metallic lithium onto the graphite electrode depending on the charging conditions.[10] A complete understanding of dendrite formation and growth is currently lacking; however, it is generally agreed factors such as electrode current density, electrolyte composition and concentration, surface morphology, and temperature are the major factors affecting dendrite formation. [35-39]

It is generally agreed that the current densities of the electrode surface play a big role in dendrite formation. Purushothaman and Landau provided a theoretical analysis to describe the conditions of lithium plating.[41] The conditions for lithium plating follow the buildup of lithium that accumulates at the surface of the negative electrode during charge. If the flux of the charge transfer reaction at the graphite/SEI layer is higher than the lithium diffusion flux into the graphite particles then it is likely plating will occur. In 1998, Brissot et al. proposed that the growth velocity of the dendrite is proportional to the local current density. They observed dendrite growth at low current densities ($0.2mA/cm^2$)

and at high current densities (0.7mA/cm^2) and reported a strong dependence between the growth rate and current density.[40] Orsini et al. thereafter reported the morphology of deposited lithium was affected by the current densities and display either moss-like or dendritic (needle-like) structures depending on the current density. Lower current densities resulted in the mossy structure, high current densities lead to the needle-like structure.[41] The difference in structure depending on current density has been further observed.[42]

Integrally connected with the current density of the electrode is the concentration gradient that forms at the surface of the electrode in the electrolyte. The intercalation of lithium ions into the graphite electrode, and the evolution of the SEI layer forms a concentration gradient at the surface of the electrode that is different from the bulk concentration of the electrolyte. Crowther and West reported that the concentration gradient was not found to have a large effect on the initiation of the dendrite; however, after the dendrite precursor has formed on the surface of the electrode, the growth is highly dependent on the availability, or concentration, of lithium in the electrolyte near the surface of the electrode. [43] The mass transport of lithium to the surface is the driving factor for dendrite growth. The growth rate of the dendrite is related to the current density by Eq. 3.[44]

$$i_{tip} = \frac{v_{tip}F}{V_m} \qquad \text{Eq. 3}$$

where:

i_{tip}= current density of dendrite tip
v_{tip} = velocity of dendrite tip (growth rate)
F = Faraday’s constant
V_m= is the molar volume of lithium

Due to the dependence of dendrite growth on the composition and concentration gradient in the electrolyte, some have looked into putting additives into the electrolyte to mitigate or eliminate dendrite nucleation and growth. Electrolyte additives have had the effect of reducing, but not completely mitigating, lithium dendrites. Researchers have found the growth of dendrites is highly sensitive to electrolyte additives.

Wandt et al. reported the addition of fluorotheylene carbonate (FEC) additive helped distribute the occurrence of lithium plating and make it more homogeoues across the electrode. Homogeneous distribution can help reduce areas of high current densities leading to further plating or breakdown of the SEI layer. Furthermore, they noted with the FEC additive the plating was partially reversible, while with their standard electrolyte the plating process was almost completely irreversible.[10] Mogi et al evaluated the effect of three different additives on lithium plating: FEC, vinylene carbonate (VC), and ethylene sulfite (ES). [45] Electrolyte with 5 wt.% of each additive was evaluated across similar cells. They found FEC improved cycling efficiency and was the only additive effective at reducing the deposition and increasing the dissolution of lithium plating. Furthermore, FEC also decreases the lithium needed for the formation of the SEI layer, decreasing the initial capacity loss of a battery.[46]

The microstructure of the negative electrode material, including lattice structure, particle size and shape, affects the characteristics of lithium dendrites. Park et al. studied the effects of lithium intercalation and deposition into graphite that had different surface geometries and particles sizes. Their findings showed the more spherical and smoother the particles were the better the lithium ions intercalated into the graphite structure and the lower the rate of lithium deposition. The graphite particles that had rougher more defined edges, as shown in Figure 8, were more likely to be sites of lithium deposition.[47] The smoother graphite surface structure helped to facilitate lithium intercalation into the bulk of the electrode material, particularly at lower temperatures and enhanced capacity retention.[48]

Figure 8. SEM image of graphite negative electrode (a) natural graphite with natural surface roughness (b) natural graphite prepared by TVD process [49], resulting in smoother particles. The graphite with smoother particles was found to better resist lithium deposition and allow better intercalation of lithium ions.[48]

The temperature at which a battery is charged significantly affects dendrite growth. At lower temperatures lithium ion batteries are more prone to dendrite growth. Love et al. investigated the dendrite growth rate as a function of temperature by observing initiation time, and the number of dendrites formed at ambient and sub-ambient temperatures (-10C-

20C).[36] At lower temperatures the dendrite initiation time decreased and growth rate increased. At lower temperatures dendrite growth is more significant because there is an increased mass transport resistance to lithium ions moving through the electrolyte and a reduced charge transfer resistance due to the thinner SEI layer. Lithium ions favor reducing to metallic lithium, according to Eq. 4, rather than intercalating into the electrode. The diffusion coefficient changes with temperature according to Eq. 5. The lower the temperature, the slower the diffusion. This is schematically represented in Figure 9. The slower diffusion leads to an accumulation of lithium at the surface of the electrode.

$$Li^{+} + e^{-} = Li^{0} \qquad \text{Eq. 4}$$

$$D = D_o \exp(-\frac{E_D}{K_B T}) \qquad \text{Eq. 5}$$

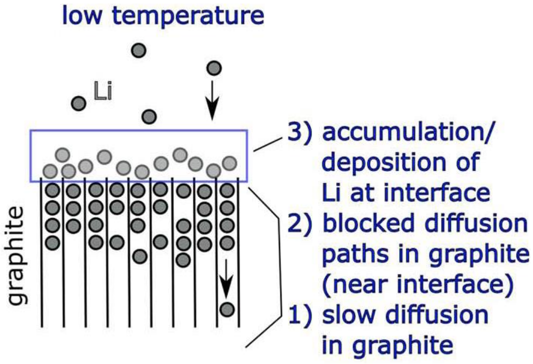

Figure 9. Representation of diffusion processes slowing at low temperatures. Due to the low temperature, the diffusion of lithium into the graphite slows. Lithium ions backup at the surface of the electrode and deposit as metallic lithium rather than intercalating into the electrode. [36]

A critical temperature of -10C was identified as the temperature below which dendrites grow uncontrollably at their testing current of 5 mA/cm^2. Temperature significantly influenced the dendrite morphology. At lower temperature, the moss-like morphology was observed. This was attributed to the faster initiation rate of new dendrites, which subsequently prevents localized current distributions, helping the dendrites spread across the surface of the electrode. At higher temperatures, a more needle-like morphology was observed. [36]

The danger and detrimental effects of dendrites comes from the fact that dendrites can cause internal short circuits, particularly dendrites that have a needle-like morphology. Needle-like dendrites can grow from the negative electrode and connect back to the positive electrode as shown schematically in Figure 10. Short circuits lead to an increase in internal heating which ultimately leads to thermal runaway and catastrophic failure of the battery.[9, 50]

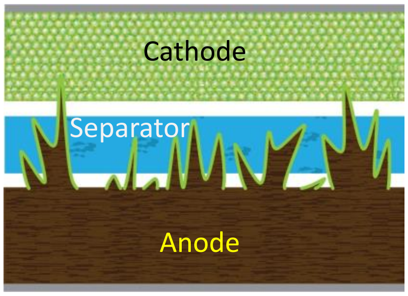

Figure 10. Representation of dendrites growing from the anode, puncturing the separator, and creating an internal short-circuit with the cathode. [11]

Scope of this Work

The objective of this work is to investigate and bring an increased understanding of dendrite growth on graphite electrodes. There are many tools and approaches available to meet this objective the broadest of the tools being computational modeling and lab based experimentation. Both modeling and experimentation can be extremely insightful in trying to understand or answer a problem; however, both also have inherent weaknesses. Modeling can be helpful in building a fundamental understanding of the physics that is behind dendrite growth. It can be used to simulate many different scenarios in very controlled manners. A draw back to modeling is the model will only include and show the physics that is represented by the governing equations included in the model. If key assumptions used in the model are incorrect, or if elements are missing then the model maybe erroneous. Experimental techniques can serve to represent what will actually occur. They can be used to validate computational models and show that our understanding and physical assumptions are correct. Difficulties lie in controlling or setting up experiments to meet circumstances or test scenarios of interest. In the case of dendrites, experimental observation are often difficult due to the many factors such as their size, and reproducibility. Many techniques such as SEM, XRF, and optical microscopy have been used to study the growth of dendrites. Many of these techniques have draw backs in that they are either destructive techniques or they are difficult to setup and require a special setup that does not necessarily mimic the battery as it would be in full operation.

The first part of this work presented in Chapter II seeks to understand and develop a computational model to gain insight into dendrite growth. Development of such a model requires exploring computational analysis methods, techniques, and appropriate verification and validation of the code. The model approach is relatively simple, being based off models found in the literature. It presents a one-dimensional approach to gaining insight and understanding of fundamental physics behind needle-like dendrite growth. Appropriate model verification, validation, and results are discussed.

The second part of this work presented in Chapter III and Chapter IV includes the experimental aspects used to study dendrites. Chapter III documents characterization of CMS graphite, a common anode material. To understand the dendrite growth on graphite, it is first important to characterize the graphite that will be used experimentally and such analysis can increase understanding to how lithium intercalates into the graphite under normal operating conditions and without dendrite formation. Chapter IV delves into using Electrochemical Impedance Spectroscopy (EIS) to detect the formation of dendrites on the graphite electrode. Traditional methods such as SEM, XRF, and optical microscopy require opening the battery to look at the dendrites, thus destroying the battery and preventing further testing. In addition, any information collected is done ex-situ and provides no information about the dendrite growth process across different states-of-charge. EIS was used to investigate the electrodeposition of lithium -dendrite growth- on graphite electrodes, quantified through equivalent circuit analysis. Finally, overall conclusions and recommendations are presented in Chapter V.

CHAPTER II

UNDERSTANDING DENDRITE GROWTH THROUGH A FUNDAMENTAL MODEL

Background

Computational modeling can provide great insight and understanding into dendrite growth. Computational modeling offers control and repeatability that is not always available through experimental methods. It is possible to precisely control specific parameters and look at the effect of just one parameter or constraint on the system. The limitations of computational modeling are the model only represents the physics that is included in the model. If incorrect assumptions are made, or key relations are excluded from the model or not correctly included then the model is completely erroneous.

Over the past 30 years, many models have been proposed to simulate dendrite growth and bring an increased understanding to their occurrence. Barton and Bockris created one of the earliest dendrite models. [44] They created a model to study the conditions for dendrite initiation and growth of silver deposition in well-understood electrolytes. Their model assumed surface tension was a key driving force in dendrite propagation. They assumed surface tension could be calculated by correlating it with an overpotential term caused by pressure variation inside and outside the dendrite tip. Their calculations predicted a parabolic shape of the dendrite tip. Barton and Bockris suggested that during the initiation stage the dendrite tip formed on the electrode with its own spherical diffusion layer. The dendrite tip protruded from the surface of the electrode and grew through the diffusion layer of the electrode. Barton and Bockris proposed that growth is faster on protrusions from the electrodes because spherical rather than linear diffusion conditions dominate. Over time, a narrowing of the dendrite tip might occur due to the larger spherical diffusion flux. Their model incorporates surface forces to resist infinite dendrite tip thinning.

Expansion of the Barton and Bockris model has taken place over the years. Diggle et al. extended the Barton and Bockris model by using a Butler-Volmer kinetic expression and relaxing the assumption that the dendrite is static. [51] Both Diggle et al. and Barton and Bockris models were found to compare well with experimental data. Monroe and Newman built off the Diggle et al. and Barton and Bockris models, but made some simplifying assumptions.[52] Their model assumes a dendrite is already protruding from the surface. They assume only one dendrite or that the dendrites are far enough apart that they do not affect each other and the dendrites are small enough that their presence does not greatly affect the concentration and potential profiles of the cell.

Generally, most models are mechanistic models meaning they operate by describing how the system should work, i.e. solving the problem through the governing physical equations. Most models start by solving for the concentration profile near the surface of the electrode. From the concentration near the electrode surface, it becomes possible to derive a relation for the potential profile by assuming a Butler-Volmer or Tafel kinetic relationship. Generally, it is accepted that the current density is the primary suspect for dendrite growth, and can be related to deposition of lithium through Faraday's law.[53]

Work by Akolkar expands on the Monroe and Newman model by looking at relations between the overpotentials that develop due to dendrite growth and the dendrite tip current density, which can be related to tip growth. [44, 52, 53] The overpotential analysis approach simplifies the otherwise computationally intensive approach by Monroe and Newman. The work presented in this chapter investigates the work done by Akolkar and builds a similar model to gain a fundamental understanding of dendrite growth physics, an understanding of the intricacies involved in model development, and the importance of model verification and validation.

Model Development

The development of a computational model begins long before a programmer takes to a computer and keyboard and begins typing out lines of code. To be successful and have a final product (i.e. a working computer code) that produces a meaningful and effective model of a physical system you first have to start with a well posed question: what is it you wish to do? Outlining the fundamental questions to answer is the first step. A detailed outline allows you to determine all the physical characteristics of a particular situation you wish to represent. This step requires gathering and solving for all governing equations, which will be used to represent a physical system through the computer model. This process requires making assumptions and simplifications: compressibility vs. incompressibility, constant boundary conditions vs. flux boundary conditions, linear-terms vs. non-linear terms, etc. All assumptions and simplifications need to be accounted for and justified for your own understanding, and for a future user who needs to understand the applications and limitations of the model. The aforementioned process constitutes the *conceptual model*.[54] The conceptual model accounts for the physics represented, any assumptions the programmer of a code makes, and the codes applicability and overall purpose. It is important to keep in mind a model can only solve for and show the physics represented by the equations it solves. This becomes increasingly important to remember when trying to compare model results to experimental data.

Once a conceptual model is developed, the numerical modeling can begin. The *numerical model* involves the details of solving the conceptual model i.e. the programming aspects. The programming language, input parameters, displays the outputs, the numerical methods and solvers, and many other details have to be decided.

Verification and Validation

The correctness of a numerical code and having confidence that the code is both solving the right equations and solving them correctly is of the utmost importance. The process of checking code is cast into two steps: *verification* and *validation*. [54]

- *Verification* is solving the equations right
- *Validation* is solving the right equations

Verification and validation are important processes that every programmer and user of numerical codes should understand and practice; doing so will help ensure that obtained results are meaningful. By their nature, verification and validation are very different; however, the two are complimentary to each other and the order execution of the two processes does matter.

Verification is strictly an exercise in mathematics. It is important to note that the verification process does not necessarily encompass source code analysis; reading through all the lines in a program does not count as verification (nor would you want to have to do that). Wide spread usage or even broad publication does not classify as code verification either. Rather, code verification as defined by IEEE is “a formal proof of program correctness”.[55] Obtaining this “formal proof” is highly dependent on the code being used and the complexity of the equations being solved. Verifying a code that solves an equation, or series of equations, with an exact analytical solution is fairly straight forward. For example, a code that solves a classically defined Newtonian mechanics problem where a body falls without drag, or slides across a frictionless surface, can easily be verified. The analytical solutions to those governing ordinary differential equations are simple to obtain and can be used to verify the code. Codes that solve equations where an exact analytical solution is either not known or too difficult to obtain makes it much harder to obtain “a formal proof of program correctness”. For example, verifying a code that solves the non-steady-state heat equation where the thermal diffusivity is not a constant, but a function of either time, position, or both is a more difficult code to verify. [56, 57]

Validation refers to the science or engineering aspects involved with a code. As defined by Mehta, validation concerns: [57]

> *“the process of assessing the credibility of the simulation model with its domain of applicability, by determining whether the right simulation model is developed and by estimating the degree to which this model is an accurate representation of reality from the perspective of its intended uses.”*

Validation is tricky because it often involves comparing the results of a code with experimental data. Experimental data frequently does not agree with itself, and can have large margins of error. Typically, validation of codes is also an ongoing process. Experiments can improve leading to refinement in code parameters.

Verification (at least for the first version of a code) is a process that can be completed. Verification of any code must be completed before attempting any validation. Skipping the verification of a code can lead to drawing erroneous conclusions from model results (that may align with experimental data!) and cause much future turmoil and complications. After verification is performed, it will no longer need to be repeated unless major code modifications are performed.

Generally speaking, there are five categories into which errors are made during code verification:[58]

1. In code generation (either by hand or using computer symbolic manipulation)
2. In code instructions (in a user manual)
3. In problem set-up
4. In defining and coding a test case (analytical solutions are often more difficult to code than numerical solutions)
5. In interpretation of code results

The authors of the code typically cause the first two categories. These errors can be easily corrected and removed. The user can cause categories three through five. Thus, there is always some degree of code verification necessary.

Dendrite Model Development

The dendrite model is based upon the following:

1. It is assumed that a dendrite precursor exists on the surface of the electrode. Thus, the model will not include or be representative of the nucleation of the dendrite.

2. A single needle-like dendrite will be modeled. It is assumed the dendrites are small enough and/or are far enough apart that they do not appreciably affect each other.
3. The time-dependent concentration distribution near the surface of the electrode is computed numerically by solving the mass transport equation inside the diffusion boundary layer. [59]
4. The dendrite propagation rate is directly dependent on the tip current density [44, 52, 53]. The tip current density is calculated by analysis of the overpotentials that develop at the dendrite tip and on the electrode surface.
5. Constants used assume a $LiPF_6$ electrolyte.

The initial model setup is illustrated in Figure 11. A dendrite precursor exists on the surface of the electrode. The precursor is assumed to be spherical in shape with a radius r. The current density of the surface of the electrode is denoted by i_f and the current density on the tip of the dendrite is denoted i_t. A concentration gradient of lithium ions exists in the diffusion layer between $Z=0$ and $Z=\delta$. Delta denotes the thickness of the diffusion layer where the concentration at $Z= \delta$ is the bulk concentration. An unsteady-state transport model governs lithium ion concentration. Since $r<<\delta$ the dendrite does not appreciably effect the lithium ion concentration profile in the diffusion layer.

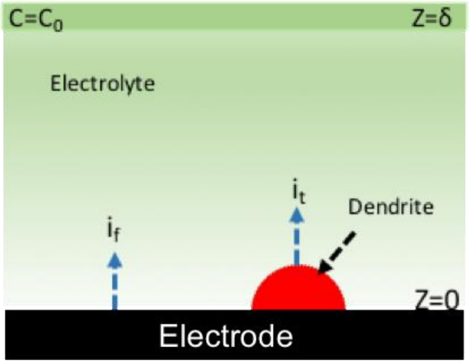

Figure 11. Initial conditions for the dendrite model. A spherical dendrite precursor of radius *r* exists on the surface. The model solves for the concentration gradient near the surface between Z=0 and Z=δ. The surface current (i_f) and tip current (i_t) are calculated be relating the overpotentials that develop.

The unsteady-state transport model is governed by the convention diffusion equation for a binary electrolyte represented in Eq. 6.[60]

$$\frac{\partial C}{\partial t} + \vec{V} \cdot \nabla C = \nabla \cdot (\mathrm{D}\nabla\mathrm{C}) - \frac{i \cdot \nabla t_+}{nZ_+F} \qquad \text{Eq. 6}$$

where:

C = concentration (mol/cm^3)
t = time (second)
D = diffusion coefficient (cm^2/s)
i = current density (mA/cm^2)
t_+ = lithium ion transport number
$\vec{V}$= velocity of fluid
Z_+= charge number
F = Faraday’s constant (96,487 C/mol)
n = valence number; 1

The first term on the left hand side of the equation represents the time-dependent concentration. The second term represents the convective transport inside the diffusion boundary layer. Inside the boundary layer this term is negligibly small and can be taken as zero.[53] The first term on the right hand side of the equation represents the diffusion transport. The second term represents the ionic migration. In typical organic electrolytes the variation of the lithium ion transport number with salt concentration is negligible.[61] The transport model can be reduced to Eq. 7. In one dimension, this equation can be simplified according to Eq. 8.

$$\frac{\partial C}{\partial t} = \nabla \cdot (D \nabla C)$$ Eq. 7

$$\frac{\partial C}{\partial t} = \frac{\partial}{\partial z}(D\frac{\partial C}{\partial z})$$ Eq. 8

In Eq. 8 the diffusion coefficient can be taken as a constant or as a function of the concentration. Stewart and Newman provide a relationship for the diffusion coefficient with respect to concentration for $LiPF_6$ electrolyte, Eq. 9. [59]

$$D = ae^{-bC}$$ Eq. 9

For $LiPF_6$ it was experimentally determined a=2.582 x 10^{-5} and b = 2.856. The units for D is cm^2/s and C is mol/L. The full form of the mass transport equation is given in Eq. 10.

$$\frac{\partial C}{\partial t} = \frac{\partial}{\partial z}(ae^{-bC}\frac{\partial C}{\partial z})$$ Eq. 10

The boundary conditions used to solve Eq. 10 are as follows:
t = 0; $C = C_0$
Z= δ; $C = C_0$
Z= 0; $D\frac{dC}{dz} = \frac{i_{f(1-t_+)}}{F}$

where:

i_f is the current density of the flat electrode surface
C_o is the initial bulk concentration

The current density of the flat electrode surface can be taken as the average operating current density (i_{avg}) when the growth of dendrites occurs on a small fraction of the electrodes surface. If the current density of the electrode surface approaches the limiting current density, the lithium ion concentration near the surface of the electrode approaches zero. Conversely, if the current density is well below the limiting current density the concentration at the surface of the electrode is close to the bulk current density. [53]

The bulk concentration of lithium ions in the electrolyte depends on electrolyte composition. A value of one molar was chosen. The thickness of the diffusion boundary layer can be measured experimentally. Ota et al. determined the thickness to be approximately 400μm. [62] All constants used are summarized in Table 1.

Table 1. Constants used in the mass transport model

Bulk concentration (C_0)	0.001mol/cm^3
Flat current density (i_f)	10 mA/cm^2
Boundary layer thickness (δ)	400μm
Lithium ion transport number (t_+)	0.2

The concentration of the lithium at the surface of the electrode can be utilized to determine the current density of the dendrite tip. The relationship between concentration and current density can be derived from an analysis of the overpotential that develops at the electrode surface. The total overpotential (η_{tf}) that develops at the surface of the electrode is the sum of the activation overpotential (η_{af}) and the concentration overpotential (η_{cf}) when a constant current density (i_f) is applied at the electrodes surface. Utilizing Tafel kinetics for the activation overpotential, the total overpotential can be represented according to Eq. 11. The negative sign before the concentration overpotential terms is used because it is assumed all overpotentials are positive.[53]

$$\eta_{tf} = \eta_{af} + \eta_{cf} = \frac{RT}{\propto_c F}\ln\left(\frac{i_f}{i_o}\right) - \frac{RT}{nF}\ln\left(\frac{C_e}{C_o}\right) \qquad \text{Eq. 11}$$

where:

i_o= exchange current density
α_c= cathodic transfer coefficient
C_e= concentration at the surface of the electrode
R= gas constant
T= temperature

At the dendrite tip, the total overpotential (η_{tt}) is the sum of the activation overpotential at the tip (η_{at}), the concentration overpotential at the tip (η_{ct}), and the surface energy of the tip (η_{st}). The overpotential due to surface energy is directly proportional to the surface tension at the electrode/electrolyte interface (γ) and inversely proportional to the dendrite tip radius (r). The total overpotential at the dendrite tip can be represented according to Eq. 12.

$$\eta_{tt} = \eta_{at} + \eta_{ct} + \eta_{st} = \frac{RT}{\propto_c F}\ln\left(\frac{i_t}{i_o}\right) - \frac{RT}{nF}\ln\left(1 - \frac{i_t}{i_{lt}}\right) + \frac{2\gamma K}{nFr} \qquad \text{Eq. 12}$$

where:

i_t= tip current density
K= molar volume of lithium
i_{lt} = limiting current density at dendrite tip

At the tip of the dendrite, lithium ion diffusion follows a spherical geometry versus at the surface where linear diffusion occurs.[53] The limiting current density of the tip can be written:

$$i_{Lt} = \frac{nFDC_t}{(1-t_+)r} \qquad \text{Eq. 13}$$

where:

C_t= concentration of lithium at the dendrite tip
r= radius of dendrite tip

Substituting i_{lt} into Eq. 12 results in Eq. 14.

$$\eta_{tt} = \frac{RT}{\propto_c F}\ln\left(\frac{i_t}{i_o}\right) - \frac{RT}{nF}\ln\left(1-\frac{i_t(1-t_+)r}{nFDC_t}\right) + \frac{2\gamma K}{nFr} \qquad \text{Eq. 14}$$

The potential applied to the electrode surface with respect to the Li/Li$^+$ reference is V. By definition V-ϕ_f =η_f and V-ϕ_t =η_t for the electrode and dendrite tip. The difference in potential in solution near the dendrite tip (ϕ_t) and the potential in solution near the electrode surface (ϕ_f) is equal to the difference in overpotentials.

$$\eta_{tt} - \eta_{tf} = \phi_t - \phi_f = \Delta\phi \qquad \text{Eq. 15}$$

The difference in net overpotential at the electrode surface and that at the dendrite tip is equal to the solution potential difference $\Delta\phi$ between the flat surface and the dendrite tip. This potential difference can be estimated by $\Delta\phi = i_{avg}\frac{L_c}{K}$. The characteristic length is taken to be ~10μm, K as 10mS/cm, and i_{avg} as 10mA/cm^2. This gives $\Delta\phi$~1mV, which is negligible in comparison to the net overpotential, which are on the order of volts. Thus, the overpotential at the surface can be equated to the overpotential at the dendrite tip according to Eq. 16.

$$\eta_t = \eta_f \qquad \text{Eq. 16}$$

$$\frac{RT}{\propto_c F}\ln\left(\frac{i_f}{i_o}\right) - \frac{RT}{nF}\ln\left(\frac{C_e}{C_o}\right) = \frac{RT}{\propto_c F}\ln\left(\frac{i_t}{i_o}\right) - \frac{RT}{nF}\ln\left(1 - \frac{i_t(1-t_+)r}{nFDC_t}\right) + \frac{2\gamma K}{nFr}$$

The second term on the right hand side of the equation represents the concentration overpotential at the tip (η_{Ct}). The dendrite precursor must grow faster than the flat surface, thus this term must be negligibly small. This is met physically because the radius of curvature of the dendrite tip is usually on the order 10^{-5} to 10^{-4} cm releasing the tip from mass transport limitations.[44, 51, 53] This phenomenon has also been observed in zinc and silver systems. Furthermore, as the dendrite tip grows it experiences an increase in lithium concentration near the tip further diminishing the effect of the concentration overpotential.[53] Thus, Eq. 16 simplifies to Eq. 17.

$$\frac{RT}{\propto_c F}\ln\left(\frac{i_t}{i_f}\right) + \frac{RT}{nF}\ln\left(\frac{C_e}{C_o}\right) + \frac{2\gamma K}{nFr} = 0 \qquad \text{Eq. 17}$$

The concentration near the electrode surface (C_e) is determined from the mass transport model. The tip current density (i_t) can be calculate as a function of dendrite radius (r). In this work a tip radius of $r=10^{-4}$ cm was used. From the tip, current density Faraday's law can be used to compute the dendrite length as a function of time.

$$L = \frac{M}{n\rho F}\int_0^t i_t dt \qquad \text{Eq. 18}$$

The aforementioned governing equations and assumptions constitute the full dendrite model. The equations will be solved using Python.

FiPy

Solving the partial differential equations that will be utilized in this model can be accomplished through a variety of numerical techniques. There exist many different numerical methods, which can be used to obtain approximate solutions to these very complex equations. The discussion of these various techniques is beyond the scope of this thesis, but can be found in literature.[63-65] This work will discuss the implementation of one numerical solver called *FiPy* which was used to obtain solutions to the partial differential equations in the dendrite model.

FiPy is an object oriented, partial differential equation (PDE) solver written in Python. *FiPy* was developed by NIST to be a tool for scientists and engineers to use in solving the partial differential equations. The task of solving PDE's is almost ubiquitous with solving many of today's complex science and engineering problems. This task, however, can be rather daunting for many and can require an advanced background in mathematics. *FiPy* is a tool that can be used to make the task of solving PDE's less daunting. It is an object-oriented solver that relies on the standard finite volume approach. The *FiPy* framework allows the programmer to easily include terms for transient diffusion, convection, and standard sources. The framework is designed to be easy to use, highly customizable, and is capable of providing solutions to an arbitrary combination of coupled, elliptical and parabolic PDE's. [66]

The Finite Volume Method (FVM) as implemented by *FiPy* divides the domain into discrete finite volumes over which the state variables are approximated with linear or higher order interpolations. The derivatives of each term are approximated through discretization across the volume. The discretization varies based upon whether a transient, convection, diffusion, or source term is being utilized. Rigorous mathematical explanation of the discretization technique for each term can be found in the *FiPy* user's manual. [66] Discretization permits the approximation of the continuous solution as a set of discrete linear equations that can be solved to obtain the dependent variables. The general form of each of the terms is shown in Eq. 19.

$$\underbrace{\frac{\partial(\rho\phi)}{\partial t}}_{\text{transient}} + \underbrace{\nabla\cdot(\vec{u}\phi)}_{\text{convection}} = \underbrace{\left[\nabla\cdot(\Gamma_i\nabla)\right]^n}_{\text{diffusion}}\phi + \underbrace{S_\phi}_{\text{source}} \qquad \text{Eq. 19}$$

The FVM requires the discretized solution domain be divided into non-overlapping polyhedral elements or cells called a mesh in *FiPy*. A mesh is constructed from three components: vertices, faces, and cells. In the FVM approach, the variables of interest are averaged over the volume elements. In *FiPy* these volume elements are the cells, which are depicted in Figure 12. The solution to the PDE is approximated in each cell. These approximations followed by an iterative solving across all the cells make up the entire mesh, which constitutes an approximation of the solution to the PDE.

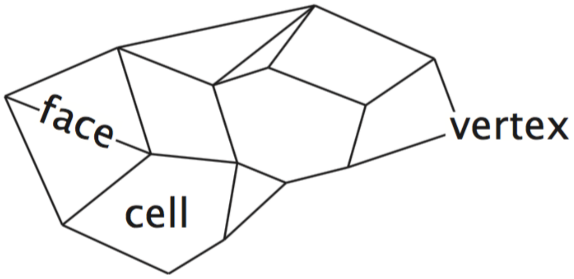

Figure 12. Components that make up a mesh used by *FiPy* [66]

Method of Manufactured Solutions (MMS)

Verification for complex codes that solve one or many equations (ODEs PDEs etc.) can take several forms. Systematic Grid Convergence studies, Richardson Extrapolation, Grid Convergence Index (GCI), and the Method of Manufactured Solutions (MMS) are all techniques with varying applicability that can be used in the verification process of numerical codes. A detailed discussion of each method is beyond the scope of this thesis, but can be found other places[54]. The method of interest for this work is the Method of Manufactures Solutions (MMS).[67, 68]

MMS provides a means to verify the solutions of a numerical code by providing an exact analytical solution. As the name implies this method allows you to manufacture the solution to your problem. The manufactured solution has no physical meaning or representation, but that is perfectly acceptable. The process of verification is simply a mathematical exercise. By picking an appropriate manufactured solution, it is possible to rigorously evaluate the mathematics, including all the derivative terms of the governing equations, of a numerical code. When properly implemented MMS provides a straightforward and general procedure for generating solutions that can be used to verify codes and check for possible solution errors.

The avenues that a code could be caused to return an incorrect answer are almost limitless. Errors can result from incorrectly applied boundary conditions (Dirchlet, Neumann, Robin, etc.), from incorrectly solving when expanding dimensions (2-D, 3-D codes), incorrectly applying initial conditions, poorly specifying a domain, or incorrect discretization are just a few examples of where codes can generate errors. The MMS procedure is general enough that it can be applied to test all the aforementioned causes of error. MMS provides an exact solution to some PDE by solving the problem backwards.

Suppose the problem you are solving is a differential equation of the form

$$Du=g$$

D is the differential operator, **u** is the solution, **g** is the source term. Traditionally to find an exact solution one chooses the function **g** and then using methods from classical applied mathematics and inverts the operator to solve for **u**. In MMS one first manufactures the solution **u**, applies **D** to **u** to find **g**. This procedure of going backwards is typically much easier. In addition, this manufactured solution is a fully general solution to the initial equation and can be solved by the code. A general solution to the equations is desired because you want to test all portions of the code.

To begin MMS you need to set the mathematical model in the form

$$L(u)=0.$$

L() is the differential operator and **u** is the dependent variable. Next, choose the analytical form of the manufactured solution **u.**

$$\text{Let } u=q \text{ and } g=L(q)$$

$$\text{Then: } L(u) = g= L(q)$$

The following examples are useful to illustrate the power of MMS and apply this theory. The two examples apply MMS to two forms of the diffusion equation, which is what needs to be solved for the mass transport part of the dendrite model. The first example assumes steady-state diffusion. The second example assumes non-steady-state diffusion. Both examples assume a constant diffusion coefficient.

Example 1.

We desire to manufacture a solution to the equation

$$0 = D\frac{d^2c}{dx^2}$$

Where **D** represents the constant diffusion coefficient, **x** is the position in a Cartesian system, and **c** represents the concentration. This satisfies the form L(u)=0. We chose a solution of the form:

q(x)=A + sin(Bx)

Calculating the derivatives with respect to x gives:

$$\frac{dq}{dx} = Bcos(Bx)$$

$$\frac{d^2q}{dx^2} = -B^2\sin(Bx)$$

Now by the procedure of MMS **q(x)** is a solution to the equation

$$0 = D\frac{d^2q}{dx^2} + g$$

Where we can find the source term **g** is equal to:

$$g = DB^2\sin(Bx)$$

Thus, we have an analytical solution to our differential equation with the appropriate source terms. The differential equation can be solved using a numerical code. The numerical solution can be compared with the analytical solution to check the code for errors.

Example 2:

Now let us increase the complexity of the differential equation and show the ease and power of the method of manufactured solutions. We now desire to apply MMS to the diffusion equation of the form:

$$\frac{\partial c}{\partial t} = D\frac{d^2c}{dx^2}$$

Where **D** represents the constant diffusion coefficient, **x** is the position in a Cartesian system, **c** represents the concentration, **t** represents the time. To satisfy the form L(u)=0 the equation becomes:

$$\frac{\partial c}{\partial t} - D\frac{d^2c}{dx^2} = 0$$

Let us choose a manufactured solution of the form:

$$q(x,t) = e^{-t}\sin(B\pi x)$$

We need to calculate the appropriate partial derivatives with respect to **t** and **x**.

$$\frac{\partial q}{\partial t} = -e^{-t}\sin(B\pi x)$$

$$\frac{\partial^2 q}{\partial x^2} = -e^{-t}B^2\pi^2\sin(B\pi x)$$

Therefore, **q(x)** is a solution to the equation

$$\frac{\partial q}{\partial t} - D\frac{d^2q}{dx^2} + g = 0$$

Where g is equal to:

$$g = -e^{-t}\sin(B\pi x) + De^{-t}B^2\pi^2\sin(B\pi x)$$

The constants A and B can be chosen based upon the initial condition and boundary conditions. B primarily functions as a scaling coefficient to scale the features of the sine function to the domain of interest. Boundary conditions need to be applied with care when using MMS as the boundary conditions (depending on the manufactured solution chosen) may become a function of time and or space. This is the reason, in Example 2, a manufactured solution of the form q= T(t)X(x) is chosen.

Boundary Conditions are an important aspect of any numerical code and can frequently be a source of error. The beauty of MMS is boundary conditions are not solution dependent; different types of boundary conditions can be applied to the same manufactured solution. Below are examples of Dirichlet and Neumann boundary conditions for the examples above on a unit domain.

Dirichlet $Q= q(x,y,z,t)$

Neumann $\frac{\partial Q}{\partial n} = q(x, y, z, t)$

Example 1:

Dirchlet: Left= A | Right = A + sin(B)

Neumann: Left = Bcos(B)| Right= Bcos(B)

Example 2:

Dirchlet: Left= 0 | Right=0

Neumann: Left= $B\pi e^{-t}$|Right= -$B\pi e^{-t}$

It is possible to pick a poor manufactured solution that will either not properly exercise all the terms in the governing equation, or be of a form that is difficult to evaluate at the boundaries. The following lists some general guidelines that should be followed when manufacturing a solution.[68]

1. Manufactured solutions should be composed of smooth analytic functions like polynomials, trigonometric functions, exponential functions. Smoothness is essential (no infinite series solutions).
2. The solution needs to be general enough to exercise all the terms of the differential.
3. The solution needs to have a sufficient number of non-trivial derivatives. This is why trigonometric and exponential functions are often used because their infinite differentiability allows for the exercising of higher order derivatives that may appear in the governing equation.
4. A solution derivative should be bounded by a small constant. This ensures the solution is not strongly varying in time or space.
5. The manufacture solution should not prevent the code from running successfully to completion during testing. i.e. work with assumptions that meet the criteria of the code. Things are positive when necessary, time sensitive, and scale sensitive.
6. The solution should be constructed such that the differential operators in the PDE make sense.

Method of Manufactured Solution Results

The code written to solve the mass transport equation, Eq. 10, was verified using MMS under the aforementioned circumstances. The results of this verification are shown in Figure 13. The code was verified to return the correct solution within 1e-3 of the analytical solution.

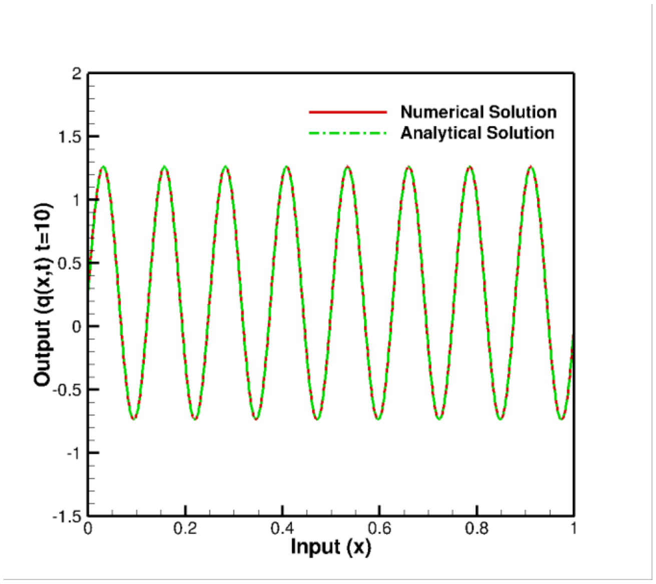

Figure 13. Shows the verification of the non-steady state, non-linear code utilized to solve the mass transport part of the dendrite model, Eq. 10. The manufactured solution $q(x,t)=e^{-t}\sin(B\pi x)$ was chosen. The two solutions match very well to a verified tolerance of 1e-3.

Dendrite Model Results

The calculations from the mass transport part of the dendrite model are shown in Figure 14. The parameters used are given in Table 1. Initially the concentration across the boundary layer is uniform. Once the current is applied to the electrode, representing charging, the concentration of lithium near the surface of the electrode begins diminishing, representing intercalation of lithium into the electrode. Knowing the concentration of lithium at the surface of the electrode as a function of time Eq. 17 can be utilized to solve for the dendrite tip current density. As shown in Figure 16 the dendrite tip initially has a current density close to the current density of the electrode surface. As time evolves and more charge is passed through the electrode the current density of the tip increases slightly. This supports the thought that an increase in the current density of the dendrite tip leads to growth. Utilizing Faraday’s law according to Eq. 18 it is possible to relate the charge passed to the growth of the dendrite, this is illustrated in Figure 15. Nishikawa et al. provides experimental data for the growth of dendrites. Their experimental data is represented by the gray shaded region in Figure 15. The shaded region represents the spread in their experimental data. The results from the model fall in the lower portion of their experimental data.

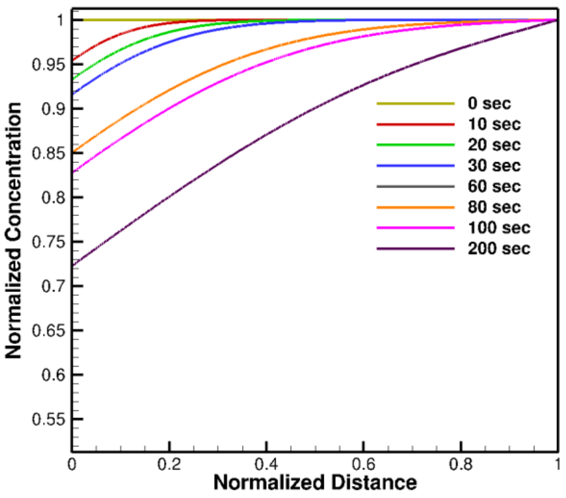

Figure 14. Concentration profile at with an electrode current density of 10mA/cm^2

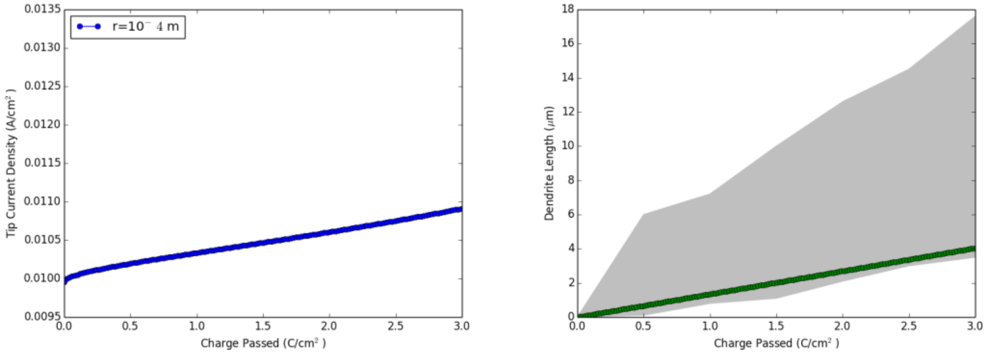

(a) (b)

Figure 15. (a) the dendrite tip current density as charge is passed, with a surface charge density of 10mA/cm^2 (b) the dendrite length relative to the amount of charge passed. The green line shows the model results, the gray region represents measured dendrite lengths presented Nishikawa et al.

Summary

Modeling can be a powerful tool to increasing understanding of a physical situation and provide keen insight. The objective was to understand and develop a computational model of dendrite growth. The development of a computational model consists of many steps, which are important to follow to ensure model validity and understanding.

The model development began with investigating prior work to build an understanding and foundation. Following the background review and based off a particular model, a plan and the conceptual model was outlined. Key assumptions and governing equations were established that would be the framework of the model. From the conceptual model, the numerical model was developed using Python and supporting libraries, *FiPy,* to solve the necessary governing equations. The steps appropriate for code verification and validation were undertaken to ensure that both the right equations were being solved and that they were being solved right. Finally, a select set of input parameters were run through the model and the model output was found to be comparable with experimental data. Discrepancies that the model data has from experimental data likely rise from the single dendrite assumption, especially when modeling different electrode current density. At low current densities, the needle-like dendrite structure is expected experimentally. At higher current densities, the bush-like dendrite structure is common, which the model would have issues properly representing. Overall, the work presented in this chapter provides a solid foundation for understanding and creating a computational model. The intricacies of model development, revision, and success were a major part of this work.

CHAPTER III

CHARACTERIZATION OF CMS GRAPHITE ANODE MATERIAL

Motivation

The electrochemical processes that occur inside the battery and their performance – efficiency – is highly material dependent. Graphite is a typical anode material and is chosen for several reasons.[69] First, its crystal structure lends itself to holding lithium, and the lithium intercalation into graphite is a favorable process. [70] Secondly, the intercalation/deintercalation of lithium with graphite is a highly reversible process. The intercalation of lithium ions into graphite is shown schematically in Figure 16. Third, graphite has good electronic conductivity and a low electrochemical voltage compared to Li/Li^+. [70] Fourth, during the lithium intercalation/deintercalation the volume change is less than 9%. [23, 71]

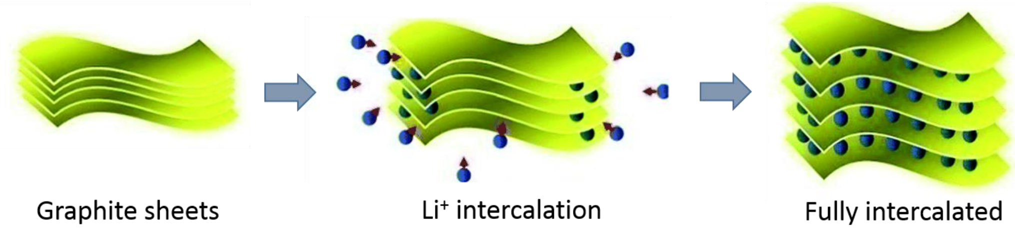

Figure 16. The process of lithium intercalating into the graphite anode during charging. Initially pure graphite is present. Lithium ions begin entering the graphite structure and filling the interstitial positions between carbon atoms. The intercalation of Li^+ into graphite continues until the interstitial sites are filled with lithium.[72]

Graphite typically has a hexagonal –Bernal—structure as shown in Figure 17. [17] Carbon stacks in an ABABA sequence. However, graphite can also take a rhombohedral form, characterized by ABCABC stacking sequence. The latter, less common form, is produced by using mechanical grinding or ultrasonic treatment.[17] Lithium intercalation into graphite changes based upon the structure. [17, 49, 73]

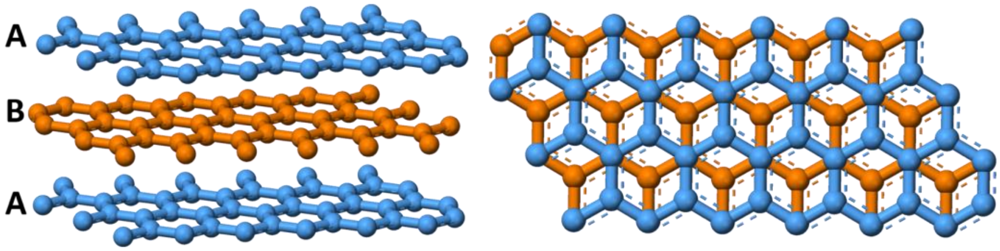

Figure 17. Typical structure of hexagonal – Bernal – graphite. The stacking order is ABABA. Lithium ions intercalate into the structure and sit in the interstitial sites.

The structure of graphite allows for a very high theoretical packing of lithium in the form LiC_6. The theoretical specific capacity is 370 mAh/g.[71] In practice a graphite electrode does not obtain this theoretical specific capacity. The experimentally obtainable capacity of an electrode is dependent upon temperature, composition of the electrode sheet, treatment during fabrication, and many other factors.[74] Due to the variability of the actual specific capacity for an electrode sheet it is important to characterize the specific graphite prior to usage.

Cell Fabrication

The cells utilized in all experiments in this work were fabricated in-house with commercially available electrode sheets.[75] The manufacturer provides approximate specifications for the electrode sheet, presented in Table 2.

Table 2. Electrode sheet information provided by MTI

Electrode sheet	**Material**	**Specific capacity**	**Active material density**	**Active material proportion in powder**
Anode	CMS graphite on copper foil	330 mAh/g	60 g/m^2	94.5%

The electrodes for the coin-cells were punched from the electrode sheets using a leather punch set shown in Figure 18. The punch sizes available range from 1/8 inch to 1 inch.

Figure 18. Punch set utilized for creating the electrodes used in coin cells.

Using the information provided by the material data sheet [75], it is possible to calculate a theoretical capacity for a given electrode size, according to Eq. 20.

$$Q = \rho_{AM} A_{Electrode} (\%AM) Q_{Spec} \qquad \text{Eq. 20}$$

where:

Q is the theoretical capacity of the punched electrode (mAh)
ρ_{AM} active material density (g/m^2)
$A_{Electrode}$ is the area of the electrode (m^2)
%AM is the percent of active material present in the powder,
Q_{Spec} is the specific capacity of the active material (mAh/g)
For each punch size the theoretical capacity was calculated as shown in Table 3

Table 3. Theoretical capacities (mAh) of anode electrode at different punch sizes made from MTI sheets calculated using Eq. 20.

Punch Diameter (in)	Anode Capacity (mAh)
1/8	0.15
3/16	0.33
1/4	0.59
5/16	0.93
3/8	1.3
7/16	1.8
1/2	2.4
9/16	3.0
5/8	3.7

The cells were assembled using 2032-coin cell hardware. The ½ inch punch was used to make the electrodes. This punch was chosen because of the nominal 2.4 mAh theoretical capacity and this size fits well in the geometry of the 2032-coin cell case.

The electrodes were punched from the electrode sheet as demonstrated in Figure 19. The mass of each electrode was recorded using a OHAUS AX224/E analytical scale, which reports to 0.1 mg with an accuracy of ± 0.2 mg and maximum capacity of 220 g. All cell fabrication was completed in an argon glove box, shown in Figure 20. The components used in the assembly of the cell are shown schematically in Figure 21. First, the punched electrode is placed coated side up in the case. A small amount of electrolyte is added to cover the electrode and the bottom of the case. A BASF manufactured lithium hexafluorophosphate diethylcarbonate electrolyte was used for all cells. A ¾ inch punched 25μm Trilayer polypropylene-polethylene-polypropylene membrane separator manufactured by Celgard is placed over the electrode to prevent physical contact between the graphite electrode and the second electrode. Lithium metal is used as the second electrode. The use of lithium metal as an electrode, as opposed to lithium cobalt oxide ($LiCoO_2$) or another commercially common electrode reduces the possible electrochemical processes and side reactions that can occur inside the cell. The goal is to study just the graphite electrode; using lithium metal as a second electrode/reference fulfills all needs. The configuration where lithium metal is used as the second electrode in the cell is commonly called a *half cell*. [76] After the lithium metal electrode is placed in the cell it is sealed using the MTI MSK-110 crimper, shown in Figure 20. The crimping pressure is 50 kg/cm^2 (750 psi). The half-cell cycling and measurements were conducted on an MTI BST8-MA, shown in Figure 22.

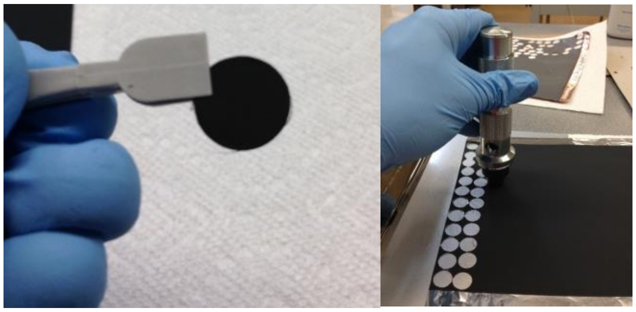

(a) (b)

Figure 19. (a) ½ electrode used in coin cells (b) punching electrode from electrode sheet

(a) (b)

Figure 20. (a) Argon glove box where all cells were fabricated (b) crimper used to seal the half cells.

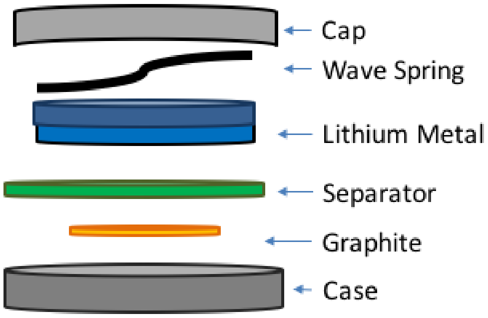

Figure 21. Schematic of the components used in the assembly of the half cells.

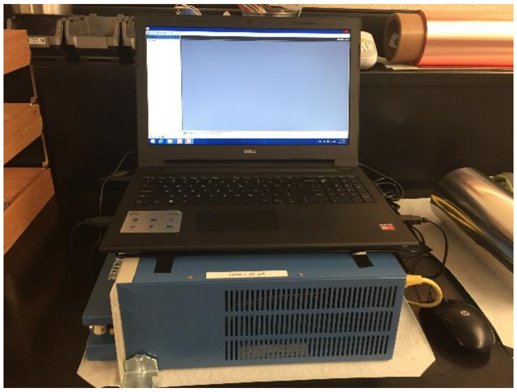

Figure 22. MTI BST8-MA system used in the cycling of the half cells.

Half Cell Operation vs. Full Cell Operation

It is important to understand the fundamental operational differences between a half cell and a normal full cell. The differences can affect charging and discharging procedures due to differences in what is occurring electrochemically inside the cell. Figure 23 (a) depicts the electrode configuration for a typical full cell battery. The higher potential electrode – verse the reference lithium – is $LiCoO_2$ and the lower potential electrode – verse the reference lithium – is graphite. During charging the difference in potential of the two electrodes increases. At the graphite anode, lithium ions are intercalating into the graphite structure. During this intercalation, process is when lithium dendrites form. During discharge the potential difference between the two electrodes decreases. Lithium deintercalates from the anode. Figure 23 (b) depicts the electrode configuration in a half cell. The two electrodes are graphite and lithium metal. Graphite has the higher potential of the two electrodes making it the cathode of the cell. This reverses what occurs at the graphite electrode during charge and discharge. Now during charge lithium is deintercalated from the graphite electrode. The potential difference between the two electrodes increases. During discharge, lithium intercalates into the graphite electrode and the potential difference between the two electrodes (or the potential of the cell) decreases. The graphite is considered full of lithium – 100% SOC— when the cell voltage reaches 0.0 V during discharge.

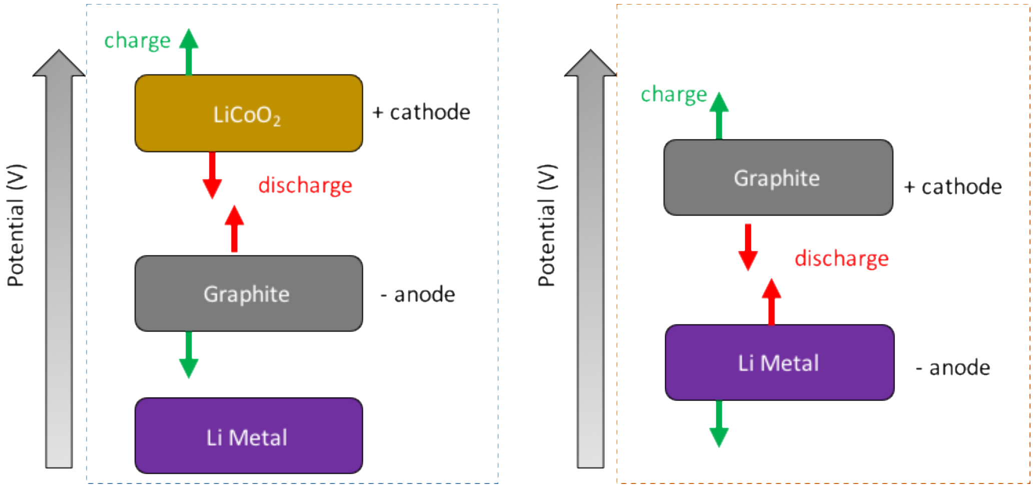

(a) (b)

Figure 23. Depiction of battery cell electrode interaction. (a) Shows the configuration for a typical full cell. (b) Shows the electrode configuration for a half cell. The key difference is the graphite electrode plays an opposite role in the two cells.

Cell Testing

Properties of the graphite electrode can be determined from the Open Circuit Potential (OCP). The OCP is a thermodynamic property. It contains information about the tendency of metallic materials to participate in electrochemical corrosion reactions. [77] At the open circuit potential no current is flowing and the anodic and cathodic reaction rates are in equilibrium. When a current is applied, the cell potential drops below the OCP. When the current is halted, the system will relax back to the OCP. In practice, it is impossible to obtain OCP curves at different SOC's without applying any current; however, if the applied current is small enough the cell's drop below the OCP is minimal and it becomes possible to experimentally obtain the OCP.

The primary challenge in determining the OCP is to use a low enough current to obtain a good approximation, but have that current be high enough so that the test can be finished in a reasonable amount of time. Three very low currents – 100µA, 200µA, 500µA – equivalent to approximately C/30, C/20, and C/10 were picked. Three identical half cells were cycled at one of the three currents. The testing protocol used is shown schematically in Figure 24. Before cycling, the cells were allowed to rest for at least 8 hours. This allows time for the initial reactions between the electrolyte and the electrodes to occur and reach equilibrium. After this initial rest the cell voltage was observed to be between 2.5-3.0V. Next the cells were cycled 5 times. A cycle consists of one discharge (2.5-0.0 V) and one charge (0.0-2.5 V). The first two cycles were deemed the formation cycles. During the formation cycles irreversible electrochemical reactions, such as SEI formation, occur and cycleable lithium is consumed, which results in a loss in capacity. After formation, cycling SEI and other side reactions can continue to occur, but the effects on capacity are minimal and the cell is assumed to be stable. [23] Thus, cycles 3-5 are used for the data analysis and evaluation of the graphite electrode. Three data cycles were used to obtain statistically significant data.

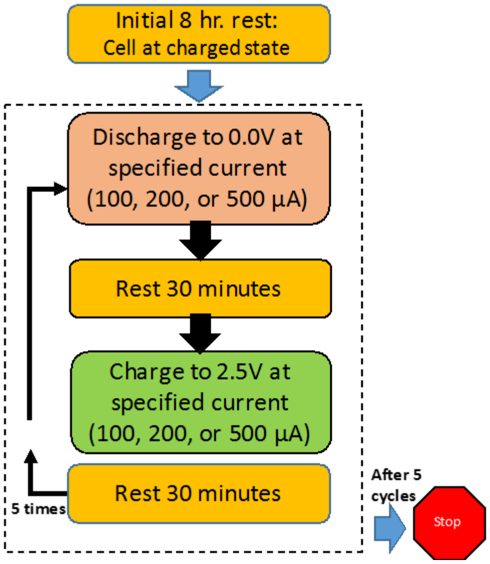

Figure 24. Schematic representing the protocol used to obtain OCP of half cells.

Cell Testing Results

The charge and discharge curves for three separate ½ inch punch graphite half cells are shown in Figure 25. The results show the cell cycled at 200 µA has the highest capacity. This is contrary to the anticipated results; a lower current should result in a higher capacity. As the current is lowered the results should converge give a close approximation for the actual cell capacity, from which the specific capacity can be calculated. The anomaly that the lowest current does not result in the highest capacity is likely related to differences between the cells due to fabrication. These cells are likely not identical even though the same punch size was used. During the punching of the electrode, some of the graphite around the edges of the electrode was noted to flake off. This small amount of missing material is likely the cause of the observed capacity difference.

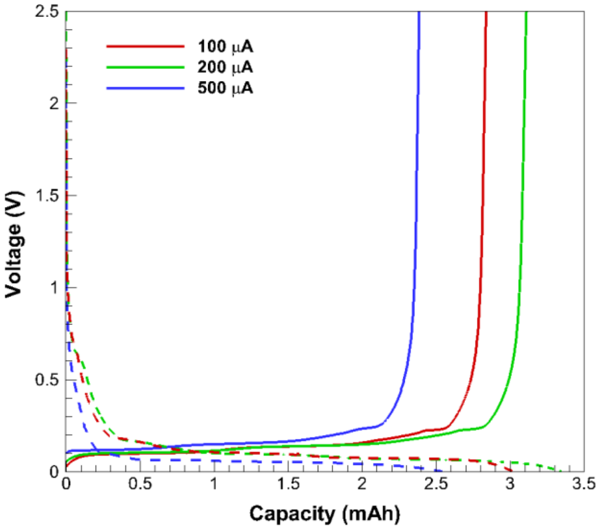

Figure 25. Charge (solid lines) and discharge (dashed) curves for three ½ inch punch graphite half cells at three different currents; all data is from 2nd data cycle for each half cell. Results indicate the cell cycled at 200µA has the highest capacity. This is contrary to anticipated results; lower current should result in the highest capacity. The cause is likely related to differences in the cells due to fabrication. These cells are likely not identical even though the same punch size was used.

The hypothesis that the anomalous results observed in Figure 25 is due to unavoidable discrepancies caused during fabrication was verified by cycling each cell at the same current. At the same cycling current, each cell should have approximately the same capacity. As shown in Figure 26 the variability of capacity across the three different half cells is significant. These cells were all cycled at 200µA. The difference across them is approximately 12%.

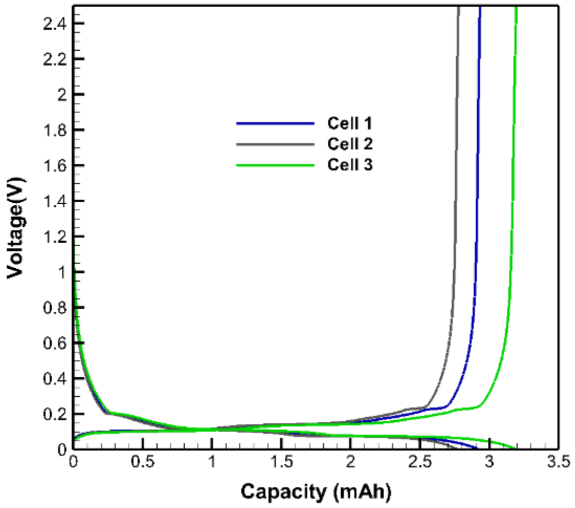

Figure 26. Charge-discharge curves for the three different half cells all cycled at 200 µA. Data shown is from 2nd data cycle for each cell.

To obtain an accurate characterization of the graphite it is necessary to eliminate the effect of unavoidable discrepancies that occur during cell fabrication. Thus, each cell was run at each of the three currents. Within the same cell, an expected trend was observed between the current and capacity as shown in Figure 27. At the two lowest currents – 100 µA and 200 µA—the OCP curves overlap and converge. This curve is taken to be the experimental representation of the OCP because as the current was lowered the same OCP curve was obtained. The capacity obtained by these low current tests is the maximum experimental capacity of the cell.

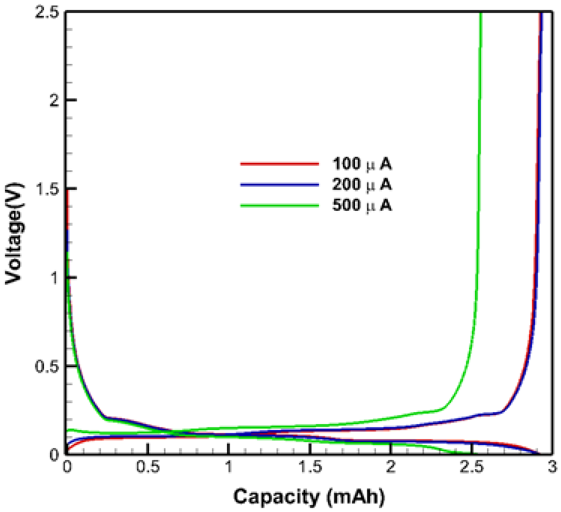

Figure 27. Charge-discharge profiles for the same half cell cycled at all three currents. At the two lowest currents –100μA and 200μA—the curves overlap and converge to a capacity. Data shown is from 2nd data cycle

Table 5, and Table 6. From the experimental data, the specific capacity (mAh/g) was calculated according to Eq. 21. The mass of the active material is determined from Eq. 22. To compare across the different cells, the normalized capacity was calculated according to Eq. 23.

$$C_{sp} = \frac{C_E}{M_{AM}} \qquad \text{Eq. 21}$$

where:

C_{sp} is the specific capacity (mAh/g)
C_E is the experimentally measured capacity (mAh)
M_{AM} is the mass of active material (g)

$$M_{AM} = (M_M - M_{CC}) * \%ActiveMaterial \qquad \text{Eq. 22}$$

where:

M_{AM} is the active material mass (g)
M_M is the measured mass of the punched electrode (g)

M_{CC} is the measured mass of the current collector (copper foil only) (g)

$$C_{Norm} = (C_{cycle}/C_{TheoMass}) \qquad \text{Eq. 23}$$

where:

C_{Norm} is the normalized capacity
C_{cycle} is the experimentally measured capacity (mAh)
$C_{TheoMass}$ is the theoretical capacity based on mass (C_{sp} x M_{AM})

Table 4. Experimentally measured discharge data for each of the three data cycle. The discharge data is normalized by the theoretical capacity by mass

Discharge		Capacity (mAh)			Theoretical capacity (mAh) by mass	Normalized by theoretical capacity by mass		
Half Cell	Current	Cycle 1	Cycle 2	Cycle 3		1	2	3
Cell 1	100 uA	2.917	2.932	2.936	3.088	0.945	0.949	0.951
Cell 1	200uA	2.927	2.930	2.937		0.948	0.949	0.951
Cell 1	500uA	2.640	2.559	2.605		0.855	0.829	0.844
Cell 2	100uA	2.772	2.786	2.772	3.338	0.960	0.956	0.960
Cell 2	200 uA	2.774	2.784	2.789		0.956	0.956	0.960
Cell 2	500uA	2.537	2.564	2.585		0.877	0.875	0.884
Cell 3	100 uA	3.104	3.113	3.137	3.151	0.985	0.988	0.996
Cell 3	200uA	3.080	3.079	3.067		0.977	0.977	0.973
Cell 3	500 uA	2.843	2.808	2.819		0.902	0.891	0.895

Table 5. Experimentally measured charge data for each of the three data cycles. The charge data is normalized by the theoretical capacity by mass.

Charge		Capacity (mAh)			Theoretical capacity (mAh) by mass	Normalized by theoretical capacity by mass		
Half Cell	Current	Cycle 1	Cycle 2	Cycle 3				
Cell 1	100 uA	2.919	2.927	2.922	3.088	0.945	0.948	0.946
Cell 1	200uA	2.933	2.932	2.938		0.950	0.949	0.951
Cell 1	500uA	2.643	2.558	2.607		0.856	0.828	0.844
Cell 2	100 uA	2.798	2.802	2.797	3.338	0.964	0.966	0.964
Cell 2	200 uA	2.778	2.779	2.789		0.958	0.958	0.961
Cell 2	500 uA	2.522	2.555	2.579		0.869	0.881	0.889
Cell 3	100uA	3.097	3.112	3.146	3.151	0.983	0.988	0.998
Cell 3	200uA	3.09	3.087	3.083		0.981	0.980	0.978
Cell 3	500uA	2.843	2.813	2.821		0.902	0.893	0.895

Table 6. Specific capacity during discharge for each half cell and each of the three data cycles. The three data cycles were averaged at each current for each half cell. The 100µA and the 200µA cycles "avg per cell" were averaged to calculate the "average over cells"

Discharge		Specific Capacity (mAh/g)			Avg per cell	Average over cells	Standard Deviation
Half Cell	Current	Cycle 1	Cycle 2	Cycle 3	Specific Capacity (mAh/g)	Specific Capacity (mAh/g)	
Cell 1	100 uA	310.3	311.9	312.3	311.5	317.8	6.1
Cell 1	200uA	311.4	311.7	312.4	311.8		
Cell 1	500uA	280.9	272.2	277.1	276.7		
Cell 2	100uA	315.0	316.6	315.0	315.5		
Cell 2	200 uA	315.2	316.4	316.9	316.2		
Cell 2	500uA	288.3	291.4	293.8	291.1		
Cell 3	100 uA	326.7	327.7	330.2	328.2		
Cell 3	200uA	324.2	324.1	322.8	323.7		
Cell 3	500 uA	299.3	295.6	296.7	297.2		

Table 7. Specific capacity during charge for each half cell and each of the three data cycles. The three data cycles were averaged at each current for each cell to create "avg per cell". The 100µA and the 200µA cycles "avg per cell" were averaged to calculate the "average over cells"

Charge		Specific Capacity (mAh/g)			Avg per cell	Average over cells	Standard Deviation
Half Cell	Current	Cycle 1	Cycle 2	Cycle 3	Specific Capacity (mAh/g)	Specific Capacity (mAh/g)	
Cell 1	100 uA	310.5	311.4	310.9	305.7	317.5	6.3
Cell 1	200uA	312.0	311.9	312.6	312.2		
Cell 1	500uA	281.2	272.1	277.3	276.9		
Cell 2	100uA	318.0	318.4	317.8	318.1		
Cell 2	200 uA	315.7	315.8	316.9	316.1		
Cell 2	500uA	286.6	290.3	293.1	290.0		
Cell 3	100 uA	326.0	327.6	331.2	328.2		
Cell 3	200uA	325.3	324.9	324.5	324.9		
Cell 3	500 uA	299.3	296.1	296.9	297.4		

Summary

Graphite is a common anode material in lithium ion batteries. During discharge, the graphite anode is the initiation site for dendrites due to the closeness of the Li/Li^+ intercalation potential to the deposition potential of metallic lithium. To study the formation of dendrites on graphite electrodes it is first necessary to characterize the graphite under normal operating conditions without dendrites. The characterization of graphite was performed using lithium metal half cells. An experimental procedure and setup was established to fabricate and test these half cells. Issues due to fabrication that would affect the experimental results were discovered and eliminated allowing for the characterization of graphite through obtaining the OCP curve. An experimental specific capacity for the graphite was determined, which as expected is lower than the theoretical specific capacity provided by the manufacturer. The overall experimental specific capacity was found to be 317.5 ± 6.3 mAh/g for the discharge cycles and 317.8 ± 6.1 mAh/g for the charge cycles. These overall experimental specific capacities were found by averaging the specific capacities measured during each of the three data cycles of the 100µA and the 200 µA cycles for each cell. The averages of the three data cycles for each cell were then averaged resulting in the overall experimental specific capacity for this graphite.

CHAPTER IV

CHARACTERIZING DENDRITE GROWTH ON GRAPHITE ELECTRODES UTILIZING ELECTROCHEMICAL IMPEDANCE SPECTROSCOPY

Motivation and Background

Evaluation of dendrites on graphite anodes is difficult because they are often small, occur under only certain charging conditions, and if they are allowed to grow too much they short circuit the cell, which can lead to catastrophic failure and leave nothing to analyze. Throughout the literature, it is possible to find successful evaluations and examinations performed on dendrites related to lithium ion batteries. Common surface techniques like SEM [78, 79], TEM [80, 81], XPS [82, 83], AFM [84], and optical microscopy [85, 86] have been implemented to study dendrite growth. Love et al. studied the growth of dendrites and the influence temperature has on their development. [36] Their study of dendrites utilized an “open face” electrode setup. Each electrode was placed between optically transparent quartz windows. This configuration allowed for the testing of a working battery cell while making it possible to observe the surface of the electrodes during operation. Dolle et al. similarly created a custom cell to study lithium plating utilizing SEM. [79] The vacuum requirements of SEM and the instability of lithium dendrites when exposed to air necessitated the utilization of a custom transfer mechanism that allowed them to test their open face battery and then transfer it into the SEM vacuum chamber for analysis. They were able to make observations of the dendrite morphology as related to applied electrode current density. At lower current densities, the structure was mossy whereas at higher current densities the dendrites had a more needle like structure.

Nishikawa et al. performed in situ observations of dendrite growth utilizing a laser scanning confocal microscope. [86] They evaluated the influence of the concentration of lithium ions in the electrolyte near the substrate with initiation time of the dendrites as influenced by current density. Higher current densities resulted in a lower initiation time and more prolific accumulation of dendrites on the surface of the electrode.

The downside of most of the techniques utilized is they require a special experimental setup and these types of tests cannot be performed on unmodified commercially available cells. In general, all these approaches are also cumbersome, and time consuming. Electrochemical Impedance Spectroscopy (EIS) is an analysis technique, which has the potential to reveal information about the electrochemical processes occurring in a battery cell, without opening the cell. EIS measures the response of an electrochemical system to a small-applied perturbation. The perturbation can be a small potential perturbation (5-10mV), or small current perturbation. [87] The response of the system, as a function of the frequency, can reveal internal information.

In the literature, EIS has been utilized to study the State-of-Health (SOH) and State-of-Charge (SOC) of lithium ion batteries during operation. Love et al. was able to use single-point impedance to obtain SOH information on commercial 18650 type batteries. They were able to correlate changes in the impedance to SOC and identify when cells had experienced cycling abuse and may be compromised. This ability to identify individual cells that may have experienced cycling abuse and may be compromised is particularly important for applications like battery management systems used in electric vehicles. Typical battery packs have a multitude of individual batteries connected together. If a single cell in one of the packs goes bad it may be impossible determine that by just looking at the health of the entire pack, as is commonly done. Rodrigues et al. utilized AC impedance to evaluate SOC of commercially sealed lithium ion batteries.[88] They applied an equivalent circuit model and non-linear least squares fitting to identify and correlate changes in the spectra to changes in internal resistance inside the battery due to SOC. Li et al used impedance spectra to look at commercially available prismatic lithium ion cells as they are repeatedly charged-discharged over many cycles. [89] They correlated changes in the size of the low frequency semi-circles with number of cycles. They noted an increase in the size of the low frequency semicircles due to cycling. This is likely due to the increase in interfacial resistance of both electrodes.

Zhang et al. used EIS to measure the resistance of SEI film after cell fabrication and during initial cycling to study its development. [90] They characterized impedance spectra by the degree of lithiation of the graphite electrode and found the lithiation process takes place in five stages, which is reflected in the impedance spectra. In addition to studying the SEI, EIS has been used to study intercalation kinetics of lithium into a graphite anode [91, 92]. Takami et al. measured changes in the graphite structure using XRD and looked at the impedance profiles. They characterized the impedance profiles as containing two or three semicircles that overlap.[92]

The difficulty in utilizing impedance data, particularly when trying to study dendrite formation, is in interpreting the data. Much discrepancy exists in the literature as to what each semi-circle in the Nyquist plot represents. It is almost impossible to determine which semi-circle in the impedance spectrum corresponds to which electrode (anode or cathode).[93] Both electrodes contribute to the impedance spectrum and both electrode reactions can be of similar magnitude. [88, 94] However, most research has shown the medium-frequency – middle semi-circle – can be attributed to the passive film on the electrodes. [88, 95] The low frequency tail of the impedance spectrum is mostly attributed to diffusion effects through the bulk material. It is often referred to as Warburg impedance. Where the impedance spectrum crosses the real axis is known as the serial resistance, which represents the resistance across the cell. It is the contribution of ohmic resistances from electrolyte and separator. [96] The first, high-frequency, semi-circle, which may or may not be visible is attributed to the SEI formation on the surface of the anode.[96] To gain greater insight and better quantify the semi-circles, equivalent circuits are often utilized for analysis. Most circuits are composed of resistors and capacitors in series and in parallel to represent the capacitive and resistive effects of physical characteristics like the development of films on the electrodes, electrolyte and separator resistance, diffusion, and charge transfer. [88, 90-92, 97] Equivalent circuit workup by Chen et al. substituted capacitors with Constant Phase Elements (CPE). [98] CPE better represent the porosity that is present in electrodes and can better capture attributes of diffusion, ultimately leading to a better fit of the data. In some situations, CPE can be converted to equivalent resistors and capacitors to aid in physical interpretation and analysis of the circuit.

EIS has the potential to reveal information about lithium plating occurring inside a battery. The challenge and the task at hand is to separate out the effects of lithium plating from other processes that may be represented by an EIS spectrum. The objective of this work is to cause metallic lithium to electrodeposit on graphite electrodes in a Li/graphite half cell and verify electrodeposition has occurred using SEM imaging. SEM imaging is a destructive approach because the half cell must be disassembled to image the electrode. Following confirmation that plating is being induced in the half cells the goal is to utilize Electrochemical Impedance Spectroscopy (EIS), a non-destructive approach, to detect and understand the development of lithium plating/dendrite growth on graphite anodes. The goal is to see how the electrodeposition of lithium is reflected in EIS spectra, quantified through equivalent circuit analysis. After an extensive literature review it has been found that no study has been done trying to utilize graphite half cells and electrochemical impedance spectroscopy to specifically study plating on graphite electrodes.

In this study Li/graphite half cells are used. One of the advantages of half cells is they can simply the electrochemical processes occurring inside the cell by using a lithium metal counter electrode. Only the graphite electrode is of interest, so using lithium metal as opposed to another common electrode material simplifies the situation. Additionally, plating only occurs when the potential of the graphite anode drops below 0V vs Li/Li^+. [99] In a half cell this is the measured cell potential, so potential of the graphite electrode can be monitored by just measuring the cell voltage eliminating any need for a third reference electrode.

Electrochemical Impedance Spectroscopy (EIS)

Electrical impedance is analogous to electrical resistance, and can be thought of as resistance with a frequency dependence. Ohm’s law relates voltage, current, and resistance according to Eq. 24.

$$V = \frac{I}{R}$$ Eq. 24

where:
V= voltage (volts)
I= current (amps)
R = resistance (ohms)

Ohm's law provides a very useful relationship between these three electrical properties and is good for an ideal resistor; however, the ideal resistor has three major shortcomings.[87]

1. Assumes this relationship is uniform and true regardless of the current and voltage level
2. Assumes the resistance values are independent of frequency
3. Assumes that the signals for AC current and voltage through a resistor are in phase

In practice, the three assumptions are not always observed to be true. Thus, the introduction of the concept of impedance, or frequency dependent resistance, is necessary. Impedance, like resistance, is a measure of a circuit's resistance to current flow, but impedance is not restricted by the three shortcomings of Ohm's law.

The general principle of EIS is to apply an AC potential, or sinusoidal signal, and measure the characteristic response from the cell, by measuring the current signal.[96] If the response of the cell is linear, or pseudo-linear, then the current signal can be analyzed as a sum of sinusoidal functions. A Fourier Series is the widely utilized mathematical tool to represent a sum of sinusoidal functions.

Implementing Fourier Series analysis requires the system be linear. A linear system is one that can be represented by the superposition of signals—the summation of sinusoidal functions. The responses of electrochemical cells are frequently non-linear as demonstrated in Figure 28. The doubling of the voltage does not necessarily correlate to a doubling of the current. However, if the analysis voltage window is small enough the system exhibits a linear response, as shown in the subset Figure 28. This is referred to as a pseudo-linear system and allows for linear analysis, which is much simpler than non-linear analysis.

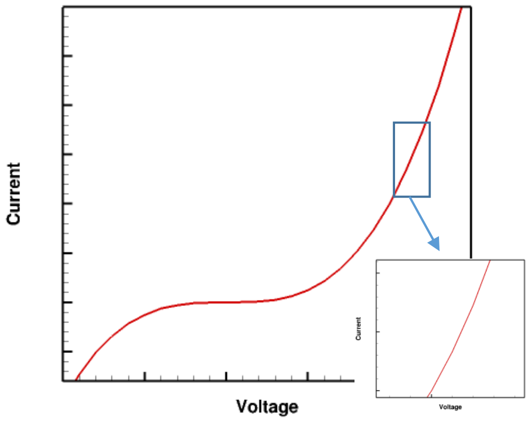

Figure 28. The non-linear relationship that exists in an electrochemical cell between current and voltage. The subset shows that in analyzing a small voltage window the system can be represented as linear, leading to the pseudo-linear classification.

When conducting an impedance measurement there is an applied excitation signal, and a response signal. The applied excitation signal (voltage) can be represented by Eq. 25. The response signal (current) in a linear system will be shifted by phase Φ and have different amplitude. The response signal can be represented by Eq. 26. The input signal and the corresponding response signal shifted by phase Φ are shown in Figure 29.

$$V_t = V_o \sin(\omega t) \qquad \text{Eq. 25}$$

where:

V_t= voltage as a function of time
V_o= initial voltage amplitude
ω= radial frequency
t = time

$$I_t = I_o \sin(\omega t + \Phi) \qquad \text{Eq. 26}$$

where:

I_t= current as a function of time
I_o= initial voltage amplitude
ω= radial frequency
t = time
Φ= phase shift

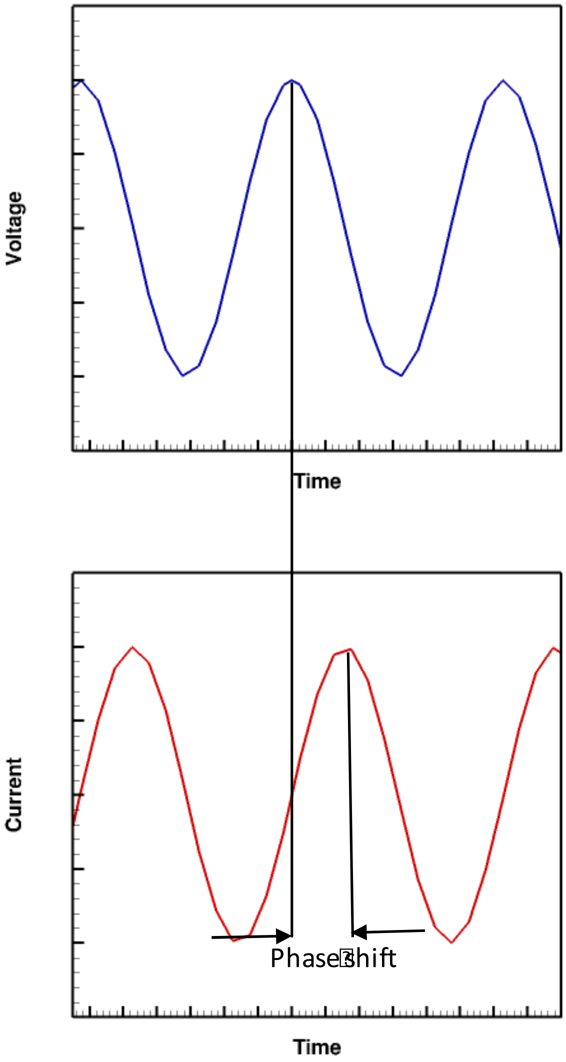

Figure 29. Input and response signal in a linear system. The output signal will be shifted by a phase shift Φ

A representation of impedance that is analogous to Ohm's law is represented in Eq. 27. The impedance is expressed in terms of the magnitude of the impedance (Z_o) and the phase shift(Φ).

$$Z = \frac{V_t}{I_t} = \frac{E_o \sin(\omega t)}{I_o \sin(\omega t + \Phi)} = Z_o \frac{\sin(wt)}{\sin(wt + \Phi)} \qquad \text{Eq. 27}$$

Historically this information was represented as a Lissajous Figure illustrated in Figure 30. All analysis was done by comparing and looking at features on the Lissajous Figure. With the improvement in computational power and the development of the Fast Fourier Transform Method it became easier and more useful to express impedance as a complex function.

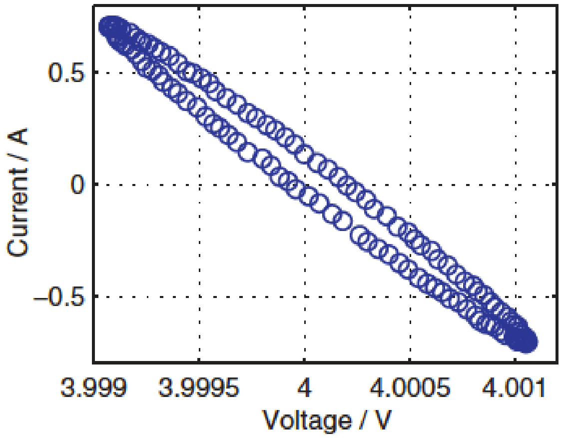

Figure 30. Lissajous figure of lithium ion battery at 100% SOC, 50Hz [96]

The Euler relationship states:

$$\exp(j\Phi) = \cos(\Phi) + j\sin(\Phi) \qquad \text{Eq. 28}$$

Using the Euler relationship, the current response and the voltage response can be rewritten as follows.

$$E_t = E_o \exp(j\omega t)$$

Eq. 29

$$I_t = I_o \exp(j\omega t - \Phi)$$

The impedance response then has a complex representation.

$$\mathrm{Z} = \frac{E_t}{I_t} = Z_o \exp(j\Phi) = Z_o(\cos(\Phi) + jsin(\Phi))$$

Eq. 30

The impedance can now be plotted in terms of the real (Z’) and imaginary parts (Z’’). This type of plot is commonly known as a Nyquist plot. A Nyquist plot makes it easier to visualize the influence of various cell parameters. Nyquist plots are the preferred method for evaluating impedance data; however, they have the disadvantage of not containing any information about the time. This makes it impossible to identify the frequency of a particular point.

Analysis of impedance data is often done by creating equivalent circuits. The impedance can be represented by common electrical elements shown in Table 8. The impedance of a resistor has no imaginary part and is independent of frequency. The current signal through a resistor stays in phase with the voltage signal across the resistor. A capacitor’s impedance is frequency dependent. The impedance decreases as frequency increases. The Nyquist plot representation of a capacitor is a vertical line in the imaginary part (-Im(Z)>0). An inductor has an impedance that is the opposite of a capacitor. Its impedance is again frequency dependent, but the Nyquist representation of an inductor is a vertical straight line in the imaginary negative part (-Im(Z)<0). The constant phase element (CPE) is frequency dependent. The Nyquist representation is a straight line in the imaginary positive part (-Im(Z)>0) with an angle $\propto \pi/2$ with the real axis. The impedance of a CPE decreases with increasing frequency. In the expression of impedance for a CPE $\omega = 2\pi f$, T is a constant, and 0<m<1. When m=1 the CPE becomes a pure capacitor with T as the capacitance. When m=0.5 the CPE represents Warburg impedance. Warburg impedance, or the Warburg element is used to represent semi-infinite linear diffusion. Warburg impedance is an example of a constant phase element where the phase angle is constant at $-\pi/4$ and is independent of frequency.[98, 100]

Table 8. Impedance representation for common electrical components.

Component	**Impedance**
Resistor (R)	Z=R
Capacitor (C)	$Z=\frac{1}{j\omega C}$
Inductor (L)	$Z=j\omega L$
Constant Phase Element (Q)	$Z=1/(i\omega T))^{m}$
Warburg Element (W)	$Z=\frac{\sqrt{2}\sigma}{\sqrt{i2\pi f}}$

Each component listed in Table 8 creates a characteristic shape in the Nyquist plot, which can be used to understand and interpret data. Figure 31 shows the characteristic Nyquist plot for a resistor and capacitor in series. The resistor acts to shifts the plot along the real axis. The capacitor controls the magnitude along the imaginary axis. If the same resistor and capacitor were placed in parallel, the characteristic Nyquist plot takes the shape shown in Figure 32. The Nyquist plot forms a semi-circle with the resistor determining the magnitude along the real axis and the capacitor controlling the amplitude of the semi-circle along the imaginary axis. Figure 33 shows a resistor (R_S) is series with a resistor (R_{CT}) that is parallel with a capacitor (C_{DL}). This setup is referred to as the Randles cell. This is a fundamental configuration often used to represent impedance data for battery cells. R_s represents the “solution” resistance or the resistance across the cell caused by the electrolyte and separator. The solution resistance can be a significant factor in the cell and is dependent upon the ionic concentration. R_{CT} represents the charge transfer resistance, or the polarization resistance present in the cell. Polarizing of the cell occurs whenever the potential of an electrode is forced away from its OCP. Polarization can result in current flow and subsequent reactions at the electrode surface. The capacitor, C_{DL}, which is in parallel with R_{CT} represents the double layer capacitance caused by the electrode and electrolyte interface. This double layer is on the order of angstroms in thickness. Capacitance can range from 20-60µF for every $1cm^2$ of electrode surface area. Factors such as electrode potential, temperature, ionic concentration, and surface roughness all effect the electric double layer.[87]

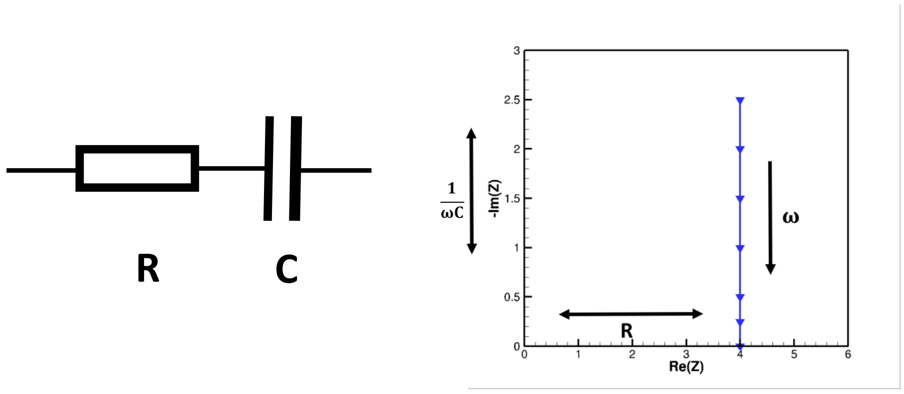

Figure 31. Characteristic Nyquist plot for a resistor in series with a capacitor. The resistor controls the shift along the real axis and the capacitor controls the magnitude along the imaginary axis.

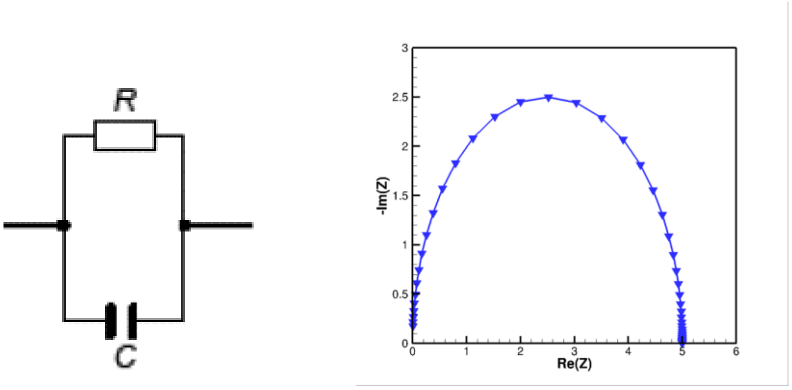

Figure 32. Nyquist plot for a resistor and capacitor in parallel. The resistor controls the magnitude along the real axis and the capacitor controls the amplitude along the imaginary axis.

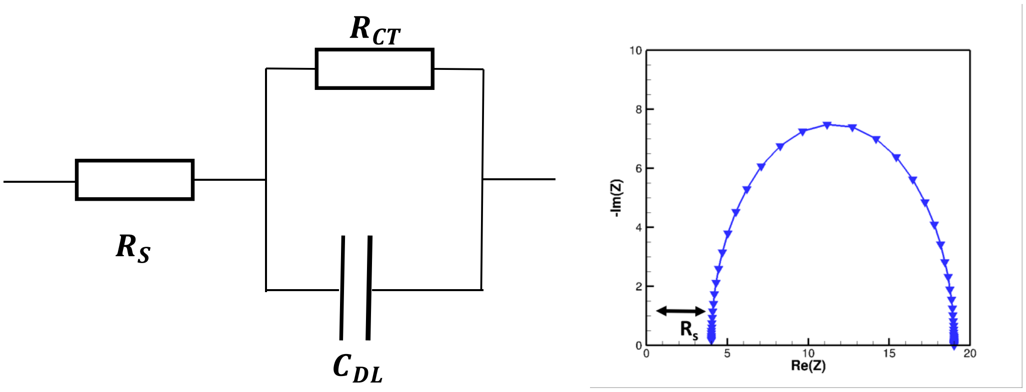

Figure 33. Randles cell configuration. Resistor (R_s) represents the electrolyte and separator resistance. R_{CT} represents the charge transfer resistance. C_{DL} represents the double layer capacitance.

Diffusion related processes have a characteristic shape that appear in Nyquist plots. The associated impedance is referred to as the Warburg Impedance and appears at lower frequencies. As represented in Figure 34 the Warburg impedance appears as a straight line. Typically, the Warburg impedance creates the tail of the impedance spectrum. A typical full impedance spectrum from a Randles cell with Warburg impedance (i.e. diffusion effects) is shown in Figure 34.

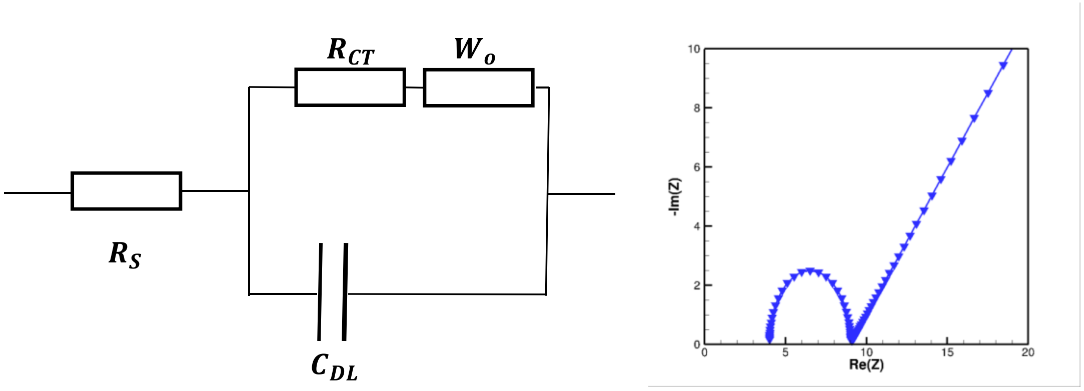

Figure 34. Equivalent circuit representation for Randles cell with Warburg impedance- tail of the spectra.

Due to the complex nature of an actual battery cell, there are a variety of equivalent circuits that can be fitted to a real cell and they can range in complexity. As mentioned, the Randles model shown in Figure 34 is a common starting place. This model has been used to characterize the electrode/electrolyte interface. [101] Takami et al used a Randles model to study the kinetics of lithium intercalation into carbon electrodes. [92] They termed their resistor (R_p) and capacitance (C_p) to represent all the polarizing and capacitive effects that occur inside a cell. However, on a carbon electrode a passivation film that forms primarily on the carbon electrode will typically influence the impedance spectra. This film can show up as a second semi-circle, particularly if the time constants of the processes related to the passivation film are significantly different from other processes occurring inside the cell. Itagaki et al. utilized and equivalent circuit with an additional resistor-capacitor pair to represent the effects of passivating films (SEI). Their measured impedance spectra and equivalent circuit are shown in Figure 35. They have no diffusion tail in their spectra because of the range in which they collected their measurements. Their fit differentiates the influence from the passivation film on the surface, the first semi-circle in the Nyquist plot, from the charge transfer and double layer effects, second semi-circle.

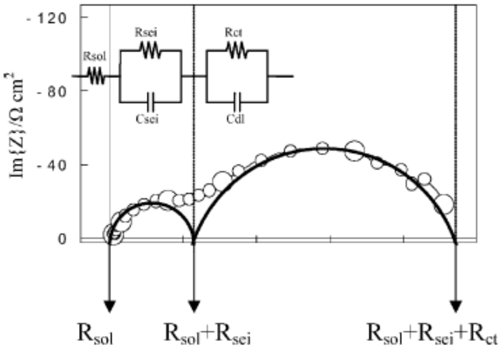

Figure 35. Equivalent circuit fit to impedance data for analyzing graphite electrodes and SEI growth by Itagaki et al. Impedance collected 10mHz-10Mhz[97]

Zhang et al. reported an impedance study where they evaluated the SEI interface on graphite eletrodes using Li/graphite cells. They fit their data with the equivalent circuit illustrated in Figure 36. The first resistor (R_e) represents the separator/electrolyte resistance. The first resistor and capacitor pair, (R_f, C_f) represent the SEI film, and R_{Ct} and C_{dl} represent the charge transfer resistance and the double layer capacitance. The values of each resistive component was evaluated during the first charge and discharge of the cell. They observed R_e to remain constant, R_f decreased with increasing lithiation of the carbon electrode, and R_{ct} was generally lower at higher degrees of lithiation but showed much fluctuation.

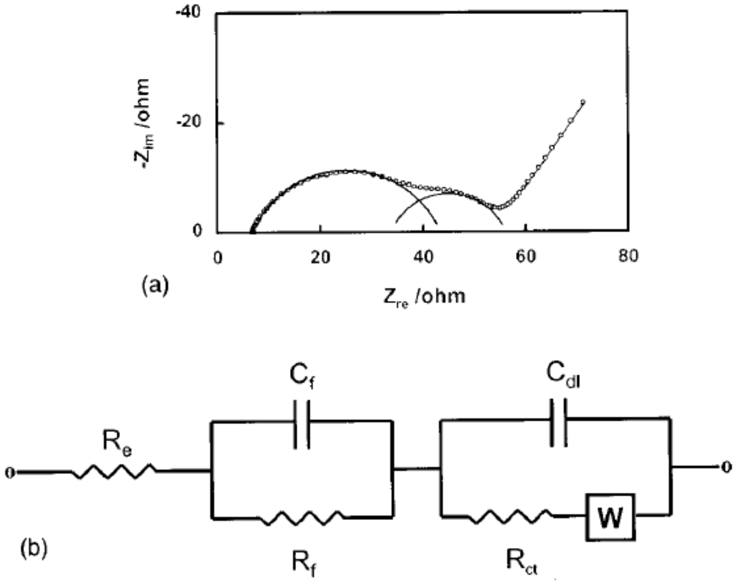

Figure 36. Equivalent circuit and example impedance spectra of Li/graphite cell used by Zhang et al to study SEI formation on graphite half cells. Impedance collected 100kHz-0.01Hz [90]

Chen et al. utilized equivalent circuit analysis with an impedance study on high power lithium ion cells. [98] Rather than using capacitors, they utilized constant phase elements (Q) to better represent the porous nature of electrodes. They found their proposed circuit, Figure 37, adequately fit their experimental data. Utilizing pseudo capacitance, they were able to convert some of the CPEs to capacitors during data analysis as shown in (b). From the magnitude of the capacitance values, they attributed the resistor-capacitor pairs to processes in the cell. R_2Q_2 was attributed to lithium ion transport to the surface because C_2 was on the order of microfarads. R_3Q_3 and R_4Q_4 were both attributed to charge-transfer processed because their capacitors C_3 and C_4 were on the order of millifarads.

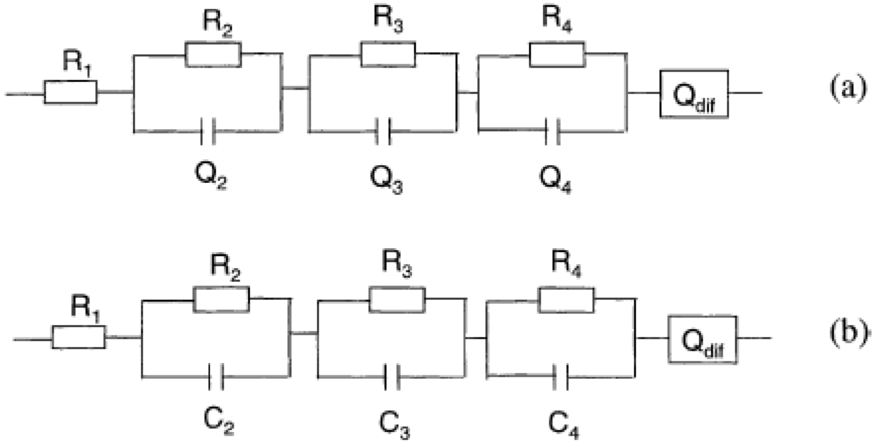

Figure 37. Equivalent circuit proposed by Chen et al. to model a lithium-ion cell using CPEs rather than resistors.[98]

In trying to interpret and understand impedance data, it is important to recognize what to look for and what to expect from an impedance spectrum. J.Y. Song conducted a two and three electrode impedance study on lithium ion batteries. In their work, they present the impedance spectra of a lithium symmetric cell, a graphite symmetric cell, and a lithium graphite half cell measured from 10Hz-50kHz. Their impedance results from a symmetric Li-Li cell are shown in Figure 38 (c). The general profile is a large semi-circle. They attribute the larger semi-circle to the nature of lithium metal and a passivated film that forms on the surface between the lithium metal and electrolyte. The changes in the impedance are a result of letting the symmetric cell sit for a period of time. The increase is attributed to an increase in the film. The C-C symmetric cell is shown in Figure 38 (a). Here the impedance profile is almost a vertical line representing the capacitive nature of graphite electrodes. It is important to note that this line is not due to diffusion as there can be none. Zooming in on the spectra as shown in Figure 38 (b), at very high frequencies there is a small semi-circle forming. This is attributed to the formation of a passivating film forming on the surface of the graphite electrode. When the two electrodes are combined and assembled into a half cell and cycled, the impedance spectra reflect the contribution of each electrode shown in Figure 39. The spectra have a semi-circle followed by a tail. The figures progress from a lithiated state (0.133V) to a delithiated state (1.465V) with respect to the graphite electrode. In this case, the semi-circle is caused from contributions from the lithium metal and the SEI layer on the graphite electrode. However, the lithium metal passivation film should remain relatively constant; changes in the semi-circle are likely an effect of the SEI on the graphite electrode. The tail that can be seen in the spectra in Figure 39 is a consequence of diffusion, not of the capacitive nature of the graphite electrode, as lithium has now intercalated into the graphite structure. This is further supported by the fact that the slope of the tail now represents the traditional 45-degree angle characteristic of Warburg impedance as opposed to the conductive nature of the vertical line seen in Figure 37 (a). As the graphite electrode is delithiated we see the capacitive effect of the graphite electrode and the influence of the lithium electrode dominate.

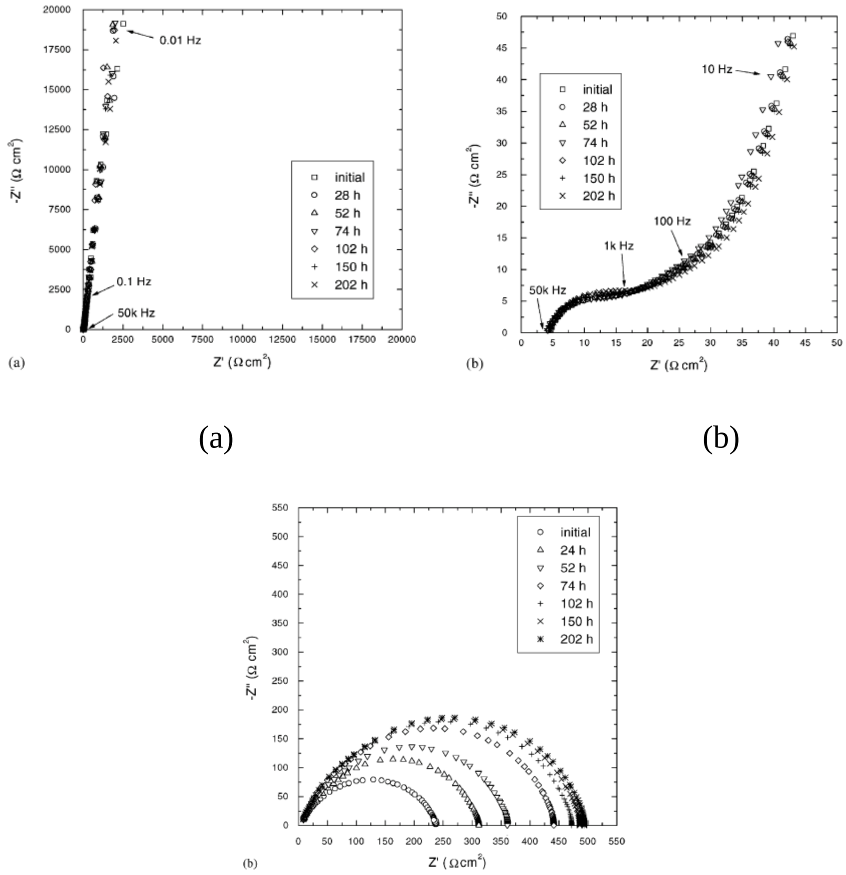

(a) (b)

(c)

Figure 38. (a) Impedance spectra from C-C symmetric cell (b) zoomed impedance spectra of C-C symmetric cell. (c) impedance spectra of Li-Li symmetric cell. All Spectra collected from 10Hz-50kHz [93]

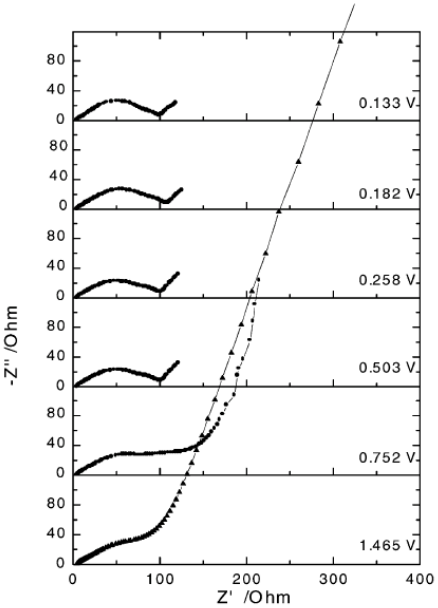

Figure 39. Impedance spectra from Li-C half cell. Starting at a lithiated (0.133V) state and moving to a delithiated state (1.465V). All Spectra collected from 10Hz-50kHz [93]

Methodology

Cell Fabrication

The cells utilized in all experiments were Li/graphite half cells fabricated in house utilizing 2032-coin cell hardware as described in Chapter III. The electrodes used in the cell were punched out of the bulk material using a round ½ punch. The lithium electrode was punched from a 99.9% pure lithium ribbon from Sigma Aldrich. The graphite electrode was punched from an electrode sheet manufactured by MTI Corporation. Single side CSM graphite coated copper foil sheet (241mm L x 200 mm W x 0.1 mm T) 94.5% active material proportion in powder, specific capacity 330mAh/g, active material mass 5.0176 g. The cells were assembled in an argon glove box (ppm < 0.1 H_2O, ppm < 0.1 O_2). The mass of each punched graphite electrode was recorded before assembly in the cell using an OHAUS AX224/E analytical scale, which reports to 0.1 mg with an accuracy of ± 0.2 mg and maximum capacity of 220 g. A BASF manufactured lithium hexafluorophosphate diethylcarbonate electrolyte was used for all cells. A ¾ inch punched 25µm Trilayer polypropylene-polethylene-polypropylene membrane separator manufactured by Celgard was placed between the electrodes to prevent physical contact. The cell was sealed using an MTI-MSK-110 crimper at 50kg/cm^2.

After fabrication, each cell is allowed to rest for at least 8 hours before cycling. The after rest voltage of the cell was found to sit between 2.5-3.0 V. After rest, each cell was CC-cycled (discharge-charge) two times at C/10 (current determined from theoretical capacity). Cells were cycled using MTI BST8-MA battery tester.

Impedance Measurements

Impedance measurements were collected using a BioLogic MPG-2. The potentiostatic measurement protocol was utilized. Spectra was collected in the range 1MHz-10mHz, 10 points per decade, with a single-sinusoidal perturbation of 10mV. Impedance was measured as the cell was cycled through different states-of-charge (SOC). The SOC refers to the lithiation of the graphite: 0% SOC is fully delithiated, 100% SOC is fully lithiated. The process of lithiation occurs during the discharge of a half cell. SOC increases as the cell is discharged; 100% SOC is when the cell potential reaches 0V.

The process of cycling then taking impedance—dynamic impedance probing— at different SOCs is shown schematically in Figure 40. After formation cycling the cell is in a charged state: 0% SOC. At this point an impedance spectrum is collected, then the cell is discharged at C/10 for 1 hour, or by 10% SOC. The cell is allowed to rest for 30 minutes[96] then the impedance spectrum is collected at this new SOC. This process is repeated until the cell is discharged to the desired SOC.

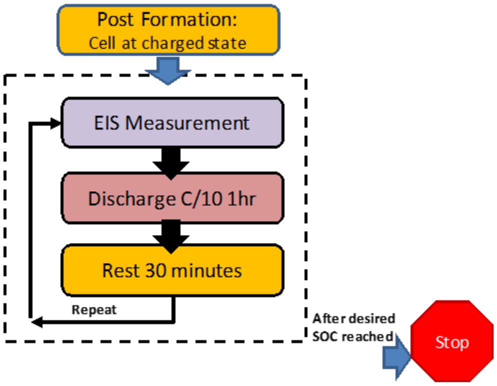

Figure 40. Representation of the dynamic impedance probing protocol used to collect impedance spectra at different SOCs

SEM Imaging

SEM images were collected using a VEGA3 TESCAN, 20 kV beam intensity, tungsten heated cathode. Because lithium metal is highly reactive in atmospheric conditions the cells were disassembled in an argon glove box. A set of needle-nose pliers were used to carefully pry apart the coin cell casing. The tips of the pliers were wrapped with electrical tape to prevent shorting of the cell. Inside the argon glove box the electrodes were rinsed with IPA to preserve any plated lithium [102], mounted with double sided carbon tape to the SEM pucks, and sealed in a plastic bag for transport outside the glove box.

Equivalent Circuit

The equivalent circuit used to analyze the impedance data collected in this work is shown in Figure 41. Similar to the work by Chen et al. this model implements CPEs (Q) to compensate for the porosity and capacitive effects of the electrodes. The first resistor in the model, R_3, represents the serial resistance of the electrolyte and separator. The first CPE-resistor pair (Q_1 R_1) represent the film resistance and capacitance that will form, mostly on the graphite electrode. The next CPE-resistor pair (Q_2 R_2) represent the charge transfer resistance and double layer capacitance. Each CPE is in parallel with a resistor. From this configuration, each CPE can be converted to a capacitor by utilizing the pseudo-capacitance characteristics. The pseudo-capacitance can be calculated for a CPE in an equivalent circuit of the form R1+(R2/Q2). The "+" represents a series relation and the "/" represents a parallel relation. The pseudo-capacitance corresponds to a capacitance value (C) at a frequency (f_o) corresponding to the maximum imaginary part on the Nyquist circle obtained by fitting with the equivalent circuit R1+(R2/Q2). The value is a solution is computed according to Eq. 31.

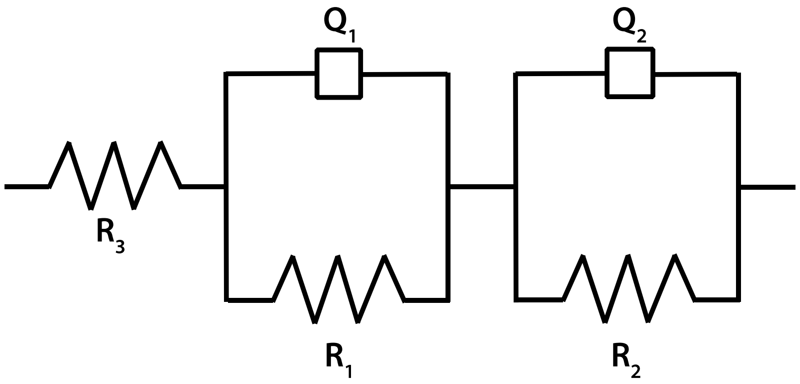

Figure 41. Equivalent circuit developed to analyze the complex impedance plots

$$\frac{1}{2\pi(RQ)^{\frac{1}{\alpha}}} = \frac{1}{2\pi RC} \qquad \text{Eq. 31}$$

where:

α and Q are CPE parameters
R = resistance
C= capacitance

After utilizing the pseudo-capacitance relationship, the equivalent circuit can be represented as shown in Figure 42. The first element in the equivalent circuit is a resistor (R_e). This resistor represents the electrolyte, separator, and other ohmic resistances that exist across the cell between the electrodes. This is in series with C_f and R_f , which represent the passivation film, typically SEI which forms on the graphite electrode. This is followed in series by C_{DL} and R_{CT}, which represent the double layer capacitance and the charge transfer resistance. The electric double layer forms because when a metal electrode is dipped into a solution of its ions, two parallel layers of charge form on both the electrode and the electrolyte sides of the interface. This parallel layer of charge is called the electric double layer (EDL). This double layer causes ions to align at the electrode/electrolyte interface in a manner that can be thought of as a capacitor with the electrolyte acting as a sort of dielectric. Charge transfer resistance is the resistance against the electron transfer from one phase (electrode) to another (electrolyte). For example, in the electrolysis of water energy is required to move electrons from the metal electrode and join them with protons to produce hydrogen. The process of transferring electrons from the electrode to the hydrogen ions in the liquid phase has an associated resistance: the charge transfer resistance. The final element in the equivalent circuit is a Warburg element, which is a

CPE with a constant phase angle and no frequency dependence. The Warburg element is used to represent the semi-infinite diffusion effects present in the cell, particularly visible in the low frequency portion of the spectrum.

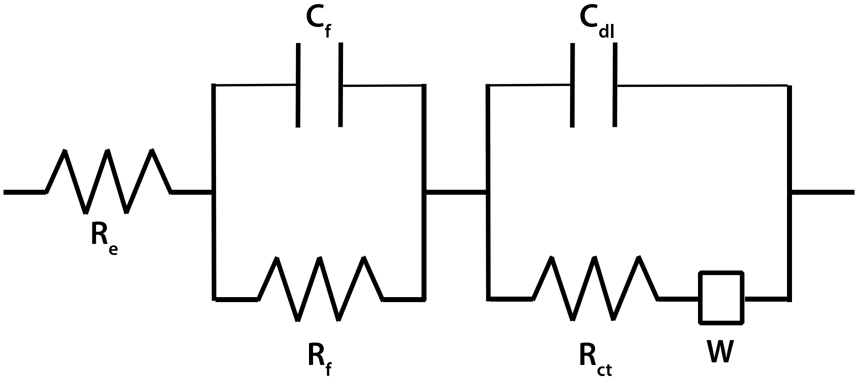

Figure 42. Equivalent circuit where CPEs have been converted to equivalent capacitors through pseudo-capacitance relationship. R_e represents the electrolyte and separator resistance, C_f and R_f represent the film resistance and capacitance, C_{dl} and R_{ct} represent the electric double layer capacitance and charge transfer resistance, W represent the Warburg element.

The various effects (SEI, CT, diffusion, etc) are typically presented in different parts of the spectrum, however if their time constants are close together they will interfere with each other and their corresponding semi-circles on the Nyquist plot will overlap. This is shown in Figure 43 which show a measured impedance spectrum and how the elements of the equivalent circuit will individually be fit and combined to represent the experimentally acquired impedance spectra for the Li/C half cells.

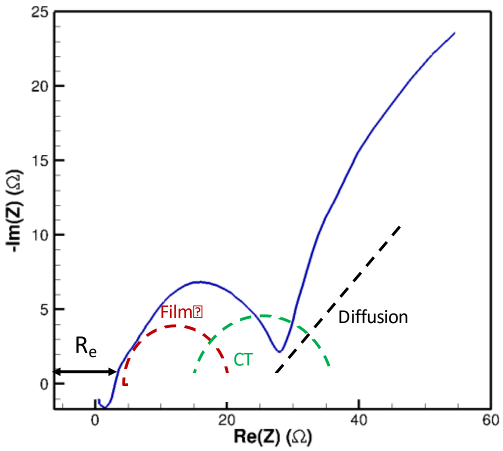

Figure 43. Experimentally measured impedance spectrum (blue line) and circuit elements that combine to reflect the entire spectrum.

Correlation Extraction

The equivalent circuit shown in Figure 41 was fit to the experimental data using EC-Lab® Express Software V5.53 provided by BioLogic Science Instruments. EC-Lab® Express provides a tool called *ZFit*, which allows you to create equivalent circuits with common circuit elements, and provides a fitting method to fit your data. The method used was the Simplex method, which is a non-linear least squares fitting method. Simplex fits the best response in a multidimensional space where variables may be interrelated. The method is computationally slow, however it is quick and easy to implement. The basic idea is one changes a variable, notes the response and tries again. A simplex is a geometric figure with n+1 vertices in n-dimensional space. The method uses three vertices at a time. It picks the two vertices and adjust the system. Because the initial conditions the system starts at have a large influence on the fit, the EC-lab fitting method also includes a randomize method to shuffle all the variables at the beginning of the fit and help more quickly and accurately narrow in on a solution.

The *Z Fit* parameter window is shown in Figure 44 (a). The highlighted in blue is the drop down menu showing the circuit being fit to the experimental data. Z fit provides hundreds of common equivalent circuits that can be used to fit data or it allows you to create your own. It follows the convention where “+” represents a series relationship and “/” represents a parallel relationship. Highlighted in green are the individual parameters and values corresponding to the fit. The user can select which values to use in the simplex method, their range, etc. Highlighted in yellow is the fitting criteria. The fitting method is selected along with how many iterations are used in the fit. The weight option has either 1 or |Z|. This weights the points when fitting. When “1” is selected each point is weighted equally, when |Z| is selected each point is weighted based upon the magnitude of the impedance. In this work “1” was used in all fits. Highlighted in orange at the bottom of the *Z fit* control window are options to save and copy the output from the fit. The *PseudoC* opens a new dialogue box shown in Figure 44 (b). Pseudo C calculates the equivalent circuit using pseudo capacitance as represented in Eq. 31.

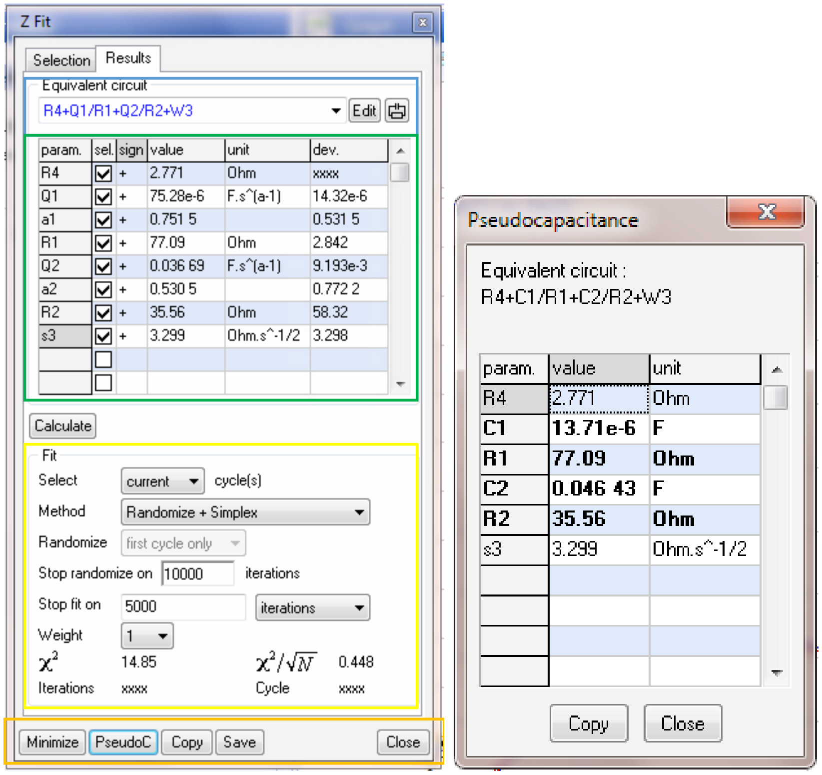

Equivalent circuit
R4+Q1/R1+Q2/R2+W3

param.	sel.	sign	value	unit	dev.
R4	☑	+	2.771	Ohm	xxxx
Q1	☑	+	75.28e-6	F.s^(a-1)	14.32e-6
a1	☑	+	0.751 5		0.531 5
R1	☑	+	77.09	Ohm	2.842
Q2	☑	+	0.036 69	F.s^(a-1)	9.193e-3
a2	☑	+	0.530 5		0.772 2
R2	☑	+	35.56	Ohm	58.32
s3	☑	+	3.299	Ohm.s^-1/2	3.298
	☐				
	☐				

Fit
Select current cycle(s)
Method Randomize + Simplex
Randomize first cycle only
Stop randomize on 10000 iterations
Stop fit on 5000 iterations
Weight 1
χ^2 14.85
$\chi^2/\sqrt{N}$ 0.448
Iterations xxxx
Cycle xxxx

Equivalent circuit :
R4+C1/R1+C2/R2+W3

param.	value	unit
R4	2.771	Ohm
C1	**13.71e-6**	**F**
R1	**77.09**	**Ohm**
C2	**0.046 43**	**F**
R2	**35.56**	**Ohm**
s3	3.299	Ohm.s^-1/2

(a) (b)

Figure 44. (a) Z Fit dialogue window (b) dialogue window from using PseudoC command

Results

SEM Results

To induce plating in a Li/graphite half cell requires the cell reach negative voltages. [76, 99] This can be accomplished in a variety of ways: charging at very high rates, charging at low temperatures, or high SOC. In this work high SOC reached at a low rate (C/10) was used to induce plating because 1) it assures the graphite electrode reaches a fully lithiated state, thus when the voltage does drop below zero it is likely that little or no more lithium intercalation is occurring. More likely, lithium is being electrodeposited on the surface 2) the lower charge rate assures that the deposition of metallic lithium is the cause of the low cell voltage. At higher rates many other factors, like charge transfer, come into play and can cause the potential of the cell to appear to drop below zero when the actual potential of the electrode is not that low. This would be evident when the current is released and the cell potential jumps back to OCV. This phenomenon was observed in 1C discharge tests.

Four electrodes were charged to different SOC's: 0%, 50%, 100%, 120%. Pictures of the electrodes from inside the glove box are shown in Figure 45. All electrodes were rinsed with IPA. The 0% SOC and 50% SOC electrode generally have the black graphite appearance. The 100% SOC electrode appears gold. This is due to the intercalated lithium changing the optical properties of the graphite and is an expected result.[103] The 120% SOC electrode also shows the gold color, however the surface also appears to be partly covered with a silver material, likely electrodeposited lithium. This can be seen before IPA rinsing. After rinsing, the lithium turns a white color and becomes more obvious. The purpose of the IPA rinse is to form Li_2CO_3 which forms from a reaction with the metallic lithium and better preserves the deposited lithium on the surface for evaluation.[102] Figure 46 shows the discharge curve for the 120% SOC electrode and the approximate markings along the curve for the other electrodes. From the zoomed portion of the curve, it becomes clear that the cell voltage does indeed drop below zero volts. In addition, after the current is stopped (rest) the cell voltage does not jump up above zero volts as happens with all other cells.

0%SOC IPA rinsed

50%SOC IPA rinsed

100%SOC IPA rinsed

120%SOC No IPA

120%SOC After IPA rinsed

Figure 45. Images of four electrodes at four different SOCs for SEM imaging

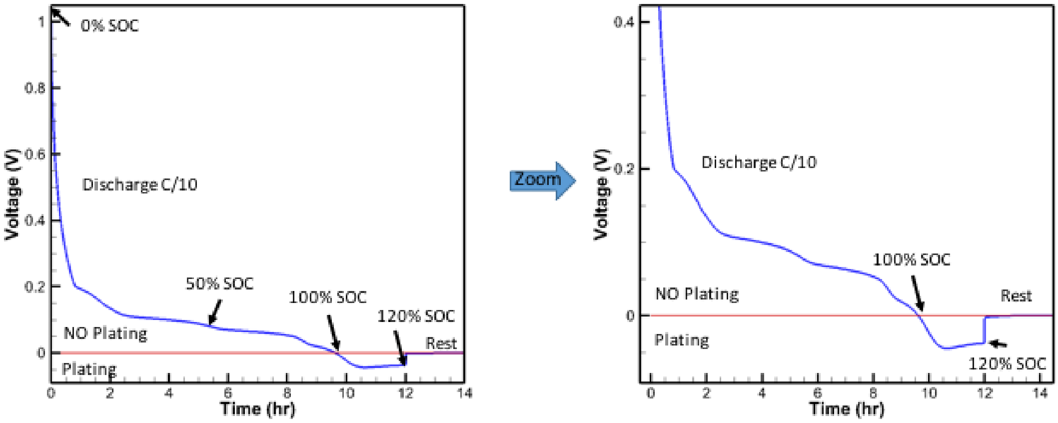

(a)

(b)

Figure 46. (a) Discharge curve through 120%SOC marked with each SOC (b) zoomed view of the discharge curve around 0V showing the drop in cell voltage below 0V allowing for plating of lithium on the graphite electrode.

The SEM images of each electrode are shown in Figure 47 and Figure 48. The 0%, 50%, and 100% SOC images clearly show the graphite particles. The 0% SOC assumes there is virtually no lithium in the graphite structure. The 50% SOC implies about half the available interstitial sites have lithium in them forming LiC_6. The 100%SOC state assumes virtually all the interstitial sites for lithium ions to intercalate are filled. The electrode voltage at this state did not drop below zero volts. At 120% SOC the cell voltage did drop below 0V and the electrode is assumed to be full of lithium. Now the graphite particles are covered with electrodeposited lithium. All images were captured with the same beam intensity and the magnification of the images are denoted in labels.

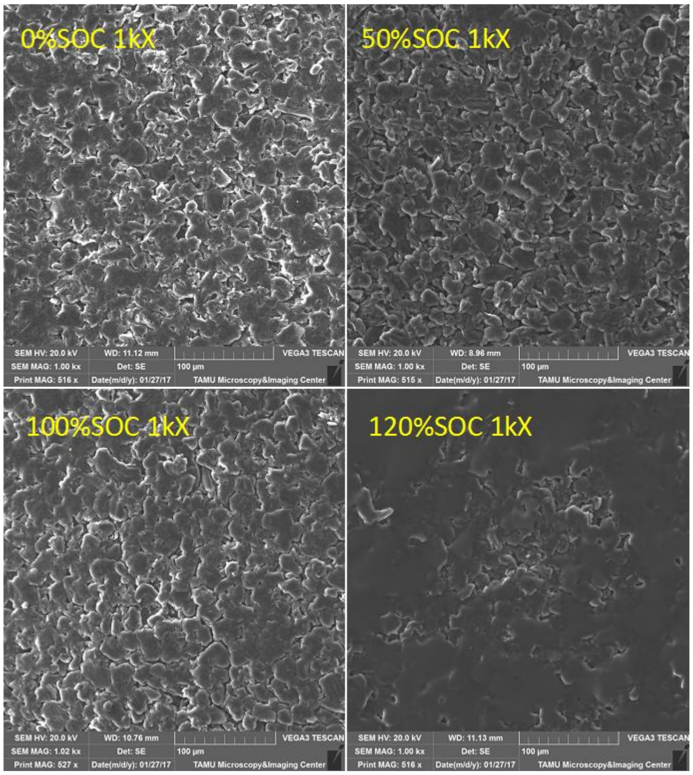

Figure 47. SEM images of graphite electrode at different SOC's. The 0% SOC, 50% SOC, and 100% SOC all show graphite particles. The 120% SOC images shows graphite particles but there also appears to be a covering over a large portion of the electrode: electrodeposited lithium. All images taken at the same beam intensity (20.0kV) and 1kx magnification.

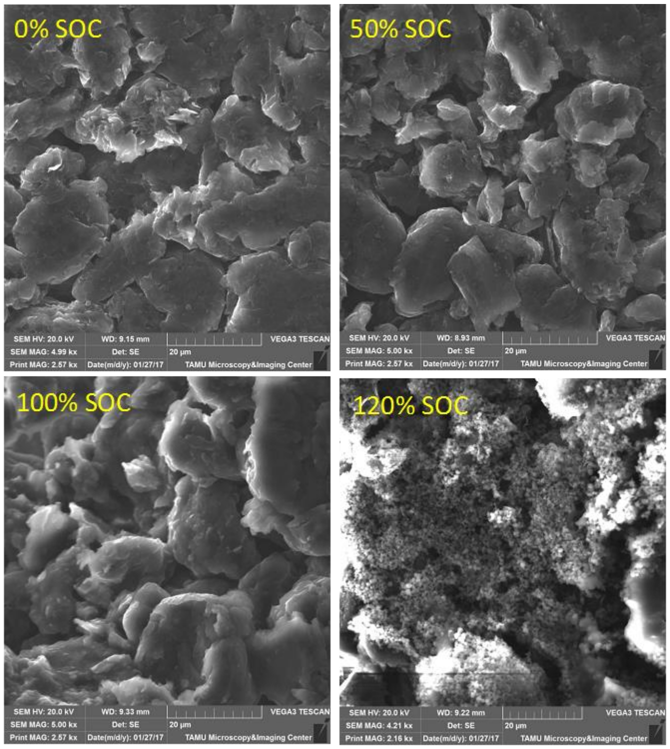

Figure 48. SEM images of graphite electrode at different SOCs. The 0% SOC, 50% SOC, and 100% SOC all show only the graphite particles. The 120%SOC image shows the graphite particles covered with another material, plated lithium. All images taken at the same beam intensity (20.0kV) and magnification 5kx.

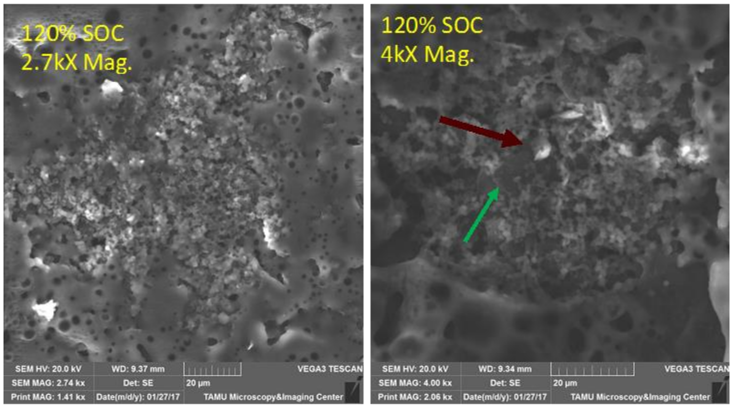

Figure 49. SEM images of different parts of the electrode charged to 120%SOC. The green arrow in the right picture indicates it is possible to see an underlying graphite particle like seen in the other 5kX images. The graphite is covered with lithium dendrites, one of which appears to be protruding up as indicated by the red arrow.

Impedance Results

The dynamic impedance protocol, described in Figure 40, is used to measure the impedance response of several cells. Figure 51 shows the impedance response cycled at C/10 from 0-100% SOC with the impedance measured every 10% SOC. They cell was cycled three times. Figure 50 shows the discharges and the points where the impedance was taken. At low SOC, approximately 10%-80% the impedance remained relatively the same. From 90-100% SOC the impedance increased. With increasing cycles, the impedance at the highest SOC (90-100%) also increased.

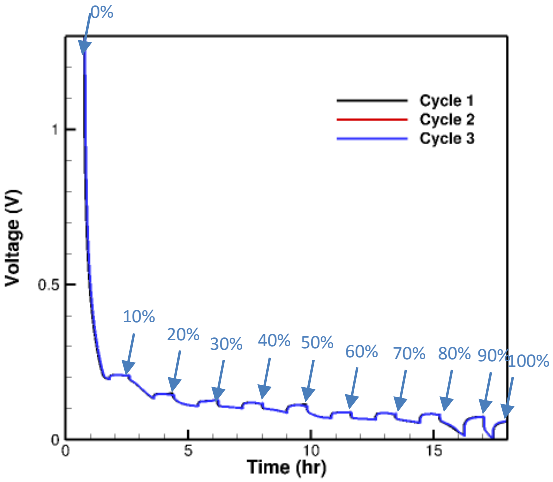

Figure 50. Discharge curve of a cell cycled three times at C/10. Impedance was taken every 10% SOC as denoted by the labels on the graph

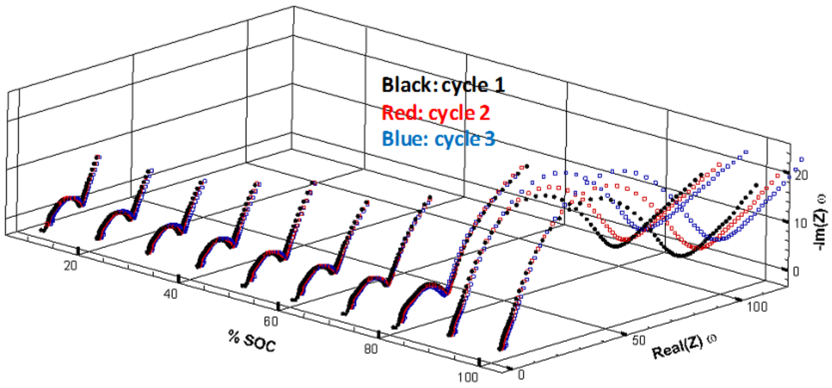

Figure 51. Impedance at different SOC (10%-100%) over three discharge cycles.

The equivalent circuit fit to the impedance data is shown in Figure 52. The equivalent circuit element corresponding to each particular graph is highlighted in blue. The separator/electrolyte resistance remains constant across different SOC. Both the film resistance (R_f) and charge transfer resistance (R_{CT}) show an increase in resistance at high SOC.

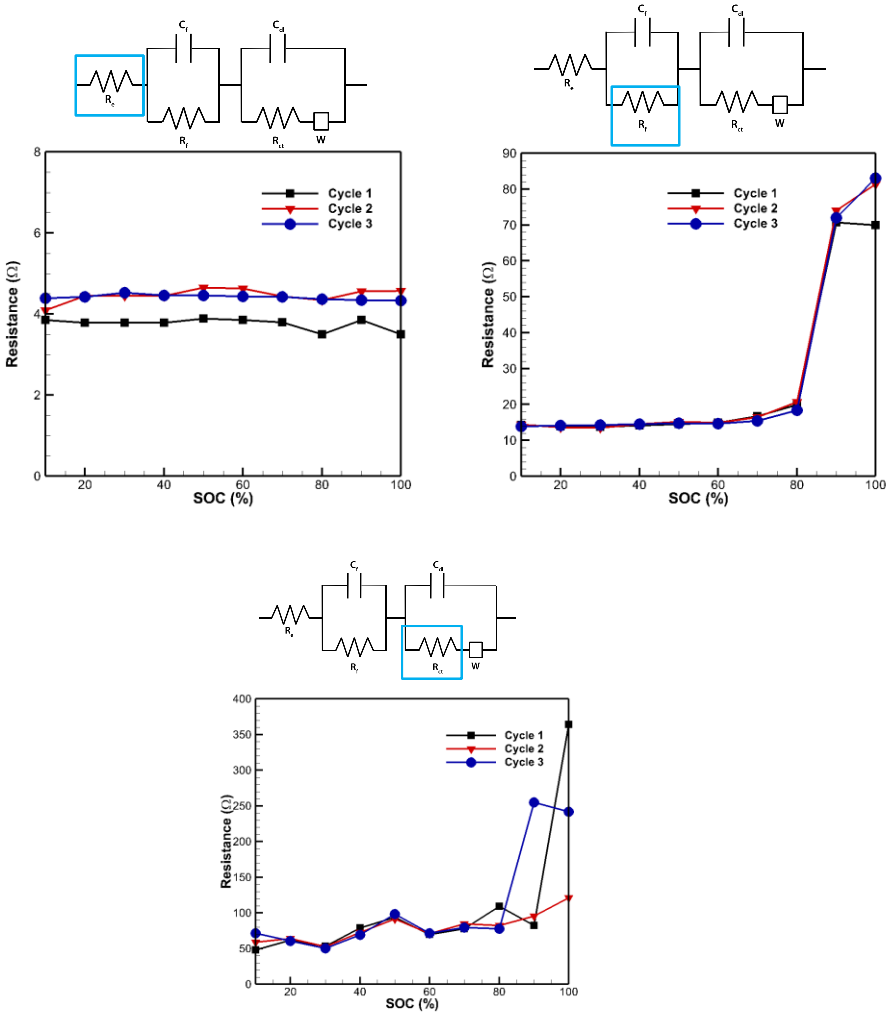

Figure 52. Equivalent circuit resistive elements fit to C/10 impedance data. Equivalent circuit above each graph highlights which element is represented.

With a baseline behavior established, a new cell was cycled at C/10. However, the SOC range is 0-150% SOC. The objective is to investigate the impedance response in a cell where lithium electrodeposition will occur. The impedance was again taken every 10% SOC. The discharge curve is shown in Figure 53. Each 10% discharge is followed by a 30 minute rest (plateaus in the graph) at the end of which the impedance was measured. From 0-100% SOC the cell voltage remained above 0V; thus no plating occurred. From 100%-110% SOC the cell voltage dropps below 0V. After the 110% discharge the cell voltage only relaxed to 0V and did not relax to a positive voltage as happened for 0-100%.

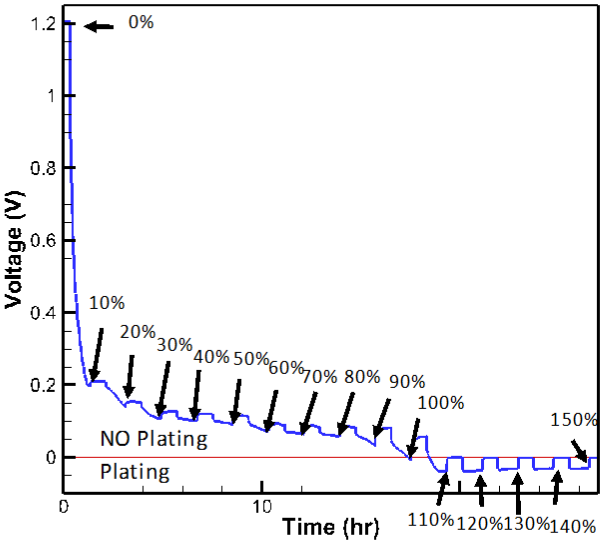

Figure 53. Discharge curve at C/10 with impedance measured every 10%SOC. Each discharge is followed by a 30-minute rest (plateau in voltage) at the end of which the impedance was measured. Above 100%SOC the cell voltage stayed above 0V. After 100% SOC the cell voltage dropped below zero during charging and relaxed to approximately 0V after the current was released (rest).

The impedance measured every 10%SOC is shown in Figure 54. The results shown in the Figure 54 are for two different half cells run under the same operating conditions. Repeat experiments had to be done using a fresh cell because once plating is induced in the cell it cannot be removed. The trends observed between the two cells are similar. Cell 1 is shown in blue circles, Cell 2 orange triangles. At low SOC – 0-60% SOC—the measured impedance remains relatively constant. The size of the semi-circle and the tail do not change appreciably. From 70-100% SOC the diameter of the semi-circle increases dramatically. The maximum size of the semi-circle occurs at 100% SOC and from 110-150% SOC the semi-circle decreases. This trend is more easily observed in the 2D plot shown in Figure 55. For clarity only selective impedance spectra a shown. The 70-100% SOC spectra semi-circle (shown as blue squares) increases sequentially up to 100% SOC. The higher SOC spectra – 120% 130% 150% (chosen for clarity in the graph, the 110% and 140% SOC follow the trend) have semi-circles that decrease in magnitude.

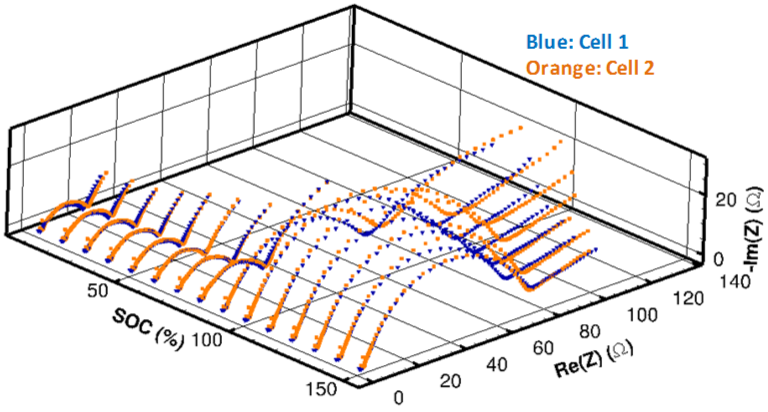

Figure 54. Plot of all impedance spectra measured from 10%-150% SOC. Cell 1 shown in blue circles, cell 2 shown in orange triangles. Similar trend observed between the two half cells.

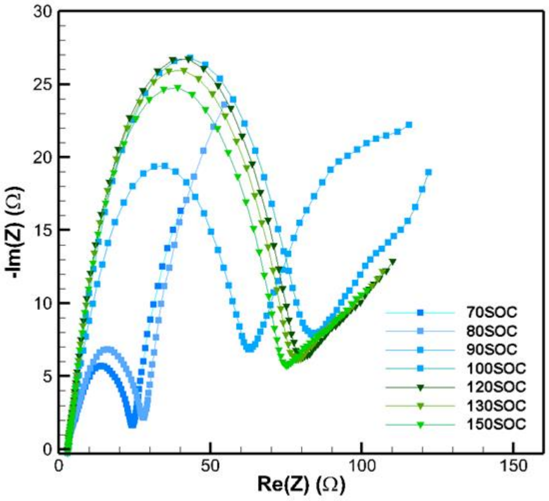

Figure 55. Selective impedance spectra shown from Cell 1 for 70-150% SOC. As SOC increases to 100% SOC –shown in the spectra represented by blue squares— the magnitude of the semi-circle increases. From 110-150% SOC – represented as green triangles— the magnitude of the semi-circle decreases. Omitted SOC spectra follow this trend and were left off for clarity in the graph.

The equivalent circuit previously discussed and shown in Figure 41 is fit to all the impedance spectra. An example fit is shown in Figure 56. In this example the measured impedance spectra, purple triangles, for 80% SOC is fit with the model, shown as blue line. The fit matches the data very well with an R^2 value of 0.995. Similar R^2 values are found for all other SOC fits.

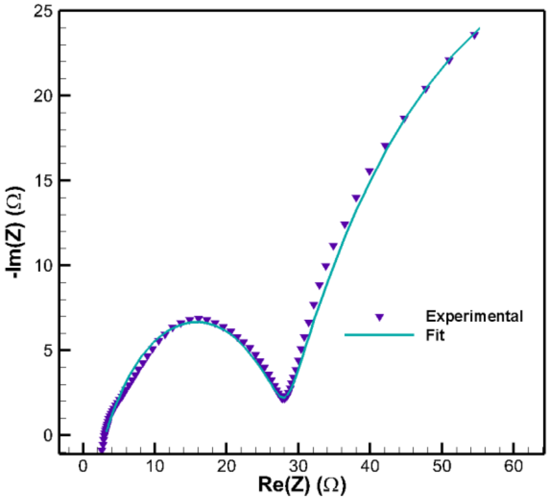

Figure 56. Example of an experimentally measured impedance spectra, purple triangles, fit with equivalent circuit model, blue line. $R^2 = 0.995$ Similar R^2 are found for all other SOC fits.

The results from each of the elements of the equivalent circuit presented in Figure 42 is shown in the following three figures. The first element, R_e, which represents the electrolyte and separator resistance is shown in Figure 57. The resistance value remains constant across all SOCs. This is in agreement with previously reported results by Chen et al. and Zhang et al. [90, 98]

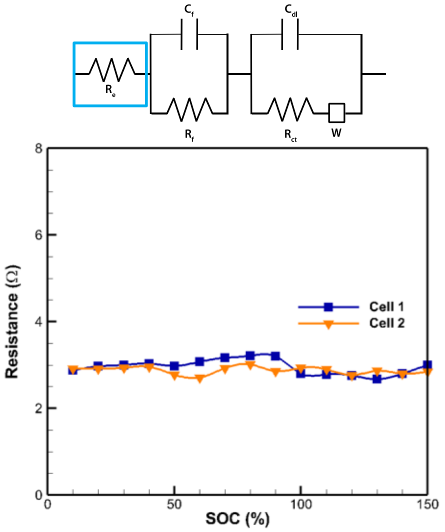

Figure 57. Resistance value for electrolyte and separator resistance, R_e which remains constant across all SOCs.

The resistance element values for R_{ct} and R_f, are shown in Figure 58 and Figure 59. The assignment of which resistor-capacitor pair corresponded to which physical phenomenon was determined by correlation with capacitance. One capacitor always returned values on the order of μF and the other on the order of F. Physically this smaller capacitance value logically correlates to the film capacitance and is the right order of magnitude. The larger capacitance value logically correlates to the double layer capacitance, which one would expect to be much larger. Thus, the resistor paired with C_f is R_f and the resistor paired with C_{dl} must be R_{ct}. The film resistance and capacitance values over all SOCs is shown in Figure 58 and Figure 59. The resistance and capacitance trends are equal but opposite. The film resistance is relatively constant from 10%-80% SOC. The value dramatically increases from 80-100% SOC where it peaks and remains at a relatively constant, or slightly decreasing value. The film capacitance initially starts at a higher value, and is reasonably constant for 10-50% SOC. From 60-100% SOC the capacitance dramatically decreases where it reaches a lower value and remains relatively constant from 110-150%SOC. The same trend is observed across both cells: Cell 1 is shown with blue squares, and Cell 2 is shown in orange triangles.

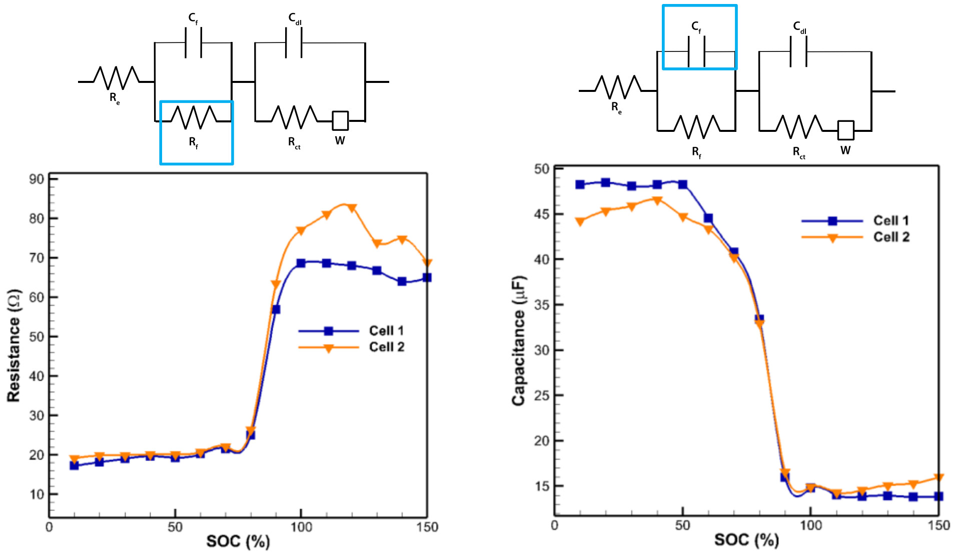

(a) (b)

Figure 58. Resistance R_f (a) and capacitance C_f (b) values for film equivalent circuit elements.

The results for the charge transfer resistance, R_{ct} and double layer capacitance, C_{dl} are shown in Figure 59. The trends present in both the resistance and capacitance follow a similar trend. The charge transfer resistance remains relatively constant from 10-70% SOC. From 80-100% SOC the charge transfer resistance increases dramatically, to a peak value at 100% SOC. As the SOC is increased, 110-150% SOC the charge transfer resistance proceeds to decrease in value. This phenomenon is observed in both cells: Cell 1 represented by blue squares, and Cell 2 represented by orange triangles. The double layer capacitance, C_{dl}, shows a decreasing trend from 10% SOC to 90% SOC. From 90-100% SOC the capacitance drastically increases and then proceeds again to decrease.

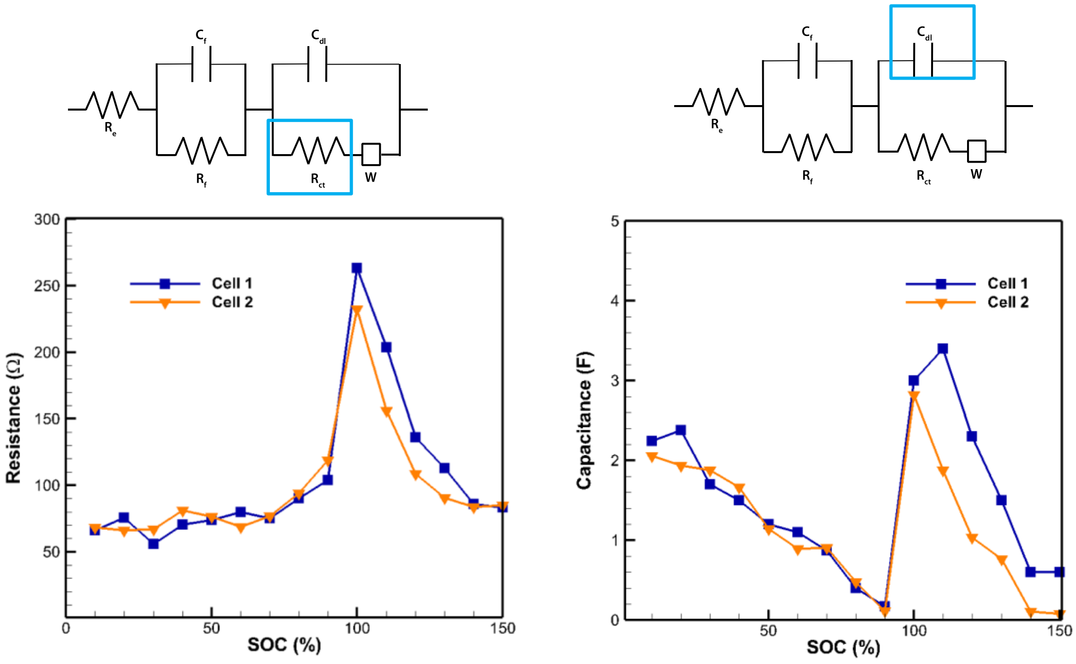

(a) (b)

Figure 59. Resistance (a) and capacitance (b) for charge transfer, R_{ct}, and double layer, C_{dl}, circuit elements.

The dynamic impedance protocol is repeated on a new cell but at a rate of 1C rather than C/10. The impedance is still taken every 10% SOC as shown in Figure 60. The low SOC impedance remains relatively constant, but there is now significant variance between cycles, and the cycle two impedance decreased at high SOC (90-100% SOC) rather than increased with cycles as was observed in the C/10 tests. This trend is shown more clearly in Figure 62. A comparison of the Cycle 1 and Cycle 2 profiles shows that in Cycle 2 the impedance at equivalent SOC was lower. From the discharge curve of the 1C test shown in Figure 61. It is evident that the higher charge rated caused the cell voltage to drop below 0V, and this occurred early in the charge process, around 30% SOC. The equivalent circuit is fit to the 1C impedance data. The resistance element values are shown in Figure 63. The trends in the data are similar to those observed in the C/10 data. The notable difference is that Cycle 2 is lower in resistance than Cycle 1.

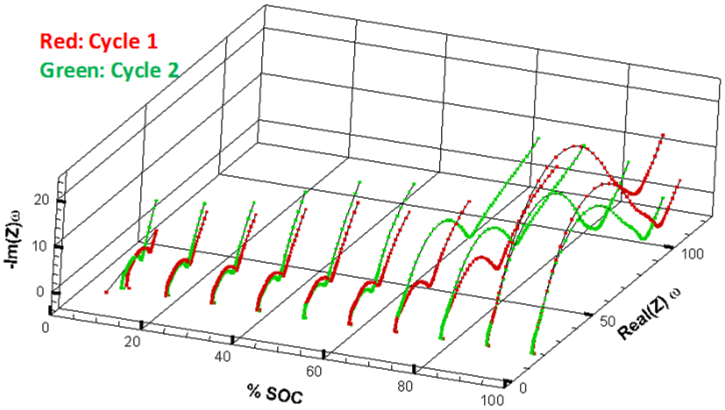

Figure 60. Impedance response at different SOC for a cell cycled two times at 1C.

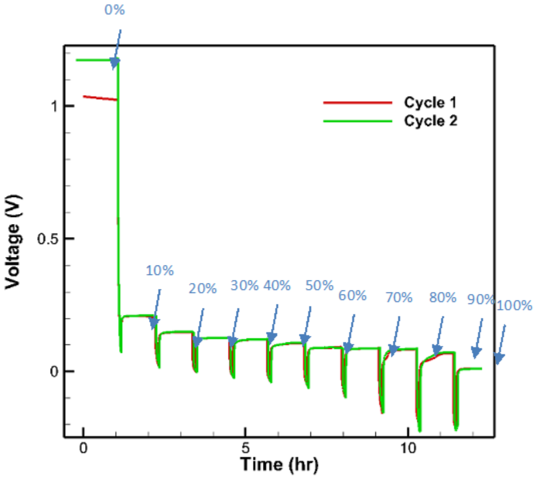

Figure 61. Discharge curve for cell cycled at 1C

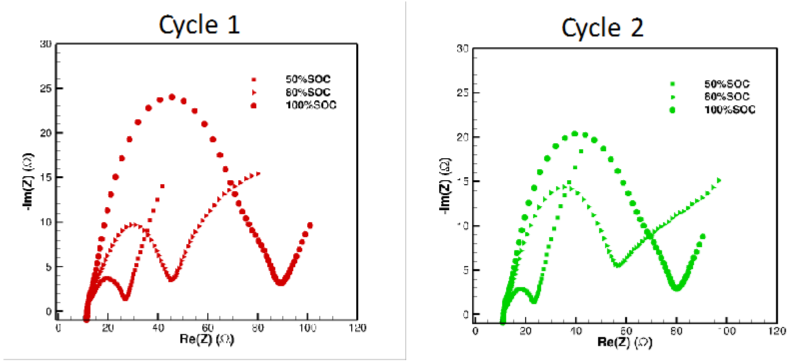

Figure 62. Selective high SOC impedance for cell cycled at 1C. During the second cycle the impedance was generally of lesser magnitude than during the first cycle. This is opposite the trend observed in the C/10 data. The difference is due to the charge C-rate this cell went to negative voltages.

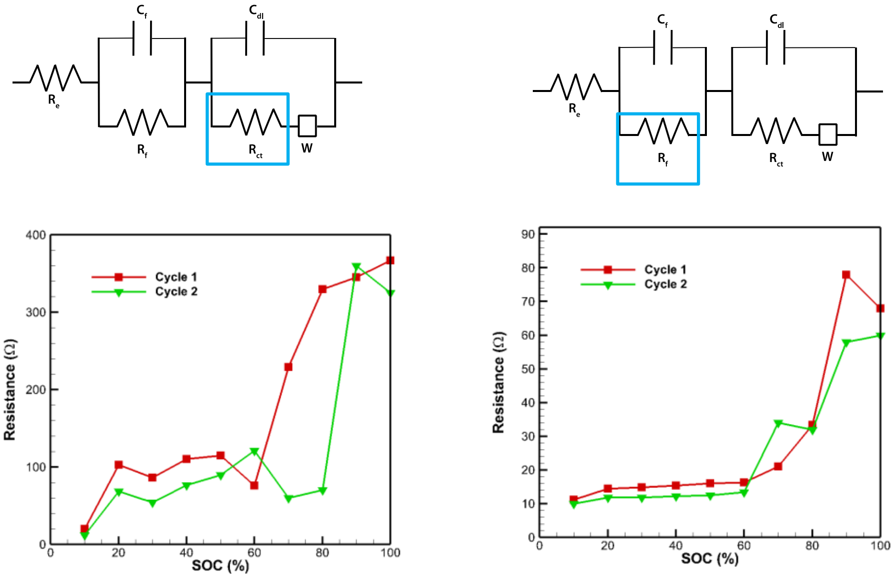

Figure 63. Equivalent circuit resistive elements fit to 1C data. Charge transfer (left) and film (right)

In addition to rate of charge, long term cycling is also evaluated. Two cells are cycled at C/3. One cell is prevented from going to negative voltage by stopping the cell at 0V. The other cell is allowed to go to negative voltage, but not excessively. This cell was stopped at -0.025V. This discharge difference is illustrated graphically in Figure 64. Just a minor difference in voltages is used because it was not desirable to have the difference in voltage windows be a significant factor in capacity. As shown in Figure 65, which plots the normalized discharge capacity versus cycle, the cell that goes to negative voltage shows a larger capacity loss than the cell that is prevented from going to negative voltages. Between the two cells, the trends in the impedance data are also different over cycling, shown in Figure 66. Each impedance spectra was taken after they cycle number indicated and while the cell was in a discharged state (graphite is fully lithiated). The cell cycled only in positive voltage shows with increasing cycles the impedance generally increases. The cell that goes to negative voltages during cycling shows an opposite trend. As cycling increases, the impedance decreases. This decreasing impedance trend follows the trends observed in other situations where electrodeposition is occurring.

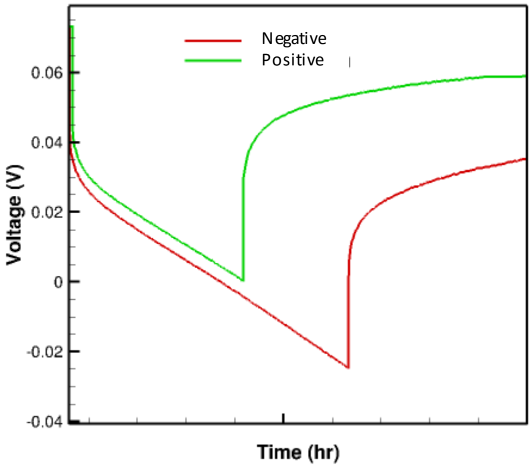

Figure 64. Discharge curve for two difference cells cycled at C/3 indicating that on cell was kept in positive voltages, the other cell was allowed to drop to -0.025V while cycling.

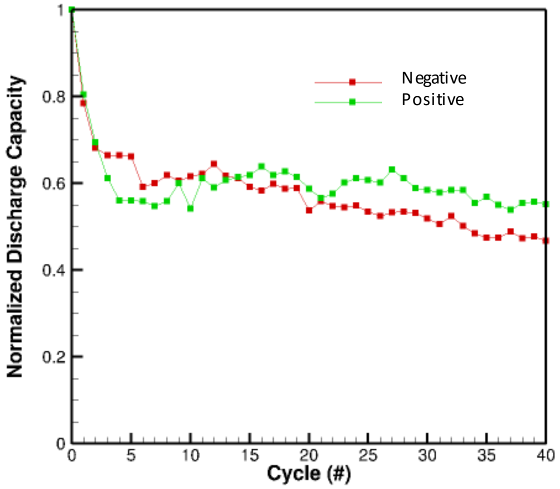

Figure 65. Capacity fade for two cells cycled at C/3.

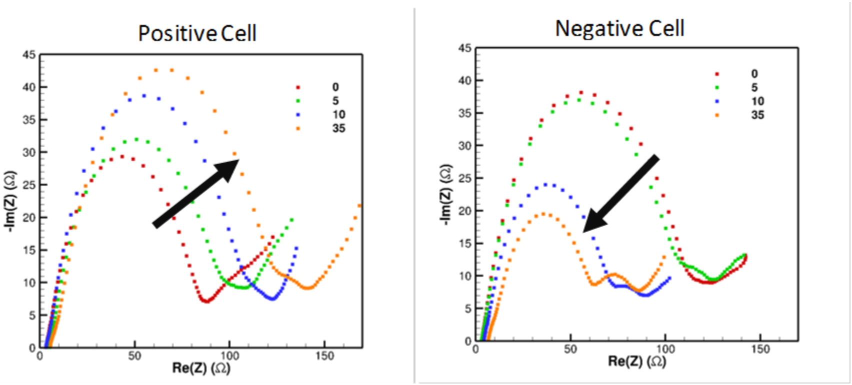

Figure 66. Impedance spectra for the cell that was kept at positive voltage and for the cell that was allowed to go to negative voltages (-0.025V). Both cells cycled at C/3, impedance trends after 0, 5, 10, and 35 cycles are shown and trends are indicated with arrows.

Discussion

In the first SEM image, shown in Figure 47, the 0% SOC image shows the graphite particles are clearly defined and the sharpness of the edges is easily noted. As the images progress too higher SOC (50-100%) the particle shape changes. Clusters appear to push together, and in certain areas the sharpness that the edges of the particles had is gone and they appear more round and smooth. This same phenomenon is seen in the 5kx images shown in Figure 48. The electrode filling with lithium causes this apparent smoothing. In the 120% SOC image, shown in Figure 47, the graphite particles are largely non-discernable and appear to be covered with something that is not present in the other three images: this covering is electrodeposited lithium. The evidence that this covering, which is not present at other SOC, is confirmed to be electrodeposited lithium by Figure 48 and Figure 49. In the 4kx figure it is possible see the graphite particles, as indicated by the green arrow. However, the surface is covered by electrodeposited lithium, forming dendritic like structures, some of them needle-like as indicated by the red arrow.

The behavior of the voltage in Figure 46 is indicative that lithium electrodeposition has occurred. After the discharge to 120% SOC and metallic lithium is deposited on the surface of the electrode, and the potential of the cell when the current is released-- marked *rest*-- remains around 0V. This behavior is also observable in Figure 53. It is due to the presence of electrodeposited lithium. Because there is lithium on both electrodes, there is no longer a potential difference between the two electrodes, like exists when lithium properly intercalates into the electrode and does not deposit on the surface. The negative voltage that the cell reaches plateaus around 40 mV for the C/10 charging rate. This is due to the lower driving force provided by this lower current. At higher currents, like 1C, Figure 61, the cell reaches much lower voltages. Both situations favor the electrodeposition of lithium. It is likely at a more negative voltage and at a higher charging rate increase the rate of deposition.

The dynamic impedance measurements shown in Figure 51 show that the general trend is the impedance remains relatively constant until approaching high SOC. At high SOC the electrodes it is close too full, so there is an increased resistance to accepting more lithium. At low-mid SOC there are many interstitial sites for the lithium to intercalate to, and thus no reason for the resistance to dramatically increase. As the final 20% of charge tries to pass into the electrode it is expected that there would be a rise in resistance as there are fewer open spots for the lithium in the graphite structure. The equivalent circuit resistance elements R_{ct} and R_f demonstrate this in Figure 52. R_e remains constant across all SOC because the bulk composition of the electrolyte and separator does not appreciable change with SOC.

As shown in Figure 54 once the graphite electrode is mostly full and electrodeposition begins, the impedance drops. This makes sense for two reasons. First, metallic lithium is highly conductive and has a very low resistance. Secondly, the lithium is deposited on the surface of the electrode, so the lithium no longer has to intercalate into the electrode, reducing resistance. This trend is clearly illustrated in Figure 59, which shows the response of the equivalent circuit element labeled as the charge transfer resistance (R_{ct}) versus SOC. The film resistance element (R_f) shows a different trend, Figure 58. At low SOC (10-70% SOC) the film resistance remains relatively constant. From 90-100% SOC the resistance jumps. At high SOC the lithium faces an increased resistance to intercalating into the electrode. Some of this lithium starts reacting with the existing film, thus increasing its resistance. The film resistance remains high as electrodeposition occurs because the electrodeposited lithium is going to break up sections of the film and add surface to increase the film. The separator/electrolyte resistance element (R_e) remains constant across SOC, Figure 57. This is expected because the bulk composition of the electrolyte should no change appreciably with varying SOC. The electrolyte acts to connect the two electrodes and transport ions. This constant behavior has also been observed in other work.[90]

At 1C the behavior of the cell indicates plating. As the graphite electrode reaches 30% SOC and above the cell voltage drops below zero as shown in Figure 61. This drop below zero, which allows electrodeposition to occur, is reflected in the impedance behavior. The 1C impedance follows the behavior of the C/10 impedance when plating is present; that is the impedance trend (between cycles) decreases; this is shown in Figure 62.

The long-term C/3 capacity fade data shown in Figure 65 shows the cell that goes to negative voltages experiences more capacity fade over many cycles than the cell that remains at positive voltages. This is due to the loss of cyclable lithium because electrodeposition is occurring in the cell that goes to negative voltages. It is worth noting that originally, for the first 10 cycles, the cell that stays above zero volts shows a larger loss in capacity. This is likely because the cell going to negative voltage has a larger voltage window, so experimentally more charge is passed into the cell making it appear to have a larger capacity. But over cycling as the effects of electrodeposition increase and more lithium is deposited on the surface of the graphite electrode, it’s observed that indeed the cell that is going to negative voltage has a larger capacity loss, due to electrodeposition. The impedance data further supports this analysis. The positive cell, which always stays above 0V (i.e. will not have lithium plating), shows a trend in the impedance data where more cycling leads to an increase in the impedance. This is attributed to an increase in the SEI and degradation of the electrode with cycling. These same phenomena are present in the cell that goes to negative voltage. In addition, electrodeposition is also occurring, because the impedance data trend decreases, Figure 66. As discussed earlier, this is due to lithium metal being highly conductive and depositing directly on the surface of the electrode, leading to a decrease in the impedance.

Conclusion

The objective of the work of this chapter was to investigate electrodeposition of metallic lithium on graphite electrodes by probing the cell at different SOC. The probing consisted of looking at the potential data and impedance response of the cell. A procedure of dynamically taking impedance at different SOC is created. Different trends in the impedance data are found, certain aspects of the trends, such as the decrease in impedance, were a result of electrodeposition of lithium on the surface of the electrode. Electrodeposition is verified using SEM imaging. Imaging showed when the cell voltage dropped below zero electrodeposition could occur and lithium dendrites are observed on the graphite. No electrodeposition is observed on cells that remained above 0V. From probing at high charge rates and over repeated cycling, the same trends established in the C/10 probing regarding plating are observed. Overall, it is shown that electrochemical impedance spectroscopy is a powerful tool in understanding electrodeposition on graphite electrodes. EIS coupled with the application of equivalent circuit analysis detects deposited lithium on graphite in a manner that is non-destructive to the battery. Further testing under a wider range of conditions such as C-rate, temperature, and refining the SOC window are the natural next steps.

CHAPTER V

CONCLUSIONS AND FUTURE RECOMMENDATIONS

The overall objective of this work was to investigate and increase the understanding of the electrodeposition of lithium (dendrite growth) on graphite electrodes. This task is approached using two major tools: modeling and experimentation. From the modeling approach a fundamental understanding in model development, design, verification, and validation was established. Based upon previous work in the literature a basic needle-like dendrite model is coded in Python. The model code and numerical techniques are verified using the method of manufactured solutions. After verification, the model is validated by comparing the results with previously reported experimental data. Under the same conditions as the experimental data, the model is found to be in agreement with the experimental data.

This model, of course, has limited applicability, and future expansion and evolution could include adding terms to account for dendrite tip morphology, relaxing the single-needle like assumption, expanding into further dimensions, and integrating into a multi-electrode, full scale, model through the utilization of other available codes like CAEBAT.

The second tool, experimentation, makes up the second part of this work and aims to investigate the electrodeposition of metallic lithium on graphite electrodes. The experimental work includes several parts. The first part required coming up with the appropriate experimental procedure: cell fabrication, characterization of the materials used, and development of testing protocols. In particular, the novel dynamic impedance probing protocol developed and utilized to study the impedance response of the experimental cells at different SOC. From the impedance response information it is possible to determine how the cell responds during normal charging conditions and under conditions in which lithium electrodeposition is occurring. Analysis of the impedance data and the implementation of tools like equivalent circuit analysis lead to the observation of trends in the data that make it possible to detect plating across conditions of high SOC, high charge rate, and repeated cycling.

Future expansion of the work could naturally move to expanding the application of the dynamic probing protocol. More analysis at different C-rates and at a more refined and focused SOC interval can help further understand the development of plating. This can then be expanded to different temperature ranges, as all this work was conducted at room temperature.

Overall, the objectives of this work were accomplished. While of course many questions remain to be answered this work uniquely touched upon and added for the author and the scientific community a broad range of tools and applications to aid in answering the scientific and engineering problems that exist now, and will exist in the future.

REFERENCES

[1] History.com Staff. (2010, December 01, 2016). *Hoover Dam*. Available: http://www.history.com/topics/hoover-dam

[2] G. Job and F. Herrmann, "Chemical potential—a quantity in search of recognition," *European Journal of Physics,* vol. 27, p. 353, 2006.

[3] U. EIA, "Annual energy review," *Energy Information Administration, US Department of Energy: Washington, DC www. eia. doe. gov/emeu/aer,* 2011.

[4] G. Cravens, *Power to save the world: The truth about nuclear energy*: Vintage, 2010.

[5] Independence Hall Association in Philadelphia. (2008, December 1, 2016). *America in the Second World War: The Decision to Drop the Bomb*. Available: http://www.ushistory.org/us/51g.asp

[6] X. Luo, J. Wang, M. Dooner, and J. Clarke, "Overview of current development in electrical energy storage technologies and the application potential in power system operation," *Applied Energy,* vol. 137, pp. 511-536, 2015.

[7] R. Huggins, *Advanced batteries: materials science aspects*: Springer Science & Business Media, 2008.

[8] U. o. C. Davis. (2013, December 01). *Batteries: Electricity through chemical reactions*. Available: http://chem.libretexts.org/Core/Analytical_Chemistry/Electrochemistry/Case_Studies/Batteries%3A_Electricity_though_chemical_reactions

[9] J. Qian, W. A. Henderson, W. Xu, P. Bhattacharya, M. Engelhard, O. Borodin, *et al.*, "High rate and stable cycling of lithium metal anode," *Nature Communications,* vol. 6, 2015.

[10] J. Wandt, C. Marino, H. A. Gasteiger, P. Jakes, R.-A. Eichel, and J. Granwehr, "Operando electron paramagnetic resonance spectroscopy–formation of mossy lithium on lithium anodes during charge–discharge cycling," *Energy & Environmental Science,* vol. 8, pp. 1358-1367, 2015.

[11] Clean Energy Institute. (December 01). *Lithium Ion Battery*. Available: http://www.cei.washington.edu/education/science-of-solar/battery-technology/

[12] The Ohio State University. (2014, December 7). *First-Ever Look Inside a Working Lithium-Ion Battery*. Available: https://engineering.osu.edu/news/2014/09/first-ever-look-inside-working-lithium-ion-battery

[13] Graphene-info. (2016). *Graphene batteries: Introduction and Market News*. Available: http://www.graphene-info.com/graphene-batteries

[14] Servo Vision. (2016, December 7). *Long Lifespan and Ultra Safe Rechargeable Cell*. Available: http://www.servovision.com/LifePo4%20Pouch%20Cell/LifePo4%20Pouch%20Cell.html

[15] D. Anderson. (2010, December 7). *Lowering costs of lithium-ion battereis for EV power trains*. Available: http://sustainablemfr.com/energy-efficiency/lowering-costs-lithium-ion-batteries-ev-power-trains

[16] D. Aurbach, Y. Talyosef, B. Markovsky, E. Markevich, E. Zinigrad, L. Asraf, *et al.*, "Design of electrolyte solutions for Li and Li-ion batteries: a review," *Electrochimica Acta,* vol. 50, pp. 247-254, 2004.

[17] K. Guerin, A. Fevrier-Bouvier, S. Flandrois, M. Couzi, B. Simon, and P. Biensan, "Effect of graphite crystal structure on lithium electrochemical intercalation," *Journal of the Electrochemical Society,* vol. 146, pp. 3660-3665, 1999.

[18] R. Dominko, M. Bele, M. Gaberšček, A. Meden, M. Remškar, and J. Jamnik, "Structure and electrochemical performance of Li 2 MnSiO 4 and Li 2 FeSiO 4 as potential Li-battery cathode materials," *Electrochemistry Communications,* vol. 8, pp. 217-222, 2006.

[19] S.-T. Myung, Y. Hitoshi, and Y.-K. Sun, "Electrochemical behavior and passivation of current collectors in lithium-ion batteries," *Journal of Materials Chemistry,* vol. 21, pp. 9891-9911, 2011.

[20] C. D. Rahn and C.-Y. Wang, *Battery systems engineering*: John Wiley & Sons, 2013.

[21] S. S. Zhang, "A review on electrolyte additives for lithium-ion batteries," *Journal of Power Sources,* vol. 162, pp. 1379-1394, 2006.

[22] N. Williard, W. He, C. Hendricks, and M. Pecht, "Lessons learned from the 787 Dreamliner issue on lithium-ion battery reliability," *Energies,* vol. 6, pp. 4682-4695, 2013.

[23] S. J. An, J. Li, C. Daniel, D. Mohanty, S. Nagpure, and D. L. Wood, "The state of understanding of the lithium-ion-battery graphite solid electrolyte interphase (SEI) and its relationship to formation cycling," *Carbon*, vol. 105, pp. 52-76, 2016.

[24] J. B. Goodenough and K.-S. Park, "The Li-ion rechargeable battery: a perspective," *Journal of the American Chemical Society,* vol. 135, pp. 1167-1176, 2013.

[25] A. Patil, V. Patil, D. W. Shin, J.-W. Choi, D.-S. Paik, and S.-J. Yoon, "Issue and challenges facing rechargeable thin film lithium batteries," *Materials Research Bulletin,* vol. 43, pp. 1913-1942, 2008.

[26] R. Yazami, "Surface chemistry and lithium storage capability of the graphite–lithium electrode," *Electrochimica Acta,* vol. 45, pp. 87-97, 1999.

[27] R. Yazami and Y. F. Reynier, "Mechanism of self-discharge in graphite–lithium anode," *Electrochimica Acta,* vol. 47, pp. 1217-1223, 2002.

[28] M. Nie, D. Chalasani, D. P. Abraham, Y. Chen, A. Bose, and B. L. Lucht, "Lithium ion battery graphite solid electrolyte interphase revealed by microscopy and spectroscopy," *The Journal of Physical Chemistry C,* vol. 117, pp. 1257-1267, 2013.

[29] J. Vetter, P. Novák, M. Wagner, C. Veit, K.-C. Möller, J. Besenhard, *et al.*, "Ageing mechanisms in lithium-ion batteries," *Journal of Power Sources,* vol. 147, pp. 269-281, 2005.

[30] K. G. Gallagher, S. E. Trask, C. Bauer, T. Woehrle, S. F. Lux, M. Tschech, *et al.*, "Optimizing areal capacities through understanding the limitations of lithium-ion electrodes," *Journal of The Electrochemical Society,* vol. 163, pp. A138-A149, 2016.

[31] C.-S. Kim, K. M. Jeong, K. Kim, and C.-W. Yi, "Effects of capacity ratios between anode and cathode on electrochemical properties for lithium polymer batteries," *Electrochimica Acta,* vol. 155, pp. 431-436, 2015.

[32] J. Smekens, R. Gopalakrishnan, N. V. d. Steen, N. Omar, O. Hegazy, A. Hubin, *et al.*, "Influence of Electrode Density on the Performance of Li-Ion Batteries: Experimental and Simulation Results," *Energies,* vol. 9, p. 104, 2016.

[33] P.-L. Taberna, S. Mitra, P. Poizot, P. Simon, and J.-M. Tarascon, "High rate capabilities Fe3O4-based Cu nano-architectured electrodes for lithium-ion battery applications," *Nature Materials,* vol. 5, pp. 567-573, 2006.

[34] J. B. Goodenough and Y. Kim, "Challenges for rechargeable Li batteries†," *Chemistry of Materials,* vol. 22, pp. 587-603, 2009.

[35] Z. Li, J. Huang, B. Y. Liaw, V. Metzler, and J. Zhang, "A review of lithium deposition in lithium-ion and lithium metal secondary batteries," *Journal of Power Sources,* vol. 254, pp. 168-182, 2014.

[36] C. T. Love, O. A. Baturina, and K. E. Swider-Lyons, "Observation of lithium dendrites at ambient temperature and below," *ECS Electrochemistry Letters,* vol. 4, pp. A24-A27, 2015.

[37] K. J. Harry, K. Higa, V. Srinivasan, and N. P. Balsara, "Influence of Electrolyte Modulus on the Local Current Density at a Dendrite Tip on a Lithium Metal Electrode," *Journal of the Electrochemical Society,* vol. 163, pp. A2216-A2224, 2016.

[38] M. F. Hasan, C. F. Chen, C. E. Shaffer, and P. P. Mukherjee, "Analysis of the Implications of Rapid Charging on Lithium-Ion Battery Performance," *Journal of the Electrochemical Society,* vol. 162, pp. A1382-A1395, 2015.

[39] K. Nishikawa, Y. Fukunaka, T. Sakka, Y. H. Ogata, and J. R. Selman, "Measurement of concentration profile during charging of Li battery anode materials in LiClO4-PC electrolyte," *Electrochimica Acta,* vol. 53, pp. 218-223, Nov 20 2007.

[40] C. Brissot, M. Rosso, J.-N. Chazalviel, P. Baudry, and S. Lascaud, "In situ study of dendritic growth inlithium/PEO-salt/lithium cells," *Electrochimica Acta,* vol. 43, pp. 1569-1574, 1998.

[41] F. Orsini, A. Du Pasquier, B. Beaudouin, J. Tarascon, M. Trentin, N. Langenhuizen, *et al.*, "In situ SEM study of the interfaces in plastic lithium cells," *Journal of Power Sources,* vol. 81, pp. 918-921, 1999.

[42] M. Dollé, L. Sannier, B. Beaudoin, M. Trentin, and J.-M. Tarascon, "Live scanning electron microscope observations of dendritic growth in lithium/polymer cells," *Electrochemical and Solid-State Letters,* vol. 5, pp. A286-A289, 2002.

[43] O. Crowther and A. C. West, "Effect of electrolyte composition on lithium dendrite growth," *Journal of the Electrochemical Society,* vol. 155, pp. A806-A811, 2008.

[44] J. Barton and J. M. Bockris, "The electrolytic growth of dendrites from ionic solutions," in *Proceedings of the Royal Society of London A: Mathematical, Physical and Engineering Sciences,* 1962, pp. 485-505.

[45] R. Mogi, M. Inaba, S.-K. Jeong, Y. Iriyama, T. Abe, and Z. Ogumi, "Effects of some organic additives on lithium deposition in propylene carbonate," *Journal of The Electrochemical Society,* vol. 149, pp. A1578-A1583, 2002.

[46] R. McMillan, H. Slegr, Z. Shu, and W. Wang, "Fluoroethylene carbonate electrolyte and its use in lithium ion batteries with graphite anodes," *Journal of Power Sources,* vol. 81, pp. 20-26, 1999.

[47] G. Park, N. Gunawardhana, H. Nakamura, Y.-S. Lee, and M. Yoshio, "The study of electrochemical properties and lithium deposition of graphite at low temperature," *Journal of Power Sources,* vol. 199, pp. 293-299, 2012.

[48] G. Park, N. Gunawardhana, H. Nakamura, Y. Lee, and M. Yoshio, "Suppression of Li deposition on surface of graphite using carbon coating by thermal vapor deposition process," *Journal of Power Sources,* vol. 196, pp. 9820-9824, 2011.

[49] M. Yoshio, H. Wang, K. Fukuda, Y. Hara, and Y. Adachi, "Effect of Carbon Coating on Electrochemical Performance of Treated Natural Graphite as Lithium-Ion Battery Anode Material," *Journal of The Electrochemical Society,* vol. 147, pp. 1245-1250, 2000.

[50] K. J. Harry, D. T. Hallinan, D. Y. Parkinson, A. A. MacDowell, and N. P. Balsara, "Detection of subsurface structures underneath dendrites formed on cycled lithium metal electrodes," *Nature Materials,* vol. 13, pp. 69-73, 2014.

[51] J. Diggle, A. Despic, and J. M. Bockris, "The mechanism of the dendritic electrocrystallization of zinc," *Journal of The Electrochemical Society,* vol. 116, pp. 1503-1514, 1969.

[52] C. Monroe and J. Newman, "Dendrite growth in lithium/polymer systems a propagation model for liquid electrolytes under galvanostatic conditions," *Journal of The Electrochemical Society,* vol. 150, pp. A1377-A1384, 2003.

[53] R. Akolkar, "Mathematical model of the dendritic growth during lithium electrodeposition," *Journal of Power Sources,* vol. 232, pp. 23-28, 2013.

[54] P. J. Roache, *Verification and validation in computational science and engineering*: Hermosa, 1998.

[55] F. Jay and J. Goetz, "IEEE Standard Dictionary of Electrical and Electronics Terms, ; The Institute of Electrical and Electronics Engineers," *Inc.: New York,* 1984.

[56] D. Tremblay, S. Etienne, and D. Pelletier, "Code verification and the method of manufactured solutions for fluid-structure interaction problems," in *36th AIAA fluid dynamics conference*, 2006, pp. 882-892.

[57] U. B. Mehta, "Guide to credible computational fluid dynamics simulations," in *1995 26 th AIAA Fluid Dynamics Conference*, 1995.

[58] P. Roache, P. Knupp, S. Steinberg, and R. Blaine, "Experience with benchmark test cases for groundwater flow," in *1990 Spring Meeting of the Fluids Engineering Division, Toronto, Ont, Can, 06/04-07/90*, 1990, pp. 49-56.

[59] S. G. Stewart and J. Newman, "The use of UV/vis absorption to measure diffusion coefficients in LiPF6 electrolytic solutions," *Journal of the Electrochemical Society,* vol. 155, pp. F13-F16, 2008.

[60] J. Newman and K. E. Thomas-Alyea, *Electrochemical systems*: John Wiley & Sons, 2012.

[61] L. O. Valøen and J. N. Reimers, "Transport properties of LiPF6-based Li-ion battery electrolytes," *Journal of The Electrochemical Society,* vol. 152, pp. A882-A891, 2005.

[62] M. Ota, S. Izuo, K. Nishikawa, Y. Fukunaka, E. Kusaka, R. Ishii*, et al.*, "Measurement of concentration boundary layer thickness development during lithium electrodeposition onto a lithium metal cathode in propylene carbonate," *Journal of Electroanalytical Chemistry,* vol. 559, pp. 175-183, 2003.

[63] J. Crank, *The mathematics of diffusion*: Oxford university press, 1979.

[64] J. Crank and P. Nicolson, "A practical method for numerical evaluation of solutions of partial differential equations of the heat-conduction type," in *Mathematical Proceedings of the Cambridge Philosophical Society*, 1947, pp. 50-67.

[65] J. Philip, "Numerical solution of equations of the diffusion type with diffusivity concentration-dependent," *Transactions of the Faraday Society,* vol. 51, pp. 885-892, 1955.

[66] D. W. Jonathan E. Guyer, James A. Warren, "FiPy Manual Release 3.0," N. I. o. S. a. Technology, Ed., ed, 2012.

[67] P. J. Roache, *Fundamentals of Verification and Validation*: hermosa publ., 2009.

[68] P. K. Kambiz Salari, "Code Verification by the Method of Manufactured Solutions," Sandia National Laboratories, Albuquerque, NM2000.

[69] J. Dahn, A. Sleigh, H. Shi, J. Reimers, Q. Zhong, and B. Way, "Dependence of the electrochemical intercalation of lithium in carbons on the crystal structure of the carbon," *Electrochimica Acta,* vol. 38, pp. 1179-1191, 1993.

[70] S. Flandrois and B. Simon, "Carbon materials for lithium-ion rechargeable batteries," *Carbon,* vol. 37, pp. 165-180, 1999.

[71] Y. Masaki, J. B. Ralph, and K. Akiya, "Lithium-Ion Batteries, Science and Technologies," ed: Springer, New York, 2009.

[72] J. H. Ying Yan, Xinghong Zhang, Yumin Zhang, Jigang Zhou, David Muir, Ronny Sutarto, Zhihua Zhang, Shengwei Liu, Bo Song, "Facile synthesis of few-layer-thick carbon nitride nanosheets by liquid ammonia-assisted lithiation method and their photocatalytic redox properties," *Royal Society of Chemistry,* vol. 4, pp. 32690-32697, 2014.

[73] H. Shi, J. Barker, M. Saidi, and R. Koksbang, "Structure and lithium intercalation properties of synthetic and natural graphite," *Journal of the Electrochemical Society*, vol. 143, pp. 3466-3472, 1996.

[74] P. Lian, X. Zhu, S. Liang, Z. Li, W. Yang, and H. Wang, "Large reversible capacity of high quality graphene sheets as an anode material for lithium-ion batteries," *Electrochimica Acta,* vol. 55, pp. 3909-3914, 2010.

[75] M. Corporation. (2016, April 7, 2016). *Li-Ion Battery Anode -Copper Foil Single Side Coated by CMS Graphite (241 mm L x 200mm W x0.1mm Thickness)*. Available: http://www.mtixtl.com/Li%C2%ADIonBatteryAnode%C2%ADCopperfoilsinglesidecoatedbyCMSGraphite241mm%C2%AD1.aspx

[76] C. Uhlmann, J. Illig, M. Ender, R. Schuster, and E. Ivers-Tiffée, "In situ detection of lithium metal plating on graphite in experimental cells," *Journal of Power Sources,* vol. 279, pp. 428-438, 2015.

[77] C. Weng, J. Sun, and H. Peng, "An open-circuit-voltage model of lithium-ion batteries for effective incremental capacity analysis," in *ASME 2013 Dynamic Systems and Control Conference*, 2013, pp. V001T05A002-V001T05A002.

[78] D. Aurbach, I. Weissman, H. Yamin, and E. Elster, "The correlation between charge/discharge rates and morphology, surface chemistry, and performance of Li electrodes and the connection to cycle life of practical batteries," *Journal of the Electrochemical Society,* vol. 145, pp. 1421-1426, May 1998.

[79] M. Dolle, L. Sannier, B. Beaudoin, M. Trentin, and J. M. Tarascon, "Live scanning electron microscope observations of dendritic growth in lithium/polymer cells," *Electrochemical and Solid State Letters,* vol. 5, pp. A286-A289, Dec 2002.

[80] H. Ghassemi, M. Au, N. Chen, P. A. Heiden, and R. S. Yassar, "Real-time observation of lithium fibers growth inside a nanoscale lithium-ion battery," *Applied Physics Letters,* vol. 99, Sep 19 2011.

[81] X. H. Liu, L. Zhong, L. Q. Zhang, A. Kushima, S. X. Mao, J. Li*, et al.*, "Lithium fiber growth on the anode in a nanowire lithium ion battery during charging," *Applied Physics Letters*, vol. 98, May 2 2011.

[82] D. Aurbach, M. Daroux, G. Mcdougall, and E. B. Yeager, "Spectroscopic Studies of Lithium in an Ultrahigh-Vacuum System," *Journal of Electroanalytical Chemistry,* vol. 358, pp. 63-76, Nov 1 1993.

[83] H. Ota, Y. Sakata, X. M. Wang, J. Sasahara, and E. Yasukawa, "Characterization of lithium electrode in lithium imides/ethylene carbonate and cyclic ether electrolytes - II. Surface chemistry," *Journal of the Electrochemical Society,* vol. 151, pp. A437-A446, Mar 2004.

[84] D. Aurbach, A. Zaban, Y. Ein-Eli, I. Weissman, O. Chusid, B. Markovsky*, et al.,* "Recent studies on the correlation between surface chemistry, morphology, three-dimensional structures and performance of Li and Li-C intercalation anodes in several important electrolyte systems," *Journal of Power Sources*, vol. 68, pp. 91-98, Sep 1997.

[85] P. C. Howlett, D. R. MacFarlane, and A. F. Hollenkamp, "A sealed optical cell for the study of lithium-electrode electrolyte interfaces," *Journal of Power Sources,* vol. 114, pp. 277-284, Mar 12 2003.

[86] K. Nishikawa, T. Mori, T. Nishida, Y. Fukunaka, M. Rosso, and T. Homma, "In Situ Observation of Dendrite Growth of Electrodeposited Li Metal," *Journal of the Electrochemical Society,* vol. 157, pp. A1212-A1217, 2010.

[87] G. Instruments. (January 11). *Basics of Electrochemical Impedance Spectroscopy*. Available: https://www.gamry.com/application-notes/EIS/basics-of-electrochemical-impedance-spectroscopy/

[88] S. Rodrigues, N. Munichandraiah, and A. Shukla, "AC impedance and state-of-charge analysis of a sealed lithium-ion rechargeable battery," *Journal of Solid State Electrochemistry,* vol. 3, pp. 397-405, 1999.

[89] J. Li, E. Murphy, J. Winnick, and P. Kohl, "Studies on the cycle life of commercial lithium ion batteries during rapid charge–discharge cycling," *Journal of Power Sources,* vol. 102, pp. 294-301, 2001.

[90] S. S. Zhang, K. Xu, and T. R. Jow, "Understanding formation of solid electrolyte interface film on LiMn2O4 electrode," *Journal of the Electrochemical Society,* vol. 149, pp. A1521-A1526, Dec 2002.

[91] C. Wang, A. J. Appleby, and F. E. Little, "Electrochemical impedance study of initial lithium ion intercalation into graphite powders," *Electrochimica Acta,* vol. 46, pp. 1793-1813, 2001.

[92] N. Takami, A. Satoh, M. Hara, and I. Ohsaki, "Structural and Kinetic Characterization of Lithium Intercalation into Carbon Anodes for Secondary Lithium Batteries," *Journal of the Electrochemical Society,* vol. 142, pp. 371-379, Feb 1995.

[93] J. Song, H. Lee, Y. Wang, and C. Wan, "Two-and three-electrode impedance spectroscopy of lithium-ion batteries," *Journal of Power Sources,* vol. 111, pp. 255-267, 2002.

[94] F. Huet, "A review of impedance measurements for determination of the state-of-charge or state-of-health of secondary batteries," *Journal of Power Sources,* vol. 70, pp. 59-69, Jan 30 1998.

[95] M. G. S. R. Thomas, P. G. Bruce, and J. B. Goodenough, "Ac Impedance Analysis of Polycrystalline Insertion Electrodes - Application to Li1-Xcoo2," *Journal of the Electrochemical Society,* vol. 132, pp. 1521-1528, 1985.

[96] D. Andre, M. Meiler, K. Steiner, C. Wimmer, T. Soczka-Guth, and D. Sauer, "Characterization of high-power lithium-ion batteries by electrochemical impedance spectroscopy. I. Experimental investigation," *Journal of Power Sources,* vol. 196, pp. 5334-5341, 2011.

[97] M. Itagaki, N. Kobari, S. Yotsuda, K. Watanabe, S. Kinoshita, and M. Ue, "In situ electrochemical impedance spectroscopy to investigate negative electrode of lithium-ion rechargeable batteries," *Journal of Power Sources,* vol. 135, pp. 255-261, Sep 3 2004.

[98] C. H. Chen, J. Liu, and K. Amine, "Symmetric cell approach and impedance spectroscopy of high power lithium-ion batteries," *Journal of Power Sources,* vol. 96, pp. 321-328, Jun 15 2001.

[99] T. Waldmann, B.-I. Hogg, M. Kasper, S. Grolleau, C. G. Couceiro, K. Trad*, et al.*, "Interplay of Operational Parameters on Lithium Deposition in Lithium-Ion Cells: Systematic Measurements with Reconstructed 3-Electrode Pouch Full Cells," *Journal of The Electrochemical Society,* vol. 163, pp. A1232-A1238, 2016.

[100] B. S. Instruments, *EC-Lab Express Software User's Manual Version 5.5x*, 2011.

[101] U. Troltzsch, O. Kanoun, and H. R. Trankler, "Characterizing aging effects of lithium ion batteries by impedance spectroscopy," *Electrochimica Acta,* vol. 51, pp. 1664-1672, Jan 20 2006.

[102] Y. Krämer, C. Birkenmaier, J. Feinauer, A. Hintennach, C. L. Bender, M. Meiler*, et al.*, "A New Method for Quantitative Marking of Deposited Lithium by Chemical Treatment on Graphite Anodes in Lithium-Ion Cells," *Chemistry–A European Journal,* vol. 21, pp. 6062-6065, 2015.

[103] X. L. Wang, K. An, L. Cai, Z. L. Feng, S. E. Nagler, C. Daniel*, et al.*, "Visualizing the chemistry and structure dynamics in lithium-ion batteries by in-situ neutron diffraction," *Scientific Reports,* vol. 2, Oct 19 2012.